

Direct Numerical Simulation of Turbulent
Flow and Heat Transfer in a Channel with
Surface Roughness

Takahiro Miura

Doctoral Program in Advanced Materials Science
and Technology

Graduate School of Science and Technology

Niigata University

Contents

Nomenclature	1
Chapter 1 Introduction	3
1.1. Background.....	3
1.2. Rough Surface Flow	5
1.3. Dissimilarity between Momentum and Heat Transfer	5
1.4. Direct Numerical Simulation.....	6
1.5. Contents of the Thesis	7
1.6. References	7
Chapter 2 Channel Flow with a Single Rib	10
2.1. Introduction	10
2.2. Numerical Methods	10
2.3. Hydraulic Loss and Heat Transfer.....	16
2.4. Turbulence Statistics of Flow	19
2.5. Turbulence Statistics of Temperature.....	21
2.6. Budgets of Reynolds Stress	22
2.7. Structures of Instantaneous Field	27
2.8. Conclusions	28
2.9. References	29
Chapter 3 Transport Dissimilarity	31
3.1. Introduction	31
3.2. Numerical Methods	32
3.3. Hydrodynamic Loss and Heat Transfer.....	35
3.4. Structure of Flow and Thermal Fields.....	38
3.5. Statistical Analysis	44
3.6. Octant Analysis	48
3.7. Conclusions	53
3.8. References	55
Chapter 4 Channel Flow with Ribs.....	57
4.1. Introduction	57

4.2. Numerical Methods for Developing Region	57
4.3. Numerical Methods for Fully Developed Region	58
4.4. Comparison with Experimental Data	59
4.5. Hydraulic Loss and Heat Transfer.....	61
4.6. Turbulence Statistics of Flow	63
4.7. Vortex Structures.....	65
4.8. Turbulence Statistics of Temperature.....	69
4.9. Conclusions	70
4.10. References.....	71
Chapter 5 Curved Channel Flow with a Single Rib	72
5.1. Introduction	72
5.2. Numerical Methods	72
5.3. Heat Transfer Coefficient.....	76
5.4. Mean Velocity Vectors.....	78
5.5. Power Spectral Density	78
5.6. Thermo-Hydraulic Performance.....	78
5.7. Conclusions	85
5.8. References	86
Chapter 6 Conclusions	87
Appendix: Parallel Computation.....	88
Acknowledgements	89

Nomenclature

C_f	:	skin friction coefficient, $2\bar{\tau}_w/(\rho U_m^2)$
C_p	:	specific heat at constant pressure
d_h	:	hydraulic diameter
E	:	spectral density
f	:	friction factor
H	:	height of rib
h	:	heat transfer coefficient
k	:	turbulent kinetic energy, $\overline{u_i' u_i'}/2$
k_z	:	spanwise wave number
L_u	:	length from inlet to rib
L_{st}	:	length from inlet to curve
L_x, L_z	:	computational domain sizes in x and z directions
N_{rib}	:	number of ribs
Nu	:	Nusselt number
N_x, N_y, N_z	:	grid numbers in x, y and z directions
Pi	:	rib pitch
Pr	:	Prandtl number
p	:	pressure
Q	:	second invariant of velocity-gradient tensor, $-(\partial u_i/\partial x_j)(\partial u_j/\partial x_i)/2$
q_w	:	wall heat flux
Re	:	Reynolds number, $U_{max}\delta/\nu$
Re_{dh}	:	Reynolds number, $U_m d_h/\nu$
Re_m	:	Reynolds number, $2U_m\delta/\nu$
Re_τ	:	Reynolds number, $U_\tau\delta/\nu$
r	:	radial coordinate
St	:	Stanton number, $Nu/PrRe_m$
T	:	temperature
t	:	time
U_m	:	bulk mean velocity
U_{max}	:	maximum mean velocity
U_τ	:	friction velocity, $(\tau_w/\rho)^{1/2}$
u, v, w	:	velocity in x, y and z directions
W	:	width of rib
x, y, z	:	streamwise, wall-normal and spanwise coordinates

α	:	radius ratio of curved channel, r_i/r_o
ΔT_w	:	temperature difference between walls
Δt	:	time increment
$\Delta x, \Delta y, \Delta z$:	grid spacings in x, y and z directions
δ	:	channel half width
ε	:	efficiency parameter
θ	:	temperature difference, $T-T_r$
λ	:	thermal conductivity
λ_z	:	wave length in z direction
ν	:	kinematic viscosity
ρ	:	density
τ_w	:	wall shear stress
φ	:	azimuthal coordinate

Subscripts and Superscripts

$()_0$:	value in driver part or on inlet
$()_1$:	streamwise direction
$()_2$:	wall-normal direction
$()_3$:	spanwise direction
$()_i$:	value on inner-wall side
$()_o$:	value on outer-wall side
$()_r$:	value on rough-wall side
$()_s$:	value on smooth-wall side
$()_{SM}$:	value in smooth channel for same Reynolds number
$()_w$:	wall
$()_{xm}$:	averaged value in x
$()'$:	fluctuating component
$()^*$:	normalized by $\delta, U_{\tau 0}$, and ΔT_w
$()^+$:	normalized by U_τ and ν
$()^{(+)}$:	normalized by $U_{\tau 0}$ and ν
$\overline{()}$:	ensemble averaged value
$\langle () \rangle$:	averaged value in x or in z

Chapter 1 Introduction

1.1. Background

At the present time, environmental problems are serious. Especially increase of greenhouse gases and the crisis of global warming are recognized widely. Kyoto Protocol was initially adopted in 1997. The target of the protocol is to reduce the overall emissions of six greenhouse gases from industrialized countries by at least five percent below the 1990 levels in the commitment period 2008 to 2012. However, the total primary energy consumption in the world is increasing (Fig. 1.1). The consumption of Organization for Economic Cooperation and Development (OECD) member nations (industrialized countries) in recent years has nearly plateaued, but it still increases about 20 percent from 1990 level. Total carbon dioxide (typical greenhouse gas) emissions from the consumption of energy in the world are also increasing (Fig. 1.2). The emissions from OECD have been decreasing recently, but the emissions in 2009 increased approximately nine percent from those in 1990. Hence, the achievement of the Kyoto Protocol's object is hopeless. It is important to improve the efficiency of energy conversion systems.

Heat transfer technology is essential improving to the energy efficiency. Heat engines need cooling when it is operated. Heat transfer of the cooling is enhanced by the air or water flow as we can experience by a fan. In order to enhance the convection heat transfer, energy which drives fluid generally needs to increase. Hence, invention of a method for improving heat transfer with the lowest hydraulic loss is desired.

All fluid flow is normally classified into the laminar flow or the turbulent flow. Optimizing the thermo-hydrodynamic performance in laminar flows is comparatively easy because its analysis and simulation are simple. On the other hand, turbulent flows are complex and its analysis is still challenging. Actual products with a turbulent flow are designed by trial and errors and/or calculation using turbulent models. Turbulence is one of the great unsolved problems in physics. This thesis deals with turbulent flow.

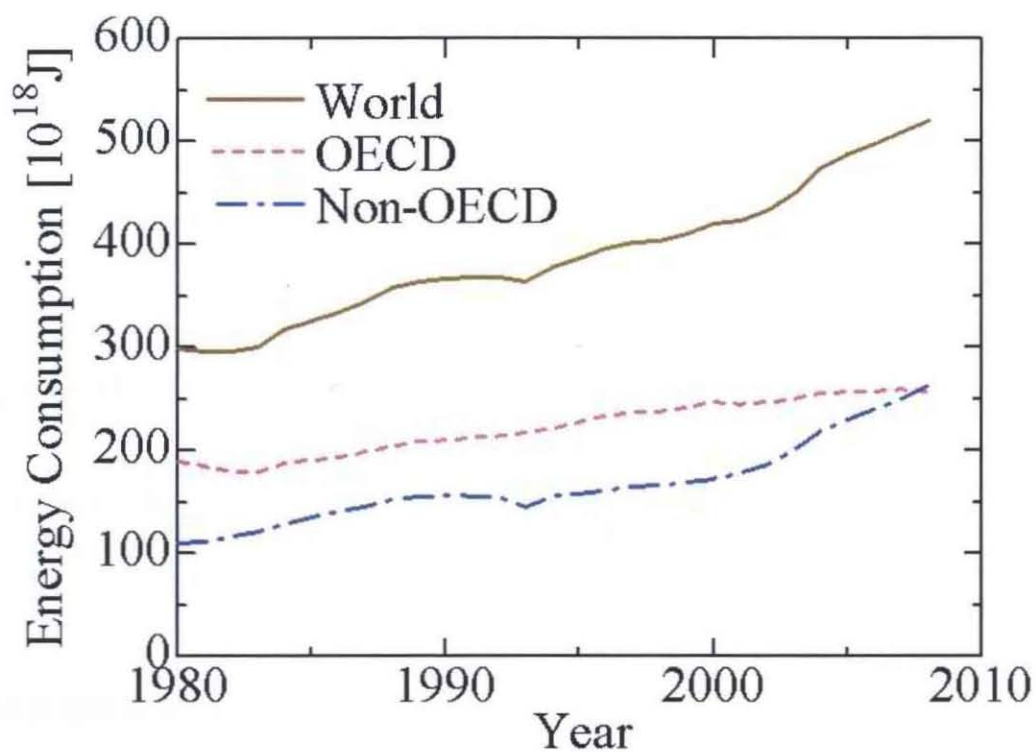


Fig. 1.1 Total primary energy consumption⁽¹⁾.

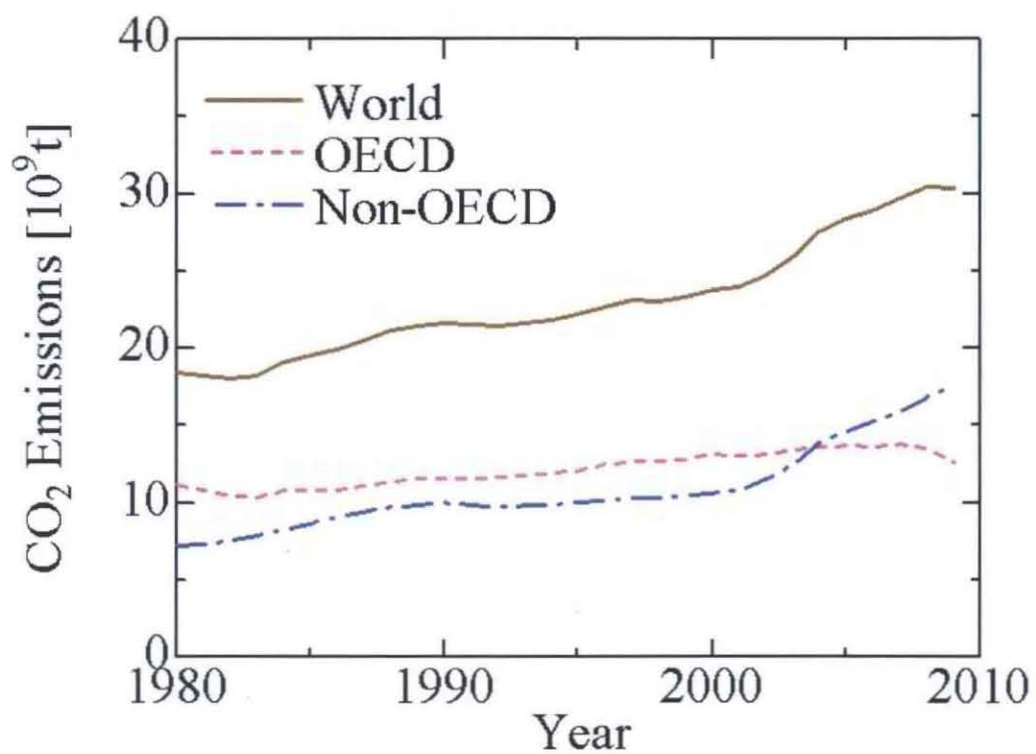


Fig. 1.2 Total carbon dioxide emissions from the consumption of energy⁽¹⁾.

1.2. Rough Surface Flow

The use of surface roughness is one of the earliest but effective techniques in turbulent flows⁽²⁾⁻⁽⁶⁾. Thanks to the activated heat transport by turbulent vortices, heat transfer of turbulent flow is higher than that of laminar flow. However, the viscous sublayer near a wall has weak turbulence and high heat resistance. The rough surface disturbs the sublayer to promote momentum and heat transfer.

Most of early research focused on natural roughness of commercial tubes. However, because such natural roughness is not well defined, artificial or structured roughness is now usually applied^{(5), (6)}. One of the structured roughnesses is the transverse ribs shown in Fig. 1.3.

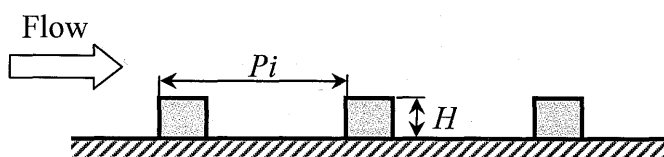


Fig. 1.3 Transverse ribs.

Many experimental studies reported on friction factors and heat transfer coefficients in rough tubes. Using these data and turbulence theory, several predictive equations for the friction factors and heat transfer coefficients have been proposed^{(3), (5)-(8)}. Norris⁽⁸⁾ suggested an empirical correlation:

$$\frac{Nu}{Nu_{SM}} = \left(\frac{f}{f_{SM}} \right)^n \quad \text{for } f / f_{SM} < 4, \quad (1.1)$$

where

$$n = 0.68 Pr^{0.215} \quad \text{for } 1 \leq Pr \leq 6. \quad (1.2)$$

Lewis⁽⁹⁾ used such equations to investigate the performance of a wide range of rough surfaces in channel flows. He used St^3/f as a parameter for thermo-hydraulic performance. Lewis concluded that the heat transfer enhancement occurred most efficiently when the roughness Reynolds number, $U_\tau H/\nu$, was 20 and the space between ribs corresponds to the total length of separation bubbles between ribs, i.e. $Pi/H \approx 9$. Details of techniques to enhance heat transfer are found in the handbooks by Bergles⁽⁵⁾ and Manglik⁽⁶⁾.

1.3. Dissimilarity between Momentum and Heat Transfer

Rough surfaces can improve heat transfer keeping low skin friction. It is likely that this dissimilarity is important for improving the thermo-hydraulic performance.

Several investigations⁽¹⁰⁾⁻⁽¹³⁾ on the dissimilarity between momentum transfer and

heat transfer have been carried out. These treated not surface roughness but a smooth wall with an inserted obstacle. Suzuki et al.⁽¹⁰⁾ found that heat transfer enhancement and wall friction reduction simultaneously occurred in the turbulent boundary layer disturbed by a cylinder. Yao et al.^{(11),(12)} visualized the channel turbulent flow inserted by a square rod, and clarified that the Karman vortex street correlated well with the heat transfer enhancement. Inaoka et al.⁽¹³⁾ applied the Reynolds averaged Navier-Stokes (RANS) model to simulate the turbulent boundary layer disturbed by a square rod. Their efforts envisioned roles of the Karman vortices which suppressed the wall friction and enhanced heat transfer simultaneously to result in the transport dissimilarity between momentum and heat.

1.4. Direct Numerical Simulation

The advent of a direct numerical simulation (DNS in short) was a major turning point for turbulence research. DNS is one of the turbulent flow simulations, which solves the Navier-Stokes equations without any turbulence model. DNS provides more detailed data than an experiment. DNS and experiments complement each other: DNS is validated by experimental data, and an experimenter checks the accuracy of the measurements using DNS data.

The disadvantage of DNS is its enormous computational costs. DNS requires accurately reproduce turbulence evolution over a wide range of length and time scales. A sufficient capacity to include the largest length scale is required for the computational domain, and the resolution which can resolve smaller vortices is required. Small time steps and long computation times are also demanded.

The significant improvement of computer hardware overcame the great costs of DNS. In 1972, Orszag and Patterson⁽¹⁴⁾ directly simulated isotropic turbulence at a Reynolds number (based on Taylor microscale) of 35. In 1987, Kim et al.⁽¹⁵⁾ performed DNS of fully developed plane channel flow at $Re_\tau = 180$. Kim and Moin⁽¹⁶⁾ added a thermal field to this DNS. Moser and Moin⁽¹⁷⁾ performed DNS of a curved channel flow. Details of DNS until 1998 were reviewed by Moin and Mahesh⁽¹⁸⁾.

The early attempts for DNS were made for simple flows at low Reynolds number due to the restriction of computer resources. Note that the smallest length scale of turbulent flows decreases as the Reynolds number is increased. In DNS, the treated flow fields are simplified from engineering problems. However, knowledge acquired through the fundamental flows can contribute to insight into the structures of real situations.

As computer resources improved, complex flows can be computed. Turbulent flow over a wall-bounded obstacle is a complex flow. In 1993, Yang and Ferziger⁽¹⁹⁾ carried out DNS of turbulent channel flow with a transverse rib mounted on one wall. They assumed periodic boundary conditions in the streamwise direction. Therefore, they actually simulated a periodic array of obstacles. Yakhot et al.⁽²⁰⁾ performed DNS of flow around a wall-mounted cube. They employed a fully developed turbulent channel flow additionally simulated as the inflow condition. Makino et al.⁽²¹⁾⁻⁽²³⁾ directly solved turbulent heat transfer over two-dimensional fences by the streamwise periodicity condition. Yakhot et al. and Makino et al. used an immersed-boundary

method to treat the obstacles. However, validity of wall variables by the immersed-boundary method was left ambiguous.

Several DNS⁽²⁴⁾⁻⁽³⁰⁾ of turbulent channel flow with repeated-rib roughness were also performed. Miyake et al.⁽²⁹⁾ and Nagano et al.⁽³⁰⁾ considered the heat transfer of such a flow. Nagano et al. simulated several roughnesses by varying rib height and pitch. They concluded that the smooth wall was more efficient than the rough wall because $(Nu/Nu_{SM})/(ff_{SM})$ was used for the evaluation. Equation (1.1) indicates $(Nu/Nu_{SM})/(ff_{SM}) \leq 1$.

1.5. Contents of the Thesis

In spite of investigations previously described, turbulent flows over surface roughness still have unsolved problems. Since most of existing studies have been made for the fully developed flow, the spatially developing region especially has many questions. The present investigations used DNS to clarify these problems.

This thesis is organized as follows.

Chapter 1 introduces the background and the related literatures. This chapter mentions the contents of the present thesis.

In Chapter 2, DNS of turbulent flow and heat transfer in a channel with a single transverse rib is performed. Additional simulations are run for the inflow condition as Yakhot et al.⁽²⁰⁾ did. The immersed-boundary method is not used, and the rib surface is accurately treated by the no-slip condition. As to the temperature field, the solid walls with the rib are isothermal, and the top and bottom walls have a temperature difference. Description is made for the rib height effects to heat transfer. The turbulence statistics of flow and temperature and the Reynolds stress budgets are investigated.

Chapter 3 discusses the channel with the single rib about its dissimilarity between momentum and heat transfer. Momentum and heat transport are similar in a smooth channel. However, the dissimilarity is generated behind the rib. The mechanisms are investigated through instantaneous fields, spectrum analysis and octant analysis.

Chapter 4 describes the spatially advancing rough-wall channel flow of its transition from the smooth wall to the rough wall. Fully advanced ribbed channel flow is also simulated to compare with the advancing case. Differences between the cases are investigated through turbulence statistics and instantaneous fields.

In Chapter 5, the curved channel with a single rib is treated. The rib is placed on either the inner- or outer-wall in front of the curved channel inlet. Flow and heat transfer characteristics are discussed to reveal effects of the rib on the curved channel flow.

The thesis summarizes the conclusions in Chapter 6.

1.6. References

- (1) U.S. Energy Information Administration, <http://www.eia.gov/>
- (2) Nikuradse, J. Laws of flow in rough pipes, VDI-Forschungsheft 361(1933); English translation as NACA-TM-1292 (1950).

- (3) Dipprey, D. F. and Sabersky, R. H., Heat and momentum transfer in smooth and rough tubes at various Prandtl numbers, *International Journal of Heat and Mass Transfer*, Vol. 6 (1963), pp.329-353.
- (4) Webb, R. L., Eckert, E. R. G., and Goldstein R. J., Heat transfer and friction in tubes with repeated-rib roughness, *International Journal of Heat and Mass Transfer*, Vol. 14 (1971), pp.601-617.
- (5) Bergles, A. E., Techniques to enhance heat transfer, *Handbook of Heat Transfer* third ed. (1998), McGraw-Hill, New York, Chapter 11.
- (6) Manglik, R. M., Heat transfer enhancement, *Heat Transfer Handbook*, Bejan, A. and Kraus, A. D. Editors (2003), John Wiley & Son, Chapter 14.
- (7) Kays, W. M., Crawford, M. E. and Weigand, B., *Convective Heat and Mass Transfer*, fourth ed. (2005), McGraw-Hill, New York.
- (8) Noris, R. H., Some simple approximate heat transfer correlations for turbulent flow in ducts with rough surfaces, *Augmentation of Convective Heat and Mass Transfer* (1970), American Society of Mechanical Engineers, New York, pp.16-26.
- (9) Lewis, M. J., Optimising the thermohydraulic performance of rough surfaces, *International Journal of Heat and Mass Transfer*, Vol. 18 (1975), pp.1243-1248.
- (10) Suzuki, H., Suzuki, K. and Sato, T., Dissimilarity between heat and momentum transfer in a turbulent boundary layer disturbed by a cylinder, *International Journal of Heat and Mass Transfer*, Vol. 31 (1988), pp.259-265.
- (11) Yao, M., Nakatani, M., Okuda, M. and Suzuki, K., Simultaneous measurements of flow and thermal fields in a turbulent channel flow with insertion of a square rod, *Transactions of the JSME Series B*, Vol. 60 (1994), pp.4192-4199.
- (12) Yao, M., Nakatani, M. and Suzuki, K., Flow visualization and heat transfer experiments in a turbulent channel flow obstructed with an inserted square rod, *International Journal of Heat and Fluid Flow*, Vol. 16 (1995), pp.389-397.
- (13) Inaoka, K., Yamamoto, J. and Suzuki, K., Dissimilarity between heat transfer and momentum transfer in a disturbed turbulent boundary layer with insertion of a rod - modeling and numerical simulation, *International Journal of Heat and Fluid Flow*, Vol. 20 (1999), pp.290-301.
- (14) Orszag, S. A. and Patterson, G. S., Numerical simulation of three-dimensional homogeneous isotropic turbulence, *Physical Review Letters*, Vol. 28 (1972), pp.76-79.
- (15) Kim, J., Moin, P. and Moser, R., Turbulence statistics in fully developed channel flow at low Reynolds number, *Journal of Fluid Mechanics*, Vol. 177 (1987), pp.133-166.
- (16) Kim, J. and Moin, P., Transport of passive scalars in a turbulent channel flow, *Turbulent shear flows 6*, Springer-Verlag, Berlin (1989), pp.85-96.
- (17) Moser, R. D. and Moin, P., The effects of curvature in wall-bounded turbulent flows, *Journal of Fluid Mechanics*, Vol. 175 (1987), pp.479-510.
- (18) Moin, P. and Mahesh, K., Direct numerical simulation: a tool in turbulence research, *Annual Review of Fluid Mechanics*, Vol. 30 (1998), pp.539-578.

- (19) Yang, K. and Ferziger, J. H., Large-eddy simulation of turbulent obstacle flow using a dynamic subgrid-scale model, *AIAA Journal*, Vol. 31 (1993), pp.1406-1413.
- (20) Yakhot, A., Liu, H. and Nikitin, N., Turbulent flow around a wall-mounted cube: A direct numerical simulation, *International Journal of Heat and Fluid Flow*, Vol. 27 (2006), pp.994-1009.
- (21) Makino, S., Iwamoto, K. and Kawamura, H., Direct numerical simulation of Turbulent heat transfer behind a rectangular orifice, *Thermal Science and Engineering*, Vol. 15, No. 4 (2007), pp.175-183.
- (22) Makino, S., Iwamoto, K. and Kawamura, H., Turbulent structures and statistics in turbulent channel flow with two-dimensional slits, *International Journal of Heat and Fluid Flow*, Vol. 29 (2008), pp.602-611.
- (23) Makino, S., Iwamoto, K. and Kawamura, H., DNS of turbulent heat transfer through two-dimensional slits, *Progress in Computational Fluid Dynamics*, Vol. 8, Nos. 7/8 (2008), pp.397-405.
- (24) Leonardi, S., Orlandi, P., Smalley, R. J., Djenidi, L. and Antonia, R. A., Direct numerical simulations of turbulent channel flow with transverse square bars on one wall, *Journal of Fluid Mechanics*, Vol. 491 (2003), pp.229-238.
- (25) Leonardi, S., Orlandi, P., Djenidi, L. and Antonia, R. A., Structure of turbulent channel flow with square bars on one wall, *International Journal of Heat and Fluid Flow*, Vol. 25 (2004), pp.384-392.
- (26) Ashrafian, A., Andersson, H. I. and Manhart, M., DNS of turbulent flow in a rod-roughened channel, *International Journal of Heat and Fluid Flow*, Vol. 25 (2004), pp.373-383.
- (27) Ashrafian, A. and Andersson, H. I., The structure of turbulence in a rod-roughened channel, *International Journal of Heat and Fluid Flow*, Vol. 27 (2006), pp.65-79.
- (28) Ikeda, T., and Durbin, P. A., Direct simulations of a rough-wall channel flow, *Journal of Fluid Mechanics*, Vol. 571 (2007), pp.235-263.
- (29) Miyake, Y., Tsujimoto, K. and Nakaji, M., Direct numerical simulation of rough-wall heat transfer in a turbulent channel flow, *International Journal of Heat and Fluid Flow*, Vol. 22 (2001), pp.237-244.
- (30) Nagano, Y., Hattori, H. and Houra, T., DNS of velocity and thermal fields in turbulent channel flow with transverse-rib roughness, *International Journal of Heat and Fluid Flow*, Vol. 25 (2004), pp.393-403.

Chapter 2 Channel Flow with a Single Rib

2.1. Introduction

Wall roughness or protrusions are convenient tools to destabilize wall-bounded flows. This type of device can be utilized for fluid control and augmentation of heat transfer in turbo-machinery, power generators, combustors and chemical reactors. Enhancement of inner-cooling in gas-turbine blades is one of applications. Optimization of the roughness or the turbulator is a key to achieve better performance in machinery of energy conversion and process engineering.

In addition to the practical importance of fully developed cases of periodic obstacles⁽¹⁾⁻⁽⁵⁾, the case of a single obstacle means a lot both scientifically and practically⁽⁶⁾⁻⁽¹⁰⁾. Suzuki et al.⁽⁶⁾ reported that the heat transfer increase and the friction decrease simultaneously occurred in a local spot of the turbulent boundary layer inserted by an cylinder. Yao et al.⁽⁷⁾ visualized flow fields in a similar situation, and they argued about roller structures behind the obstacle, which caused the local dissimilarity between the heat transfer and the friction on the wall.

In spite of these efforts, there is ambiguity in the heat transfer enhancement by a single obstacle. At the present time, it is not evident if the overall heat transfer in the case with an obstacle can actually exceed the flat-plate case. The recent DNSs (Direct Numerical Simulations) for non-periodic cases⁽⁸⁾⁻⁽¹⁰⁾ did not resolve this question since they targeted on basic fluid mechanics not paying special attention to the heat transfer enhancement.

In the present study, a spatially advancing type of DNS is performed for turbulent air flows in a channel with a single rib mounted on the wall. The frictional Reynolds number is kept at 150 at the channel inlet, and the ratio of the rib height to the channel half width is changed in 0.05, 0.1, 0.2 and 0.4. The mean Nusselt number is analyzed through comparison with the flat-plate case showing the same pumping loss in order to verify the total merit of the single-rib augmentation. Mechanisms of heat transfer enhancement are examined through discussion of turbulence statistics of flow and temperature and the Reynolds stress budgets. An instantaneous flow is argued to compile information on turbulence structures related to transport process.

2.2. Numerical Methods

Figure 2.1 shows the computational domain and the coordinate system. A fully developed turbulent flow with thermal variation is assumed to enter a straight channel obstructed by one rectangular rib protruded from the wall. The inlet values for the ribbed channel are generated by the driver part, where a constant pressure gradient drives the fluid flow. Periodic boundary condition is employed in streamwise and spanwise directions of the driver part, and in the spanwise direction of the main part. In both of the driver and main parts, no-slip condition is used on channel walls. Temperature of the lower walls and rib surfaces are kept at $(T-T_r)/\Delta T_w = 0$, and that of the upper walls are fixed at $(T-T_r)/\Delta T_w = 1$. At the exit of the main part, the convection

out-flow condition⁽¹¹⁾ is applied for flow and temperature fields.

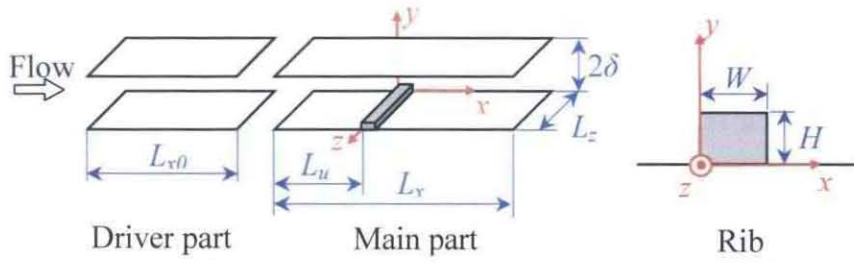


Fig. 2.1 Computational domain and coordinate system.

The continuity, Navier-Stokes and energy equations for the incompressible fluid;

$$\frac{\partial u_j}{\partial x_j} = 0, \quad (2.1)$$

$$\frac{\partial u_i}{\partial t} + u_j \frac{\partial u_i}{\partial x_j} = -\frac{1}{\rho} \frac{\partial p}{\partial x_i} + \nu \frac{\partial^2 u_i}{\partial x_j \partial x_j}, \quad (2.2)$$

$$\frac{\partial T}{\partial t} + u_j \frac{\partial T}{\partial x_j} = \frac{\lambda}{\rho C_p} \frac{\partial^2 T}{\partial x_j \partial x_j}, \quad (2.3)$$

are used as governing equations. As implied by Eq. (2.2), gravity effects are neglected. Time advancement of Eqs. (2.1) and (2.2) is made by the fractional step method⁽¹²⁾. In time splitting of Eqs. (2.2) and (2.3), the second-order Crank-Nicolson method is applied for the wall-normal second derivatives, and the second-order Adams-Bashforth method is used for other terms. The fourth-order central difference^{(13), (14)} is utilized as spatial difference for convection and diffusion terms of Eqs. (2.2) and (2.3). In the driver part, the Poisson equation for the pressure is solved by the fast Fourier transformation (FFT) in the streamwise and spanwise directions and by the tri-diagonal matrix algorithm of compact difference for wall-normal derivatives. In the ribbed channel, the Poisson equation is computed by the FFT in the spanwise direction and by the successive over-relaxation at each plane perpendicular to the spanwise axis.

Computational conditions are listed in Table 2.1. The rib height is changed in four steps ranging from $H/\delta = 0.05$ to $H/\delta = 0.4$. The Reynolds number based on the frictional velocity and the channel half width, $Re_{\tau 0}$, is set at 150 for $H/\delta = 0.05, 0.1, 0.2, 0.4$ (Cases 2, 3a-3d, 4, and 5), and at 180 for $H/\delta = 0.4$ (Case 1) which exactly corresponds to the experiment⁽⁷⁾. Air flow is assumed through the simulations, and the Prandtl number is fixed at 0.71.

Figure 2.2 shows an example of grid arrangement. As shown in this figure, numerical grids are allocated finely to the rib walls, especially dense in upstream of the front surface of the rib. Such a grid arrangement is used in order to resolve the thin boundary layer in the impinging region without numerical oscillation. For $H/\delta = 0.2$,

four kinds of computation (Cases 3a-3d) are performed with using different grid meshes (Table 2.2). Case 3a and Case 3b are simulated by the largest computational volume with the spanwise length of $L_z/\delta = 6.4$. In the former and the latter, grid numbers are $(128+320) \times 185 \times 256$ and $(64+320) \times 98 \times 128$, respectively. Case 3c is computed by the reduced domain, where the spanwise length is a half of Case 3a or 3b ($L_z/\delta = 3.2$), and grid resolution is $(64+320) \times 98 \times 64$. Case 3d is also computed by the reduced domain, having sparser grids in the streamwise direction than Case 3c. Figures 2.3 and 2.4 show distributions of the skin friction coefficient and the Nusselt number, respectively, for Cases 3a-3d. There is almost no essential difference occurring from changes in the domain size or the grid arrangement. It is thus suggested that the domain size is enough large with sufficient resolution of grids through Cases 3a-3d. As suggested in Table 2.2, simulations for Cases 1, 2, 4, and 5 are made by the reduced domain with grid resolution as fine as Case 3b or 3c to save the computational load.

Table 2.1 Computational conditions.

	Case 1	Case 2	Case 3a-3d	Case 4	Case 5
H/δ	0.4	0.4	0.2	0.1	0.05
W/δ	0.4	0.4	0.2	0.2	0.2
$Re_{\tau 0}$	180	150	150	150	150
$H^{(+)}$	72	60	30	15	7.5
Pr	0.71	0.71	0.71	0.71	0.71

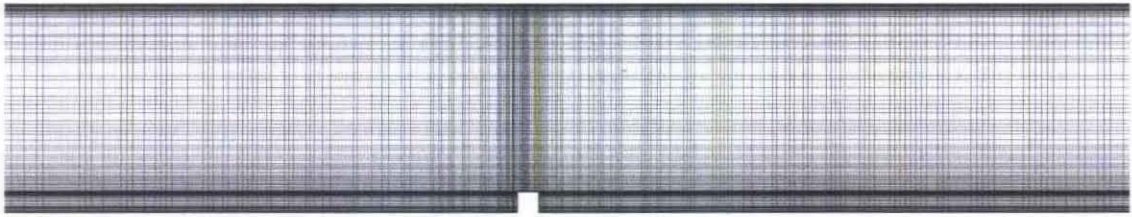


Fig. 2.2 Grid arrangement near rib for Case 3a.

Table 2.2 Computational domain and grid arrangement.

	Case 1	Case 2	Case 4	Case 5
L_{x0}/δ	8	8	8	8
L_x/δ	26.6	22.9	13.4	13.4
L_u/δ	9	5	5	5
L_z/δ	3.2	3.2	3.2	3.2
N_{x0}	128	64	64	64
N_x	580	512	320	320
N_y	128	128	98	98
N_z	128	64	64	64
$\Delta x_0^{(+)}$	11.3	18.8	18.8	18.8
$\Delta x^{(+)}$	1.13-11.3	0.938-14.1	0.938-14.1	0.938-14.1
$\Delta y^{(+)}$	1.13-7.34	0.938-6.12	0.938-10.0	0.938-10.0
$\Delta z^{(+)}$	4.50	7.50	7.50	7.50
$\Delta t^{(+)}$	0.00720	0.00600	0.0120	0.0120
	Case 3a	Case 3b	Case 3c	Case 3d
L_{x0}/δ	16	8	8	8
L_x/δ	11.0	13.4	13.4	14.3
L_u/δ	5	5	5	5
L_z/δ	6.4	6.4	3.2	3.2
N_{x0}	128	64	64	64
N_x	320	320	320	320
N_y	185	98	98	98
N_z	256	128	64	64
$\Delta x_0^{(+)}$	18.8	18.8	18.8	18.8
$\Delta x^{(+)}$	0.938-9.38	0.938-14.1	0.938-14.1	1.88-14.1
$\Delta y^{(+)}$	0.300-6.00	0.938-10.0	0.938-10.0	0.938-10.0
$\Delta z^{(+)}$	3.75	7.50	7.50	7.50
$\Delta t^{(+)}$	0.00600	0.0120	0.0120	0.0120

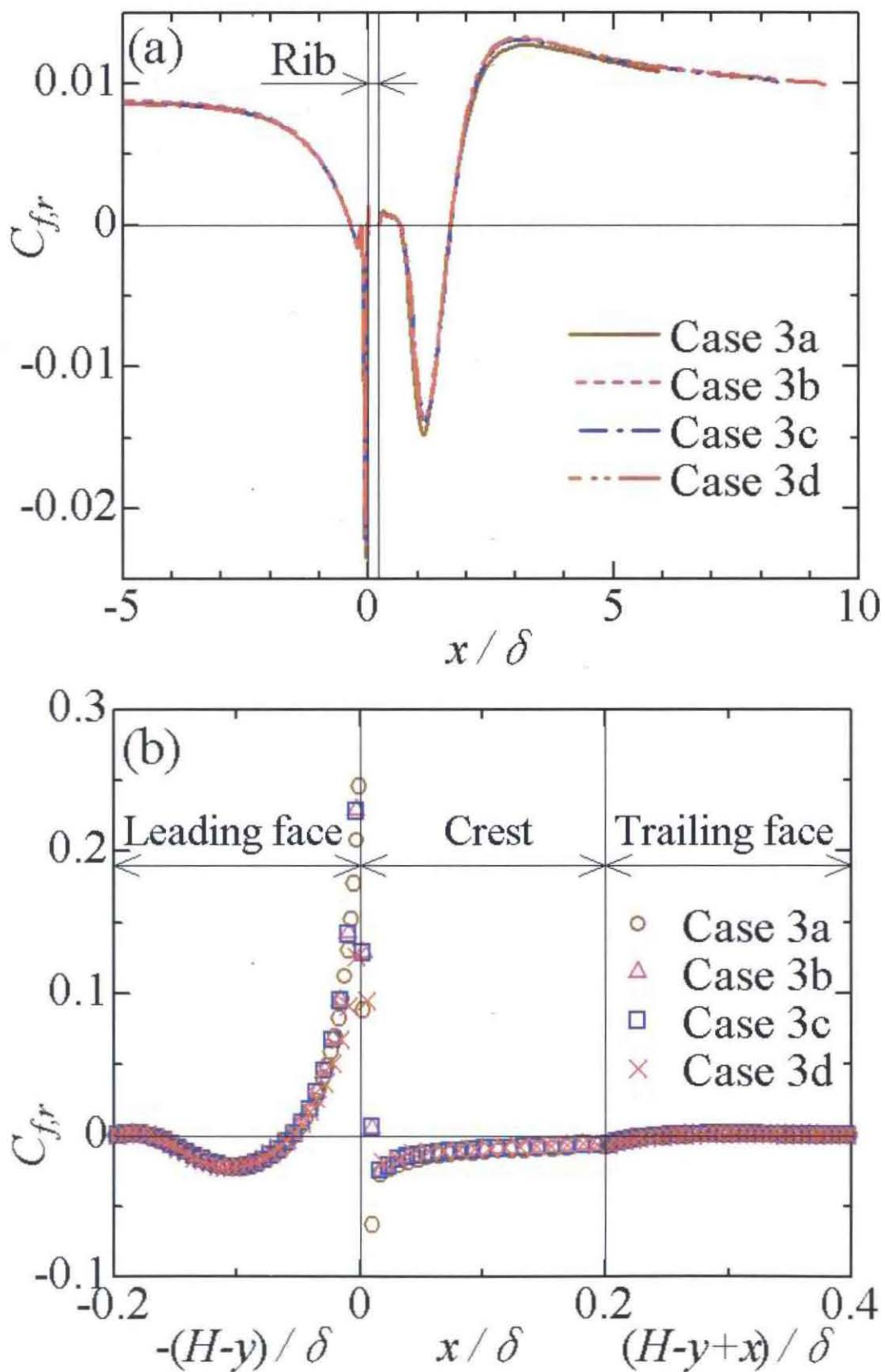


Fig. 2.3 Local skin friction coefficient: (a) bottom wall; (b) rib.

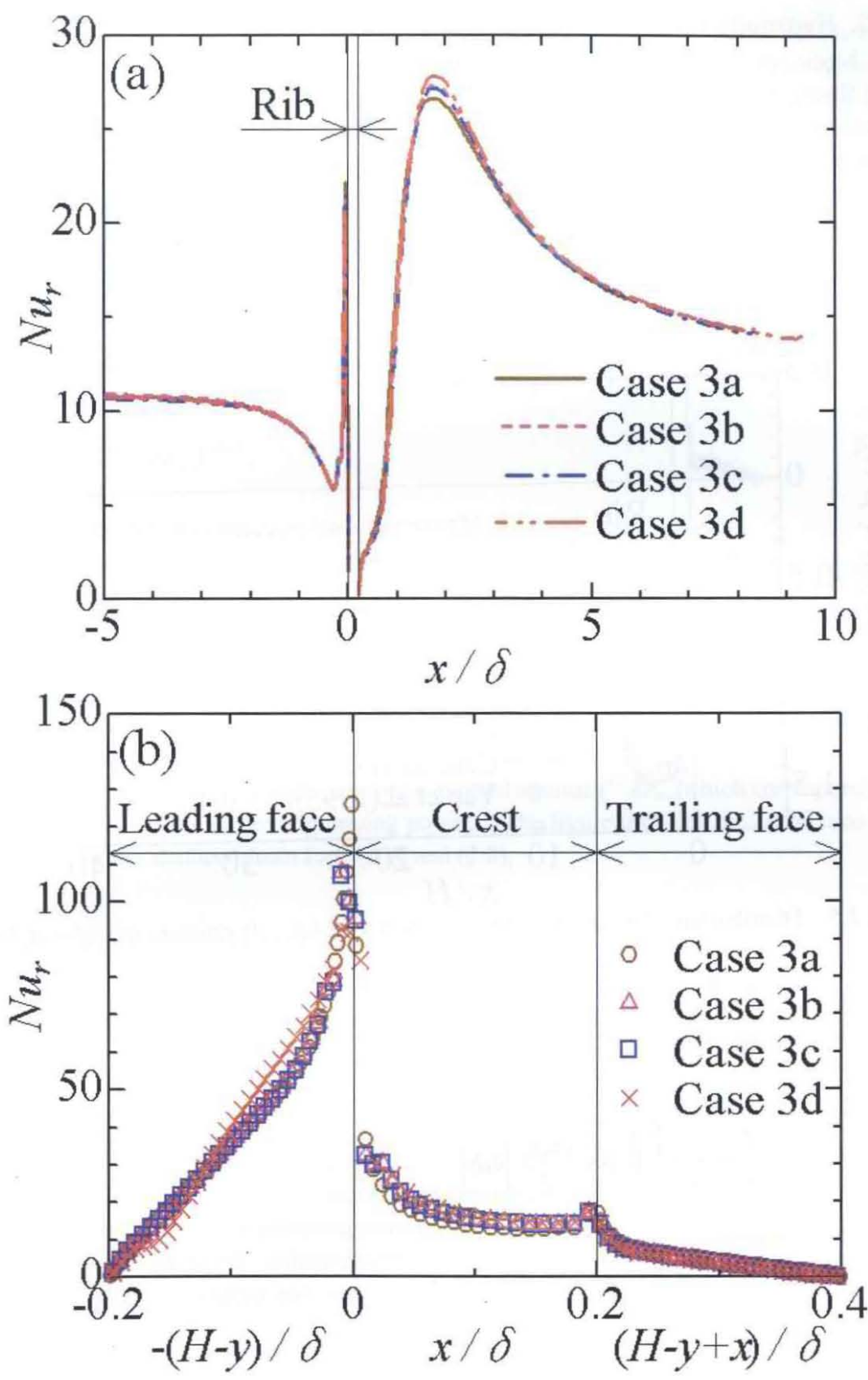


Fig. 2.4 Local Nusselt number: (a) bottom wall; (b) rib.

2.3. Hydraulic Loss and Heat Transfer

Mean pressure distributions for $H/\delta = 0.2$ and $H/\delta = 0.4$ are shown in Fig. 2.5. In the figure, Case 1 for $H/\delta = 0.4$ and $Re_m = 5700$ is very close to the experiment for the same condition by Yao et al.⁽⁷⁾, and validity of the numerical data is thus confirmed. The distributions for Case 1 and Case 2 are agreed, regardless of the Reynolds number. This has been also observed in the experiment by Yao et al. In all the presented cases, there are pressure drops due to the blockage effect from the rib, and the mean values show transitional variation in the upstream and downstream region between $-5 \leq x/H \leq 30$.

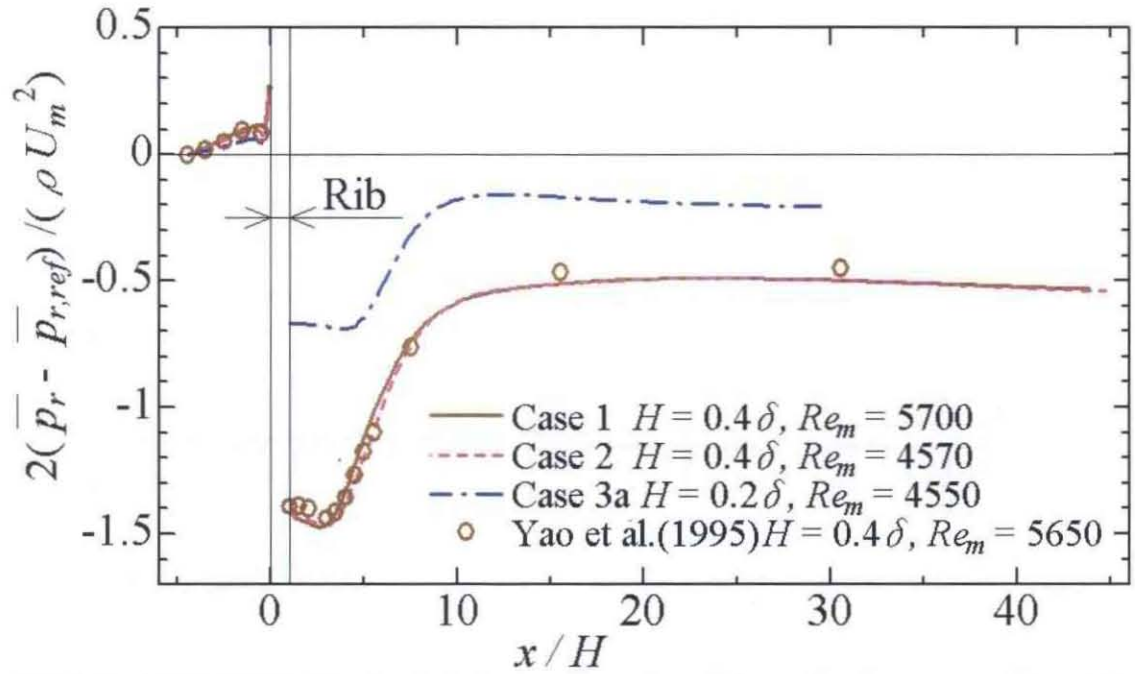


Fig. 2.5 Distribution of mean pressure on bottom wall ($\bar{p}_{r,ref}$ is pressure at $x/H = -4.5$).

Pressure loss and heat transfer in a channel are evaluated, respectively, by the apparent friction factor

$$f = \frac{1}{\rho U_m^3 (x_d - x_u)} \left\{ \int_0^{2\delta} \left(\bar{p} + \frac{\rho \bar{u}_i \bar{u}_i}{2} \right) \bar{u} dy \Big|_{x=x_u} - \int_0^{2\delta} \left(\bar{p} + \frac{\rho \bar{u}_i \bar{u}_i}{2} \right) \bar{u} dy \Big|_{x=x_d} \right\} \quad (2.4)$$

and the mean Nusselt number

$$\langle Nu \rangle = \frac{4\delta}{\lambda (T_w - T_{w,other}) (x_d - x_u)} \int_{x_u}^{x_d} \bar{q}_w d\tilde{x}, \quad (2.5)$$

where \tilde{x} denotes the streamwise direction which lines the wall shape. Therefore, heat transfer rates on the leading and trailing faces of the rib are added. The reference planes are chosen as $x_u = -20H$ and $x_d = 40H$, by which major part of the rib effects can be included in the parameters. Computed values from Eqs. (2.4) and (2.5) are shown in Figs. 2.6 and 2.7, respectively. The former presents experimental correlation for a smooth channel by Dean⁽¹⁵⁾

$$f = 0.073 Re_m^{-0.25} \quad (2.6)$$

and the Blasius's law⁽¹⁶⁾

$$f = 0.079(2 Re_m)^{-0.25}, \quad (2.7)$$

and the latter indicates the correlation by Tsukahara et al.⁽¹⁷⁾

$$Nu = 0.014 Re_m^{0.8} Pr^{0.5}. \quad (2.8)$$

In Fig. 2.6, the friction coefficient on the flat surface is doubled by the highest rib ($H/\delta = 0.4$). However, in Fig. 2.7, even maximum of the mean Nusselt number does not reach twice of the flat-plate value.

In Fig. 2.8, the mean Nusselt number is plotted against $f^{1/3} Re_m$, which corresponds to cubic root of non-dimensional pumping power. The figure includes the correlation for flat-plate values deduced from Eqs. (2.6) and (2.8),

$$Nu = 0.03 Pr^{0.5} (f^{1/3} Re_m)^{48/55} \quad (2.9)$$

and that from Eqs. (2.7) and (2.8),

$$Nu = 0.0308 Pr^{0.5} (f^{1/3} Re_m)^{48/55}. \quad (2.10)$$

In the figure, the mean Nusselt number on the ribbed wall is confirmed to exceed the smooth plate for the same pumping power. The enhancement ratio is 1.3 at maximum. Merit of the single-rib enhancement is thus validated for the case when the hydrodynamic loss is taken into consideration.

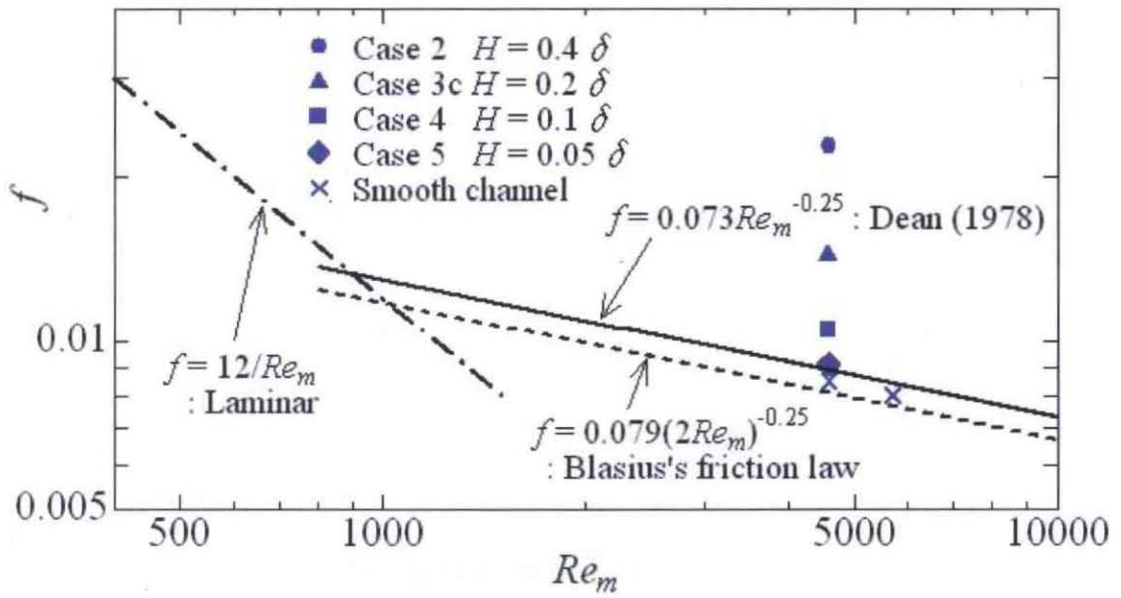


Fig. 2.6 Friction factor versus bulk Reynolds number.

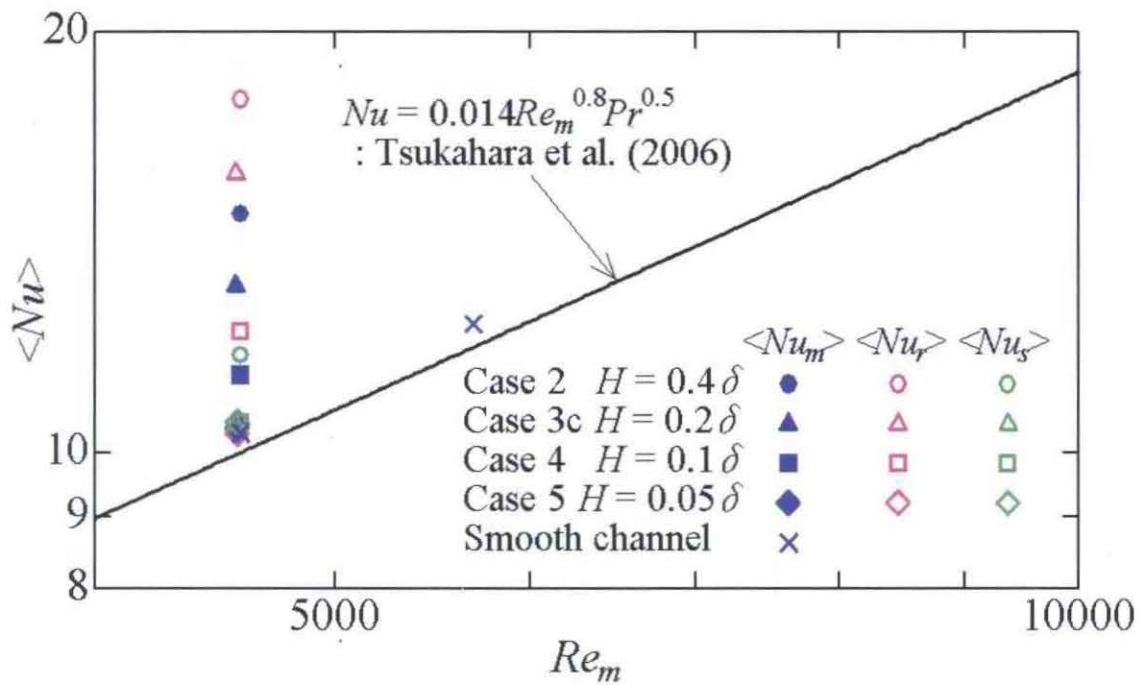


Fig. 2.7 Mean Nusselt number (on the two walls $\langle Nu_m \rangle$, on the rough-wall $\langle Nu_r \rangle$ and on the smooth-wall $\langle Nu_s \rangle$) versus bulk Reynolds number.

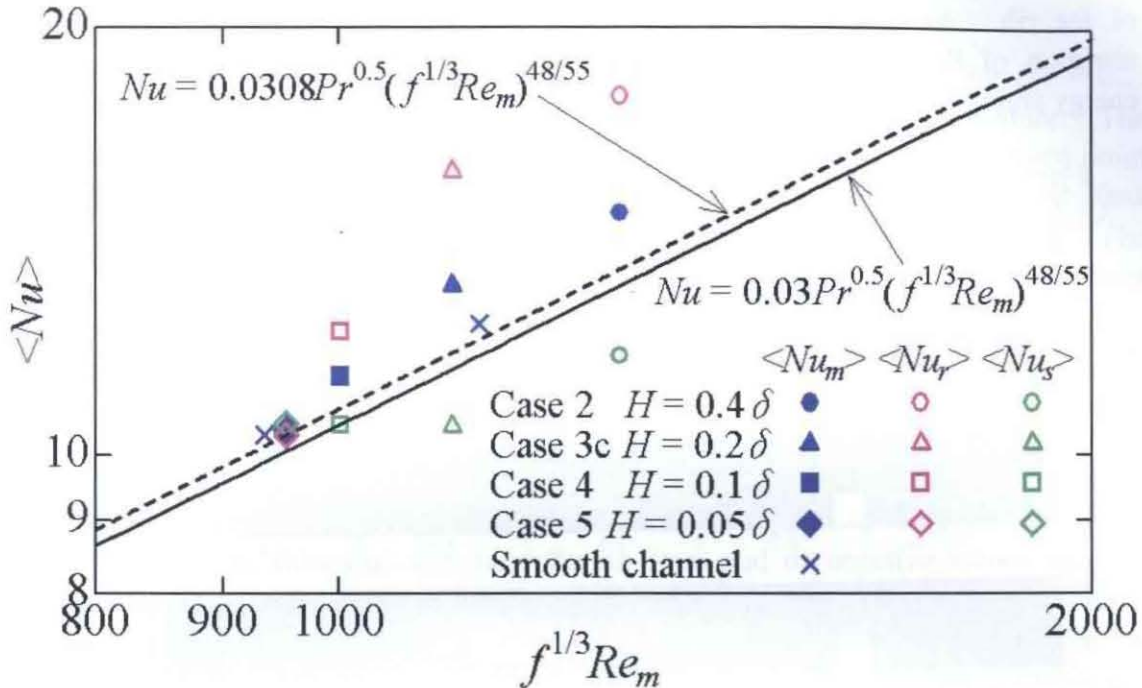


Fig. 2.8 Mean Nusselt number (on the two walls $\langle Nu_m \rangle$, on the rough-wall $\langle Nu_r \rangle$ and on the smooth-wall $\langle Nu_s \rangle$) versus pumping power.

2.4. Turbulence Statistics of Flow

In the following, attention is paid to the results from Case 3a ($H/\delta = 0.2$), where heat transfer is preferably enhanced with increasing pressure loss penalty modestly as earlier mentioned.

Figure 2.9 shows mean streamlines together with colored gradation of the mean-velocity magnitude. In this figure, circulating flows exist next to the upstream and downstream surfaces of the rib. From numerical analysis, the separated shear layer from the rib is confirmed to reattach to $x/\delta = 1.65$ on the wall, which is mostly correspond to the streamwise extent of the largest circulation as observed in the figure. In this case, the Nusselt number takes a peak at $x/\delta = 1.68$ as suggested in Fig. 2.4, and this peak position is nearly coincident with the reattachment point.

The Reynolds normal stresses and the shear stress are shown in Figs. 2.10 and 2.11, respectively. In the downstream part of the rib, there are conspicuous increase in the Reynolds stresses, which is remarkable around $1.0 < x/\delta < 2.0$ prevailing in the upstream of the reattachment position. There are also high values of Reynolds stresses in the upstream of the rib, where the streamwise stress increases at $-0.5 < x/\delta < 0$ and others are large in close vicinity of the rib front. Increases in Reynolds stresses are correlated well with high values of Nusselt number in Fig. 2.4, and the heat transfer enhancement is suggested to occur due to the turbulent fluctuation.

The mean pressure and the root mean square of the fluctuation are shown in Figs. 2.12 and 2.13, respectively. In Fig. 2.12, mean pressure suddenly drops near the front edge of the rib, which implies an acute acceleration of the flow. In Fig. 2.13, pressure fluctuation is high in the downstream of the rib and in small spots near the front surface

of the rib. As described later, such high fluctuations of pressure contribute the transport of Reynolds stresses through inter-component redistribution of turbulence energy and the pressure-assisting diffusion.

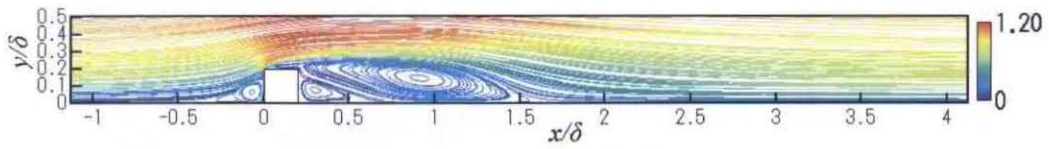


Fig. 2.9 Mean stream lines and contours of mean-velocity magnitude in Case 3a.

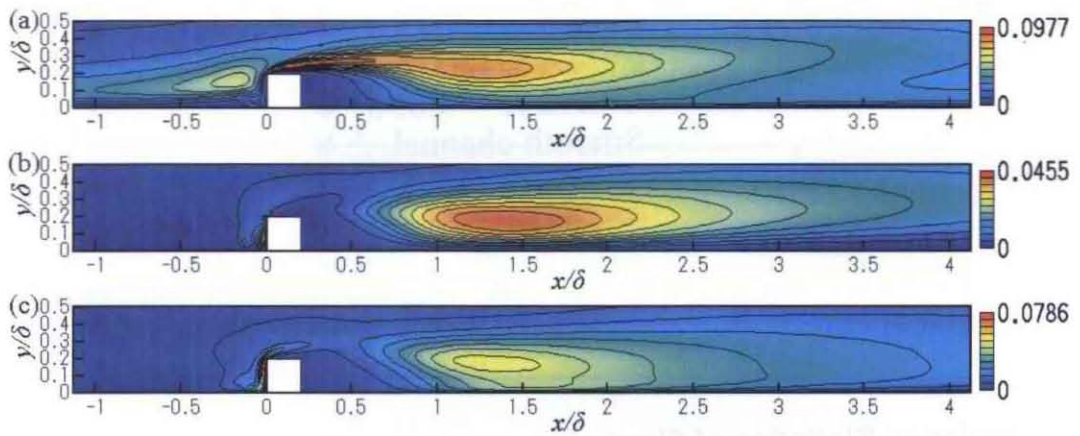


Fig. 2.10 Contours of Reynolds stress normalized by U_m^2 in Case 3a. (a) $\overline{u'u'}$; (b) $\overline{v'v'}$; (c) $\overline{w'w'}$.

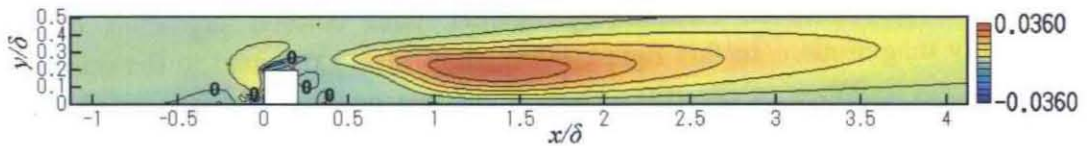


Fig. 2.11 Contours of Reynolds shear stress, $-\overline{u'v'}$, normalized by U_m^2 in Case 3a.

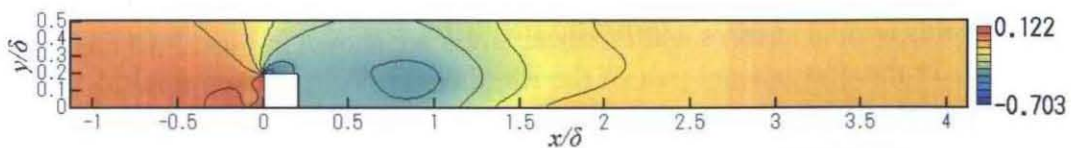


Fig. 2.12 Contours of mean pressure, $(\bar{p} - P_0) / \rho U_m^2$, in Case 3a.

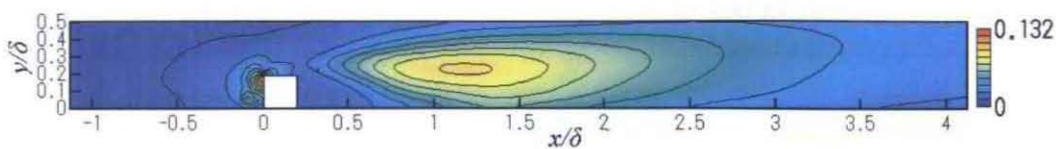


Fig. 2.13 Contours of root-mean-square pressure fluctuation normalized by ρU_m^2 in Case 3a.

2.5. Turbulence Statistics of Temperature

Examination is given to the thermal field for the same case (Case 3a for $H/\delta = 0.2$) as treated in the previous section. Figure 2.14 shows the mean temperature. The thermal boundary layer is thin near the front surface of the rib and reattachment point ($x/\delta = 1.65$). Comparison of Fig. 2.14 with Figs. 2.4 and 2.9 reveals that the flow impingements on the walls lead to thin thermal layers enhancing heat transfer. The dense distributions of thermal contours near impinging regions contrast with sparse contours away from the wall, by which turbulent transport is implied to exist.

The streamwise and wall-normal turbulent heat fluxes are presented in Fig. 2.15. In the present study, $\overline{u'\theta'} > 0$ and $\overline{v'\theta'} > 0$ express turbulent transport in positive x and y , respectively, while $\overline{u'\theta'} < 0$ and $\overline{v'\theta'} < 0$ mean transport in inverse directions. In most parts of the channel, $\overline{v'\theta'}$ shows negative values, and the turbulent heat flux is suggested to activate the heat travelling from the hotter (upper) to cooler (lower) walls. Similarly, positive values of $\overline{u'\theta'}$ near the rib front and its negative values near the back surface are consistent with heat directing to the rib surfaces. However, turbulent heat fluxes act to deteriorate the heat flow in small portions near the lower half of the rib's front surface ($\overline{u'\theta'} < 0$, Fig. 2.15(a)), its top surface ($\overline{v'\theta'} > 0$, Fig. 2.15(b)) and the channel wall just upstream of the rib front ($\overline{v'\theta'} > 0$, Fig. 2.15(b)). From Fig. 2.9, it is confirmed that such inverse contributions of turbulent heat flux tend to accompany with the separation of wall-bounded flow. Therefore, inverse contribution of turbulent motion is thought to occur in relation with bending of stream lines, which can inversely correlate flow and thermal fluctuations due to excessive convection of scalar.

Intensity of temperature fluctuation is displayed in Fig. 2.16. Temperature fluctuation is high around the rib's top surface extending between $-0.5 < x/\delta < 1.5$. This extension is broader than velocity fluctuation, $\overline{u'u'}$. This is because the thermal boundary condition adopted in this paper has the mean thermal gradient over the channel width and strong thermal fluctuation is assisted to occur through production by mean thermal gradient⁽¹⁸⁾.

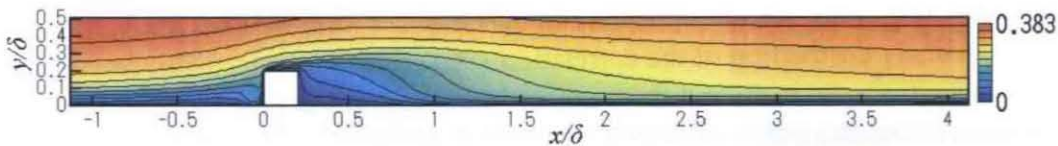


Fig. 2.14 Contours of mean temperature, $(\bar{T}-T_r)/\Delta T_w$, in Case 3a.

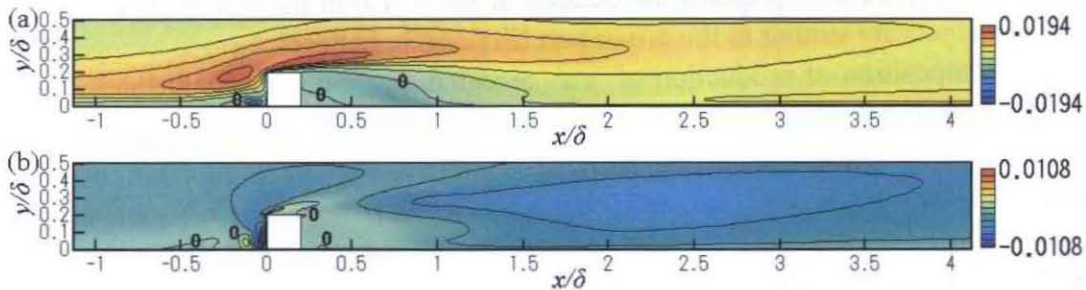


Fig. 2.15 Contours of turbulent heat flux normalized by $U_m\Delta T_w$ in Case 3a. (a) $\overline{u'\theta'}$; (b) $\overline{v'\theta'}$.

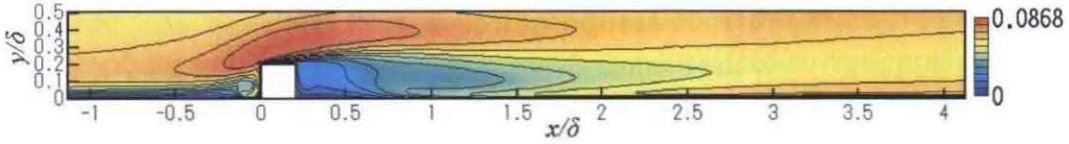


Fig. 2.16 Contours of root-mean-square temperature fluctuation normalized by ΔT_w in Case 3a.

2.6. Budgets of Reynolds Stress

Transport equations of Reynolds stresses can be written as follows:

$$\frac{\partial \overline{u_i' u_j'}}{\partial t} + \bar{u}_k \frac{\partial \overline{u_i' u_j'}}{\partial x_k} = D_{ij} + P_{ij} + \Phi_{ij} + \varepsilon_{ij}; \quad (2.11)$$

$$\text{Diffusion, } D_{ij} = \frac{\partial}{\partial x_k} \left\{ v \frac{\partial \overline{u_i' u_j'}}{\partial x_k} - \overline{u_i' u_j' u_k'} - \left(\frac{\overline{p u_j'}}{\rho} \delta_{ik} + \frac{\overline{p u_i'}}{\rho} \delta_{jk} \right) \right\}; \quad (2.12)$$

$$\text{Production, } P_{ij} = -\overline{u_j' u_k'} \frac{\partial \bar{u}_i}{\partial x_k} - \overline{u_i' u_k'} \frac{\partial \bar{u}_j}{\partial x_k}; \quad (2.13)$$

$$\text{Pressure-strain correlation, } \Phi_{ij} = \frac{p'}{\rho} \frac{\partial \bar{u}_i'}{\partial x_j} + \frac{p'}{\rho} \frac{\partial \bar{u}_j'}{\partial x_i}; \quad (2.14)$$

$$\text{Dissipation, } \varepsilon_{ij} = -2\nu \frac{\partial \bar{u}_i'}{\partial x_k} \frac{\partial \bar{u}_j'}{\partial x_k}. \quad (2.15)$$

In this section, budgets of Eq. (2.11) are presented for the Case 3a ($H/\delta = 0.2$) similarly to sections 2.4 and 2.5. Figure 2.17 shows budgets in the driver part. As explained in the earlier work⁽¹⁹⁾, budgets in the no-rib case show that redistribution of energy goes from $\overline{u'u'}$ to $\overline{v'v'}$ and $\overline{w'w'}$ through the pressure-strain correlation being finally dissipated to heat, and $\overline{u'v'}$ disappears through another role of the pressure-strain correlation, namely destruction of the correlation. In all the budgets, diffusions are not important away from the wall, and the transport processes are in near local-equilibrium in major parts of the channel.

The sampling planes for Reynolds-stress budgets in the ribbed channel are indicated in Fig. 2.18. Figure 2.19 presents the budgets at $x/\delta = -1.0$ in the ribbed channel. In Fig. 2.19, budgets are similar to the driver part (Fig. 2.17), but each term is exaggerated. Further decomposition of production of $\overline{u'u'}$ revealed that the major contribution was made by an increase of $-\overline{2u'u'\partial u/\partial x}$ rather than $-\overline{2u'v'\partial u/\partial y}$, and the exaggeration was suggested to occur due to the flow deceleration. In the production of $\overline{u'v'}$, increase of $-\overline{2u'u'\partial v/\partial x}$ was the most important among increases of $-\overline{2u'v'\partial u/\partial x}$, $-\overline{2u'u'\partial v/\partial x}$, $-\overline{2v'v'\partial u/\partial y}$ and $-\overline{2u'v'\partial v/\partial y}$, and it was suggested that displacement of mean flow increased the production.

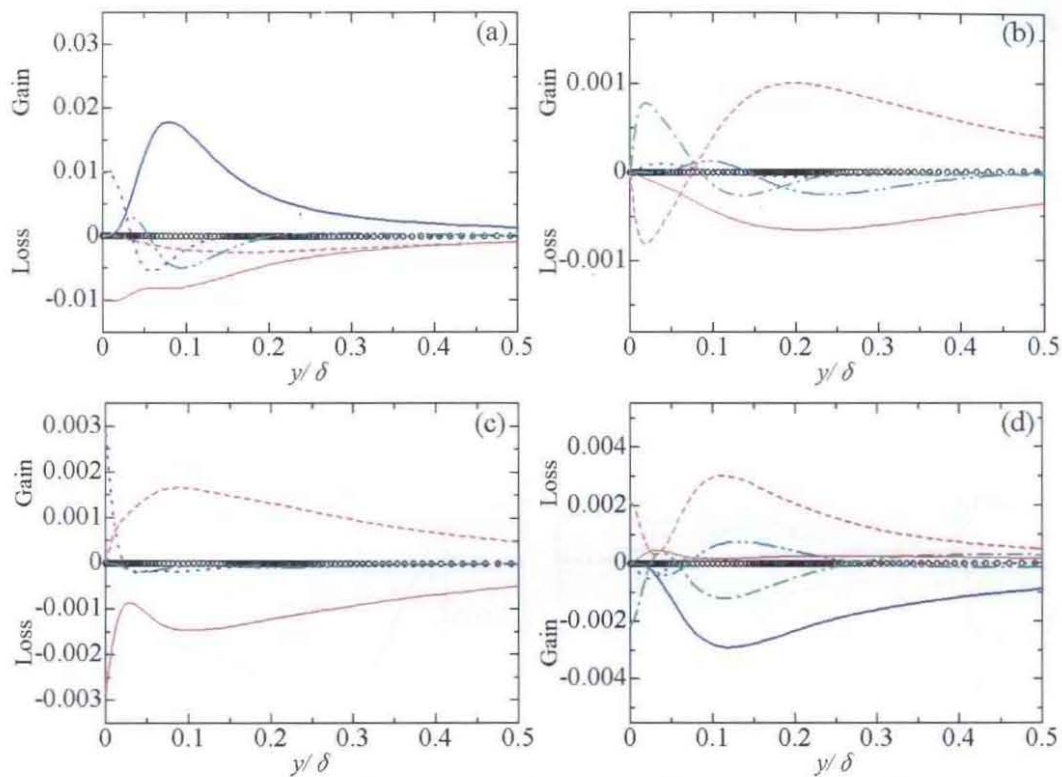


Fig. 2.17 Reynolds stress budgets normalized by U_m^3/δ in Case 3a at driver part: —, production; ----, pressure strain; - · - ·, pressure diffusion; · · · ·, turbulent diffusion; - - - -, viscous diffusion; —, dissipation; °, residual. (a) $\overline{u'u'}$; (b) $\overline{v'v'}$; (c) $\overline{w'w'}$; (d) $\overline{u'v'}$.

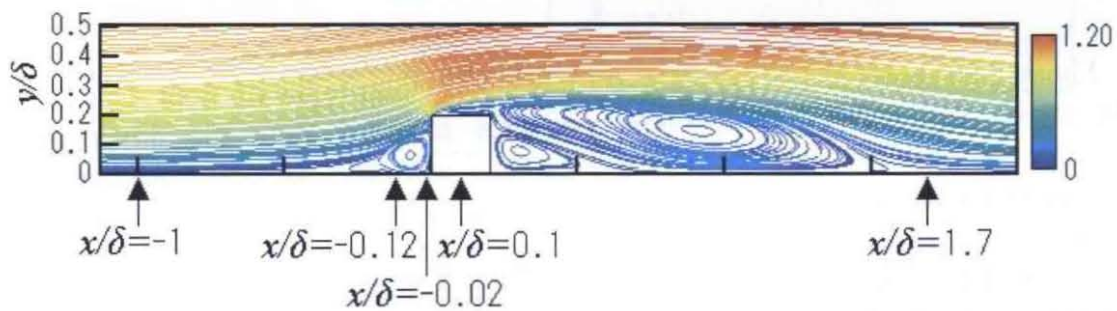


Fig. 2.18 Sampling position for Reynolds-stress budgets.

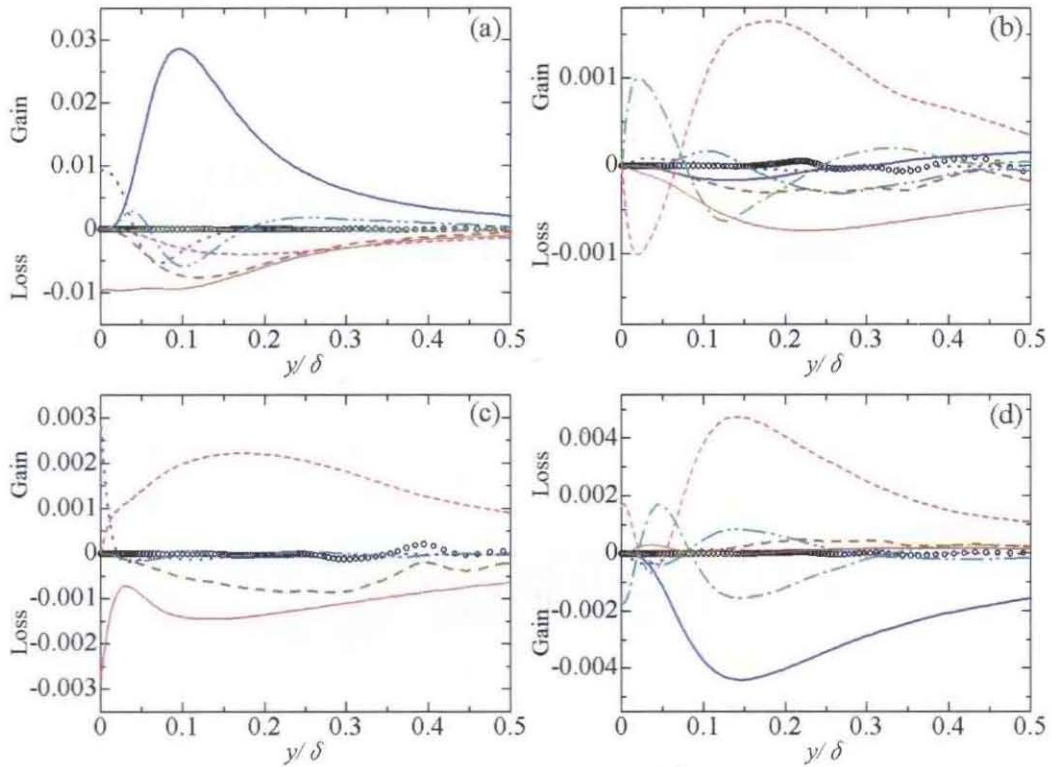


Fig. 2.19 Reynolds stress budgets normalized by U_m^3/δ in Case 3a at $x/\delta = -1$: —, production; ----, pressure strain; - · - ·, pressure diffusion; ····, turbulent diffusion; ·····, viscous diffusion; —, dissipation; ---, convection; *, residual. (a) $\overline{u'u'}$; (b) $\overline{v'v'}$; (c) $\overline{w'w'}$; (d) $\overline{u'v'}$.

Figure 2.20 shows budgets at $x/\delta = -0.12$, which is closer to the rib front. This plane still shows the essence of transport structures inherited from the driver part: redistribution occurs from $\overline{u'u'}$ to $\overline{v'v'}$ and $\overline{w'w'}$; $\overline{u'v'}$ is destroyed by the pressure-strain correlation. However, each term of budgets is more complex than the far-field due to the circulating flow neighboring the rib front. The diffusion terms (turbulent diffusion, pressure diffusion and viscous diffusion) are remarkable, and spatial transport is thus strong near the rib surface. In most parts of normal-stress budgets, diffusion terms or convections are larger than dissipation, and transport mechanisms are far from the local equilibrium.

Budgets at $x/\delta = -0.02$ are shown in Fig. 2.21. In the figure, pressure-strain correlations are huge in budgets of normal stresses, and the flow splatting to the front wall is suggested to promote the redistribution. Negative values in the production of $\overline{u'u'}$ and those in $\overline{v'v'}$ were confirmed to occur due to the flow acceleration. This acceleration was thought to occur based on the flow contraction near the rib corner and the impingement to the rib front. In all the budgets, diffusions or convection are important compared with the driver part, and the spatial transport is thus signified near the vertical wall.

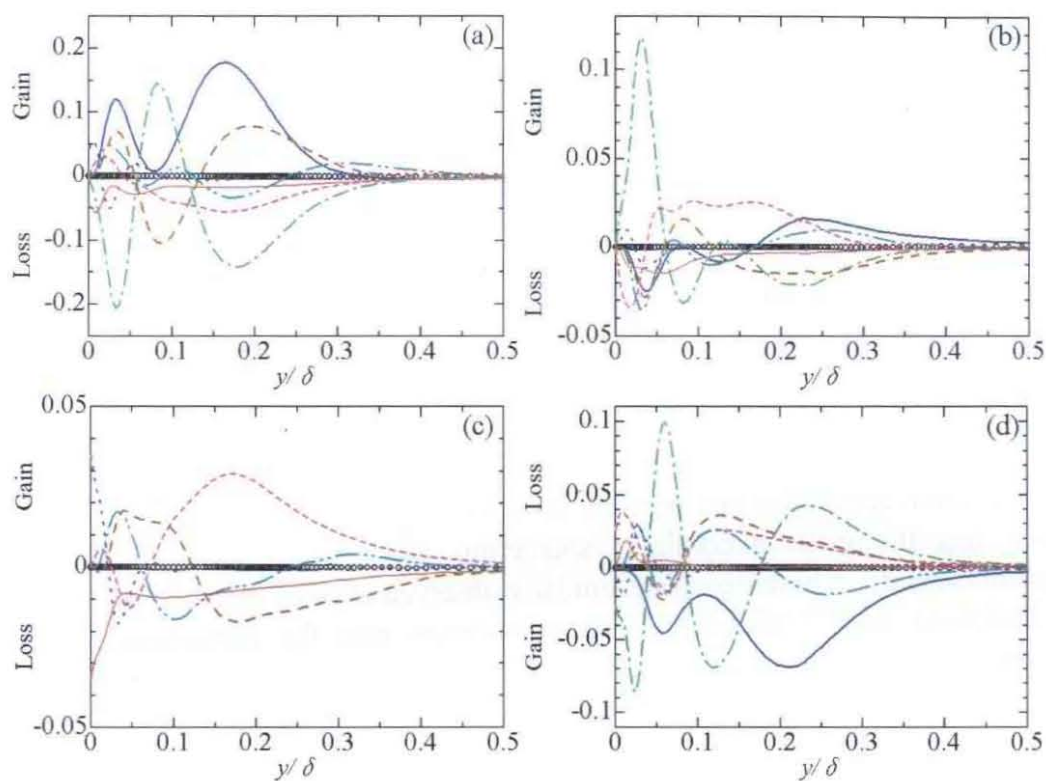


Fig. 2.20 Reynolds stress budgets at $x/\delta = -0.12$ with the same captions as Fig. 2.19.

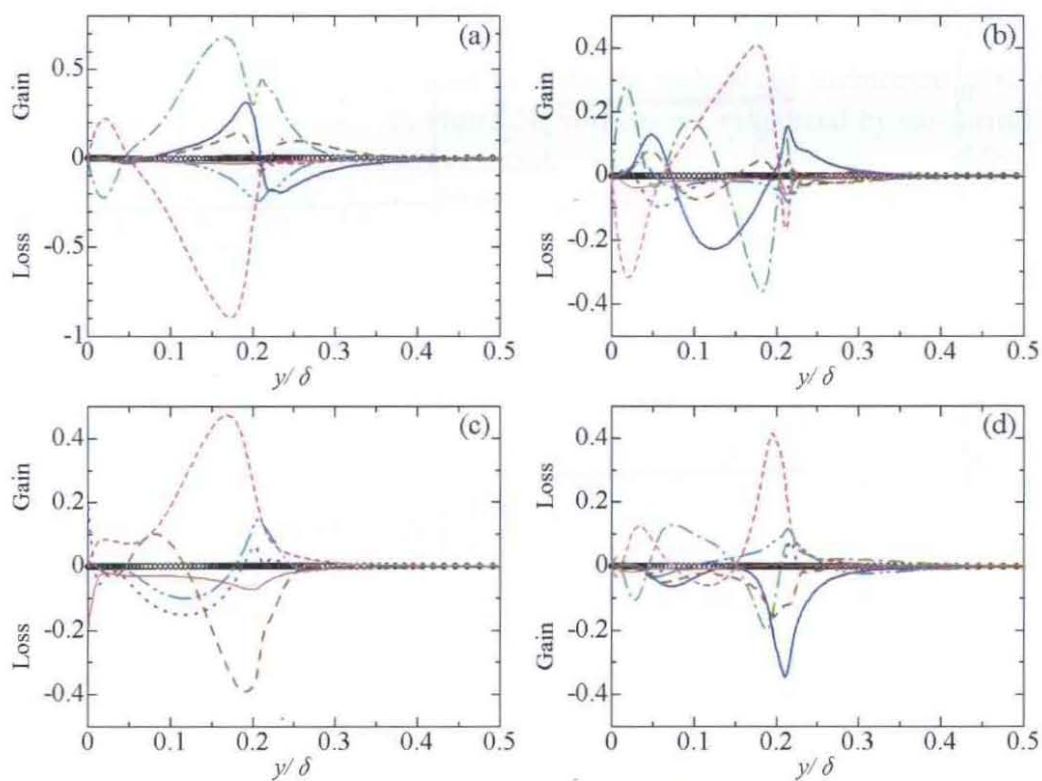


Fig. 2.21 Reynolds stress budgets at $x/\delta = -0.02$ with the same captions as Fig. 2.19.

In Fig. 2.22, budgets at $x/\delta = 0.1$ are depicted. At this plane, gain by the production and loss by the convection are important in the budget of $\overline{u'u'}$. Pressure-strain correlation is small in the budgets of normal stresses, and the redistribution is shown to be minor. In budgets of $\overline{v'v'}$ and $\overline{w'w'}$, the convection and diffusions are important, and diffusions transport stresses away from the wall. These are consistent with modest values of $\overline{v'v'}$ and $\overline{w'w'}$ near the top wall of the rib compared with $\overline{u'u'}$ as shown in Fig. 2.10.

Figure 2.23 shows the plane near the reattachment point, namely $x/\delta = 1.7$. Near the reattachment point, redistribution occurs in normal stresses and contributions from turbulent diffusion are conspicuous in budget of $\overline{v'v'}$. Production of $\overline{v'v'}$ is high near the wall due to the deceleration of wall-normal velocity, and this contributes the high fluctuation which enhances scalar transport. There are remarkable contributions from pressure-strain correlation and pressure diffusion of $\overline{v'v'}$, and contributions from those of $\overline{u'v'}$ near the wall. Accordingly, splattering effects are suggested to occur due to the reattachment. These trends are similarly observed in cases of periodic fences⁽⁸⁾ and the backward step⁽¹¹⁾, and the transport processes near the reattachment point are analogous in separated flows.

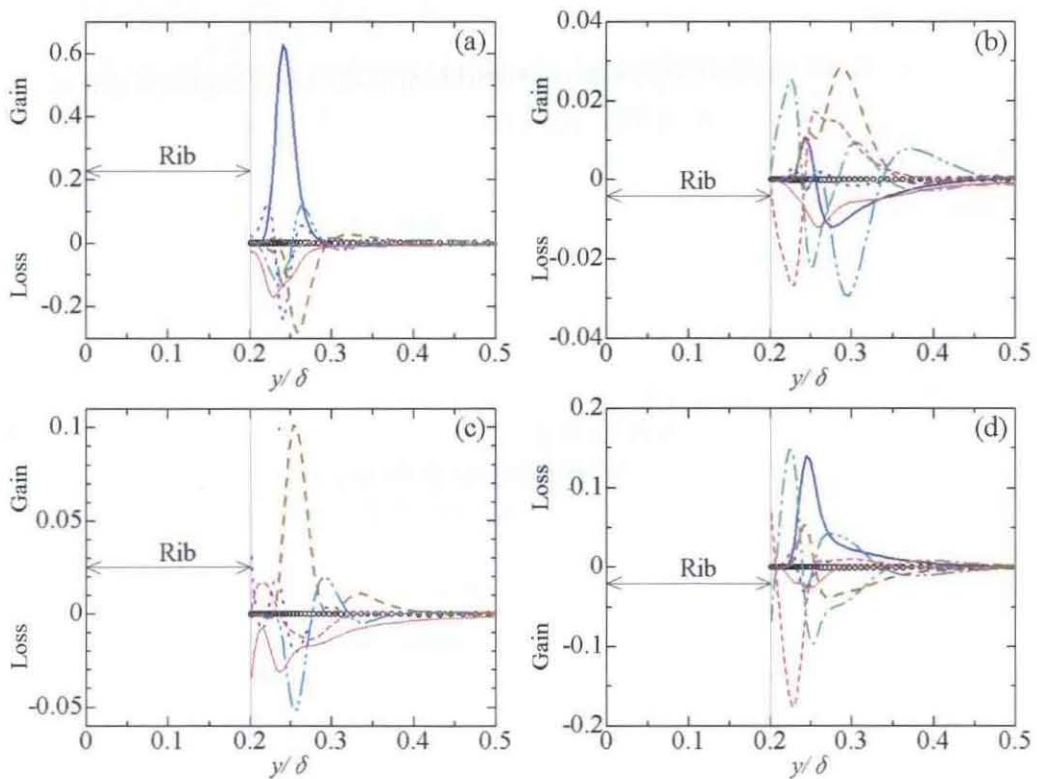


Fig. 2.22 Reynolds stress budgets at $x/\delta = 0.1$ with the same captions as Fig. 2.19.

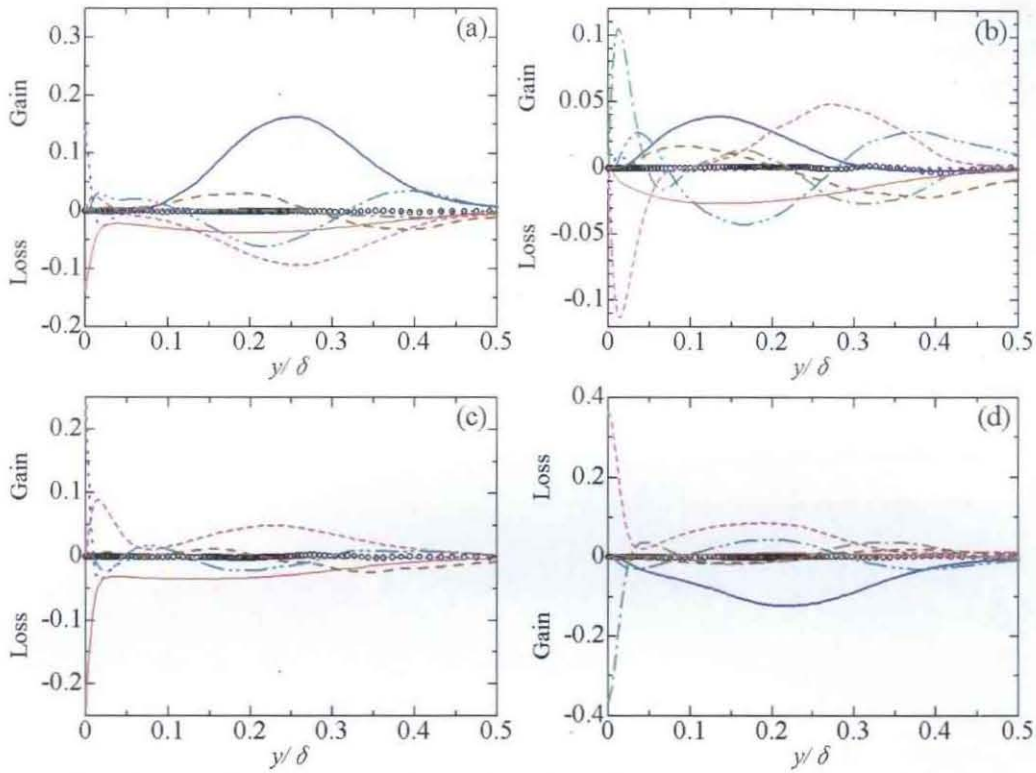


Fig. 2.23 Reynolds stress budgets at $x/\delta = 1.7$ with the same captions as Fig. 2.19.

2.7. Structures of Instantaneous Field

An instantaneous flow is examined in order to understand turbulence structures related to the transport process. In Fig. 2.24, vortices are visualized by iso-surfaces of the second invariant for the deformation tensor

$$Q = -\frac{1}{2} \frac{\partial u_i}{\partial x_j} \frac{\partial u_j}{\partial x_i}, \quad (2.16)$$

where the iso-surfaces are colored by

$$Q_z = -\frac{1}{2} \left\{ \left(\frac{\partial u}{\partial x} \right)^2 + 2 \frac{\partial u}{\partial y} \frac{\partial v}{\partial x} + \left(\frac{\partial v}{\partial y} \right)^2 \right\} \quad (2.17)$$

to detect the spanwise rotation. The figure includes contours of streamwise velocity fluctuation. In the upstream of the rib, there are stripes of alternating low-speed streaks and high-speed islands, and streaky structures are branched as approaching the rib wall. The branching of structures is implied to occur due to flow deceleration, and this is suggested to correspond to turbulence enhancement described in the previous section. Near the front surface of the rib, longitudinal structures are rooted to streaks and stretched to the upper-downstream direction, which implies energy redistribution occurring from streamwise to secondary directions through longitudinal vortices.

There are longitudinal and spanwise structures near the top wall of the rib, and three-dimensional disturbance is suggested to occur in the mean flow. Behind the rib, instability in the shear layer is highly complex and fully three-dimensional, and three-dimensionality near the rib corner is suggested to trigger smooth transition.

Comparison between Figs. 2.24 and 2.4 reveals that high performance of heat transfer can be attributed to hydrodynamic mechanisms leading to strong fluctuation. Turbulence near the front surface of the rib is intensified due to flow deceleration, and three-dimensionality near the rib corner induces fast transition of separated shear layer. These structures are thought to induce powerful fluctuations near the wall, and activated transport of scalar is suggested to cause high values of Nusselt number.

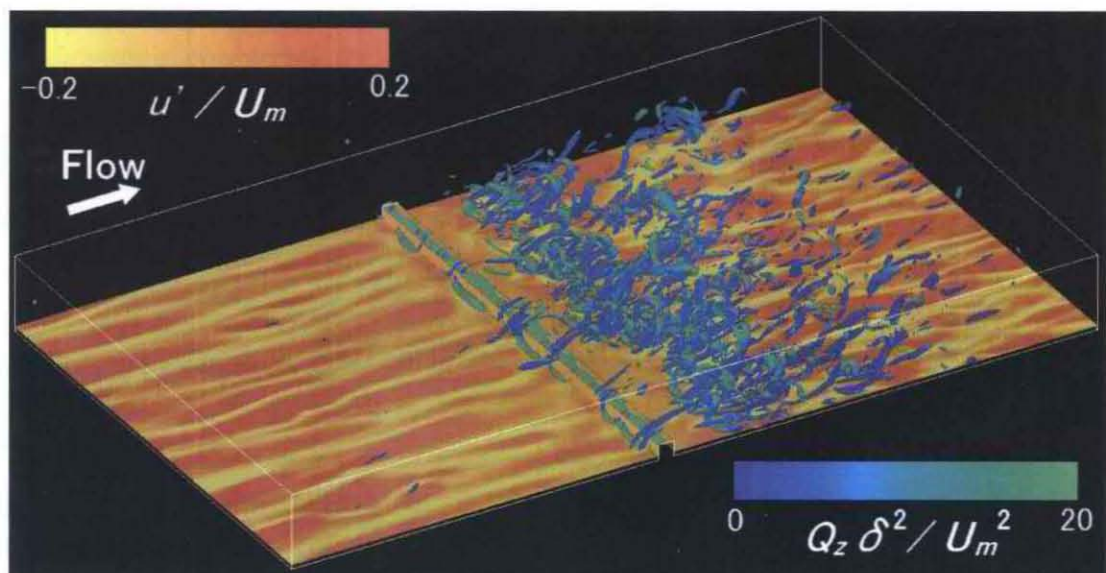


Fig. 2.24 Iso-surfaces of the second-invariant ($Q\delta^2/U_m^2 = 20$) with Q_z and contours of streamwise velocity fluctuation at $y/\delta \approx 0.05$ in Case 3a.

2.8. Conclusions

Direct numerical simulation was performed for air flows and related heat transfer in a channel with a single rib attached to the channel wall. The rib height was changed at $H/\delta = 0.05, 0.10, 0.20, 0.40$ for the frictional Reynolds number, $Re_{\tau 0}$, fixed at 150. Conclusions thus extracted are as follows.

- For cases of $H/\delta = 0.2$, four kinds of computation were made with changing spanwise length of computational domain and grid arrangement. Computational results from these simulations show almost no difference, and there was essentially no dependence on domain size and grids. In addition, in the case of the highest rib ($H/\delta = 0.4$), there was close agreement of the mean pressure between the computation and the existing experiment.
- The mean Nusselt number on the ribbed wall was about 1.3 times as large as the smooth wall for the same pumping power. Single rib mounted on the wall was thus meaningful as a heat-transfer-enhancement technique.

- The Reynolds normal stress was high near the front surface of the rib and around the reattachment region, which was well correlated with high values of the Nusselt number. The streamwise and wall-normal turbulent heat fluxes were mostly consistent with enhancing heat transfer on the wall.
- Budgets of Reynolds stresses revealed transport mechanisms: (1) The flow deceleration in the upstream of the rib results in the enhancement of streamwise normal stress; (2) Near the front surface of the rib, redistribution from streamwise to wall-normal and spanwise stresses were large due to splatting effect; (3) Near the reattachment point, production of wall-normal stress is high, and this enhances fluctuation by which heat transport is activated.
- Instantaneous iso-surfaces of second invariant for deformation tensor and contours of streamwise fluctuation revealed: (1) The low-speed streaks branched as the flow approached the rib front surface, which was implied to enhance turbulence through accumulating fluctuations; (2) Near the leading edge of the rib, longitudinal eddies resulted in three-dimensional disturbance of the shear layer, corresponding to activation of redistribution; (3) In the downstream of the rib, there was highly three-dimensional turbulence in the separated shear layer.
- Comparison between an instantaneous flow and distributions of the Nusselt number indicated that streamwise fluctuation near the rib's front surface and fully developed turbulence in the separated shear layer are correlated well with high values of the Nusselt number. Therefore, high performance of heat transfer in the ribbed channel is attributed to the mechanisms to induce strong fluctuation.

2.9. References

- (1) Lewis, M. J., Optimising the thermohydraulic performance of rough surfaces, *International Journal of Heat and Mass Transfer*, Vol. 18 (1975), pp.1243-1248.
- (2) Miyake, Y., Tsujimoto, K. and Nakaji, M., Direct numerical simulation of rough-wall heat transfer in a turbulent channel flow, *International Journal of Heat and Fluid Flow*, Vol. 22 (2001), pp.237-244.
- (3) Leonardi, S., Orlandi, P., Smalley, R. J., Djenidi, L. and Antonia, R. A., Direct numerical simulations of turbulent channel flow with transverse square bars on one wall, *Journal of Fluid Mechanics*, Vol. 491 (2003), pp.229-238.
- (4) Leonardi, S., Orlandi, P., Djenidi, L. and Antonia, R. A., Structure of turbulent channel flow with square bars on one wall, *International Journal of Heat and Fluid Flow*, Vol. 25 (2004), pp.384-392.
- (5) Nagano, Y., Hattori, H. and Houra, T., DNS of velocity and thermal fields in turbulent channel flow with transverse-rib roughness, *International Journal of Heat and Fluid Flow*, Vol. 25 (2004), pp.393-403.
- (6) Suzuki, H., Suzuki, K. and Sato, T., Dissimilarity between heat and momentum transfer in a turbulent boundary layer disturbed by a cylinder, *International Journal of Heat and Mass Transfer*, Vol. 31 (1988), pp.259-265.

- (7) Yao, M., Nakatani, M. and Suzuki, K., Flow visualization and heat transfer experiments in a turbulent channel flow obstructed with an inserted square rod, *International Journal of Heat and Fluid Flow*, Vol. 16 (1995), pp.389-397.
- (8) Makino, S., Iwamoto, K. and Kawamura, H., Turbulent structures and statistics in turbulent channel flow with two-dimensional slits, *International Journal of Heat and Fluid Flow*, Vol. 29 (2008), pp.602-611.
- (9) Orellano, A. and Wengle, H., Numerical simulation (DNS and LES) of manipulated turbulent boundary layer flow over a surface-mounted fence, *European Journal of Mechanics, B/Fluids*, Vol. 19 (2000), pp.765-788.
- (10) Yakhot, A., Liu, H. and Nikitin, N., Turbulent flow around a wall-mounted cube: A direct numerical simulation, *International Journal of Heat and Fluid Flow*, Vol. 27 (2006), pp.994-1009.
- (11) Le, H., Moin, P. and Kim, J., Direct numerical simulation of turbulent flow over a backward-facing step, *Journal of Fluid Mechanics*, Vol. 330 (1997), pp.349-374.
- (12) Kim, J. and Moin, P., Application of a fractional step method to incompressible Navier-Stokes Equations, *Journal of Computational Physics*, Vol. 59 (1985), pp.308-323.
- (13) Matsubara, K., Kobayashi, M. and Maekawa, H., Direct numerical simulation of a turbulent channel flow with a linear spanwise mean temperature gradient, *International Journal of Heat and Mass Transfer*, Vol. 41 (1998), pp.3627-3634.
- (14) Matsubara, K., Kobayashi, M., Sakai, T. and Suto, H., A study on spanwise heat transfer in a turbulent channel flow –eduction of coherent structures by a conditional sampling technique–, *International Journal of Heat and Fluid Flow*, Vol. 22 (2001), pp.213-219.
- (15) Dean, R. B., Reynolds number dependence of skin friction and other bulk flow variables in two-dimensional rectangular duct flow, *Transactions of the ASME, Journal of Fluids Engineering*, Vol. 100 (1978), pp.215-223.
- (16) Bejan, A., *Convection Heat Transfer*, 2nd edition, (1995), John Wiley and Sons, Inc.
- (17) Tsukahara, T., Iwamoto, K., Kawamura, H. and Takeda, T., DNS of heat transfer in a transitional channel flow accompanied by a turbulent puff-like structure, *Proceedings of 5th International Symposium on Turbulence, Heat and Mass Transfer*, (2006), pp.193-196.
- (18) Matsubara, K., Matsui, A., Miura, T., Sakurai, A., Suto, H. and Kawai, K., A spatially advancing turbulent flow and heat transfer in a curved channel, *Heat Transfer-Asian Research*, Vol. 39 (2010), pp.14-26.
- (19) Mansour, N. N., Kim, J. and Moin, P., Reynolds-stress and dissipation-rate budgets in a turbulent channel flow, *Journal of Fluid Mechanics*, Vol. 194 (1988), pp.15-44.

Chapter 3 Transport Dissimilarity

3.1. Introduction

Elementary steps in energy conversion and chemical processing often evolve turbulent heat transfer, requiring heat removal by moderate pumping loss penalty. Naturally the global design of a particular system decides majority of its thermo-hydrodynamic performance, but modification of the flow by means of a surface roughness or protrusion is known to dramatically improve characteristics of some applications. For example, internally roughened tubes are used for a heat exchanger of refrigerators to disturb the interior refrigerant, which reduce thermal resistance from the near-wall stagnation and contribute to shorten the heat transfer length. There have been compilation of academic studies treating wall roughness which contacts a turbulent flow (for example see Lewis⁽¹⁾), and readers can access mean properties of flow and temperature restricted conditions. However, it still needs try and errors to improve surface roughness or a protrusion for efficient destabilization of wall-bounded flows, because the past studies mostly collect the bulk features for cases with the surface roughness but lacking ample knowledge on phenomenology leading to the guideline for constructing the strategy of flow and thermal control.

Research by Suzuki et al.⁽²⁾ and his colleagues can be raised as efforts to fill in the vacancy. Suzuki et al. found that heat transfer enhancement and wall friction reduction simultaneously occurred in the turbulent boundary layer disturbed by a cylinder. They made octant analysis for experimental data from a hot wire anemometry, and pointed out that the outward and wallward interactions contributed to reducing the Reynolds shear stress and increasing the turbulent heat flux over the heated wall. Yao et al.^{(3),(4)} visualized the channel turbulent flow inserted by a square rod, and clarified that the Karman vortex street correlates well with the heat transfer enhancement. Inaoka et al.⁽⁵⁾ applied the Reynolds averaged Navier-Stokes (RANS) model to simulate the turbulent boundary layer disturbed by a square rod. Their two-dimensional time-dependent analysis envisioned roles of the Karman vortices which suppress the wall friction and enhance heat transfer simultaneously to result in the transport dissimilarity between momentum and heat.

In spite of previous efforts, there is still ambiguity in mechanisms leading to the transport dissimilarity. So far, the limitation of experimental technique averted full access to the concerned flow and thermal fields, and the turbulence model adopted by the simulation may blur the predicted structures. Furthermore, existing literatures on the transport dissimilarity mainly treated floated obstacles and eluded a more practical situation where the surface roughness or protrusion is on the wall surface. Recently, Miyake et al.⁽⁶⁾ and Nagano et al.⁽⁷⁾ directly solved basic equations for the channel turbulence with periodic square ribs protruded from the wall. Yang and Ferziger⁽⁸⁾, Orellano and Wengle⁽⁹⁾, Yakhot et al.⁽¹⁰⁾, and Makino et al.⁽¹¹⁾ similarly treated the channel flow with an isolated rib protrusion. However, these efforts focused on fundamental fluid dynamics, and the analysis on heat transfer is still scarce. It is

expected to explore detailed mechanisms of the transport dissimilarity in the case of protruded rib, since such knowledge is thought to enlighten the more efficient way for controlling turbulent heat transfer.

The present paper performs direct numerical simulation (DNS) of the turbulent channel flow with an isolated rib attached to one wall, and aims to reveal mechanisms causing the dissimilarity between momentum and heat transport based on a complete set of time series of three-dimensional data. The present author treated the same flow in the previous chapter, and examined heat transfer characteristics and turbulence statistics including the Reynolds stress budgets. This previous study set two walls at different temperatures, where the transport dissimilarity appeared vaguely. The present chapter treats various thermal conditions, and mainly maintains two walls at the same temperature enabling to clearly present the transport dissimilarity. This investigation firstly reports on hydrodynamic loss and heat transfer characteristics of the concerned case. This chapter then examines instantaneous structures of flow and thermal fields to reveal background physics behind the dissimilarity between the momentum and heat transport. Furthermore, the study expands the Reynolds shear stress and turbulent heat flux into the cross spectral density to examine the spectral dissimilarity, and analyzes the fractional contribution to these quantities from the octant events to compare with other sources for a floated obstacle.

3.2. Numerical Methods

Figure 3.1 shows the computational domain and the coordinate system. The computational object and the numerical methods for the flow fields are the same as Chapter 2.

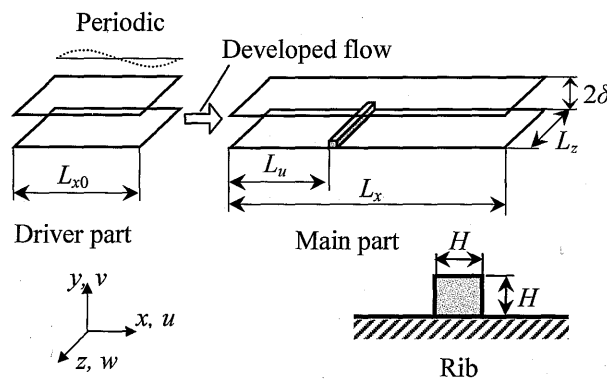


Fig. 3.1 Computational domain and coordinate system.

This chapter treats two thermal conditions for the ribbed channel; CT (Constant Temperature Walls) and CTD (Constant Temperature Difference between Two Walls), and four conditions for the smooth channel; CT, CTD, CF (Constant Heat Flux) and CAF (Constant Time-Averaged Heat Flux). In CT, the main channel maintains a constant wall temperature, introducing the hotter fluid passing through a constant wall heat flux in the driver. Although thermal conditions in CT are different between the

driver and the main channel, the thermal profile in the main channel differs very little and becomes asymptotic after passing the streamwise length of 10δ . In CTD, the main channel as well as the driver keeps two walls at different temperatures transporting heat from the top to bottom walls. CF and CAF are simulated only by the driver, where the fluid temperature difference from the wall, θ , is used as a computational variable to satisfy the streamwise periodicity. CF and CAF both solve resulted energy equation;

$$\frac{\partial \theta}{\partial t} + u_j \frac{\partial \theta}{\partial x_j} = \frac{\lambda}{\rho C_p} \frac{\partial^2 \theta}{\partial x_j \partial x_j} - \frac{\bar{q}_w}{\rho C_p u_m \delta} u, \quad (3.1)$$

where the last term means a source by the streamwise temperature gradient. The CF makes the instantaneous wall flux consistent with the source term in Eq. (3.1), whereas the CAF fixes the wall temperature fluctuation at zero⁽¹²⁾.

Table 3.1 Computational conditions.

	Case 1	Case 2	Case 3	Case 4
H/δ	0.4	0.2	0.2	0
$Re_{\tau 0}$	180	150	150	150
Pr	0.71	0.71	0.71	0.71
L_{x0}/δ	8	8	16	8
L_x/δ	26.6	24.7	19.6	48
L_w/δ	9	13	5	-
L_z/δ	3.2	3.2	12.8	3.2
N_{x0}	128	128	256	128
N_x	580	640	768	768
N_y	128	98	185	98
N_z	128	128	512	128
$\Delta x_0^{(+)}$	11.3	9.38	9.38	9.38
$\Delta x^{(+)}$	1.13-11.3	0.938-9.38	0.300-9.38	9.38
$\Delta y^{(+)}$	1.13-7.34	0.938-10.0	0.300-6.00	0.938-10.0
$\Delta z^{(+)}$	4.50	3.75	3.75	3.75
$\Delta t^{(+)}$	0.00720	0.0120	0.00600	0.0120
CT	-	Run	-	Run
CTD	Run	Run	Run	-

The computational conditions are listed in Table 3.1. Case 1 corresponds to the experiment by Yao et al.⁽⁴⁾, namely, equating the rib-height to the channel-half-width ratio to $H/\delta = 0.4$ and the frictional Reynolds number to $Re_{\tau 0} = 180$. Case 2 simulates $H/\delta = 0.2$ and $Re_{\tau 0} = 150$, adopting the number of grid cells of $(128+640) \times 98 \times 128$ and the spanwise channel length of $L_z/\delta = 3.2$. Case 3 treats the same condition as Case 2 using grids of $(256+768) \times 185 \times 512$ and the spanwise length of $L_z/\delta = 12.8$. Figure 3.2 exemplifies the grid arrangement for the main channel in Case 2. As shown in the figure, grid points are allocated finely close to the wall and rib surfaces to resolve

the thin boundary layer without numerical oscillation. Case 4 treats the main channel with no rib ($H/\delta = 0$) at $Re_{\tau 0} = 150$. As to thermal conditions, four numerical cases solve CT and/or CTD according to Table 3.1. In addition, the driver treats CF and CAF as earlier mentioned. Through the simulations, air flow is assumed and the Prandtl number is fixed at 0.71.

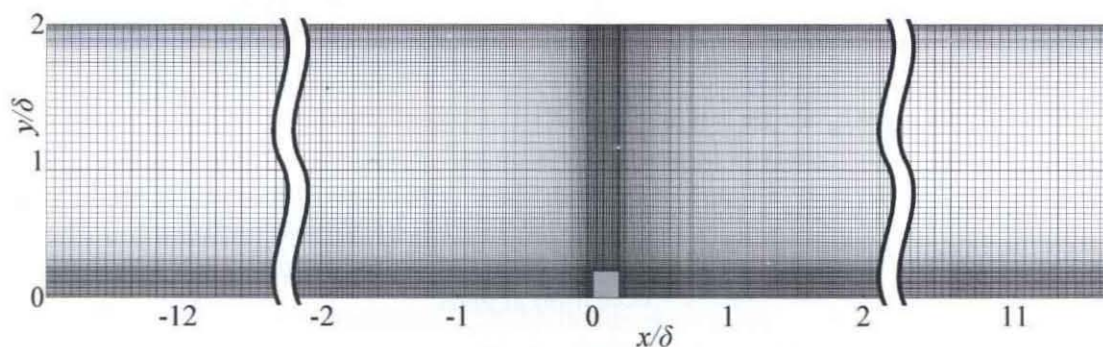


Fig. 3.2 Grid arrangement for Case 2.

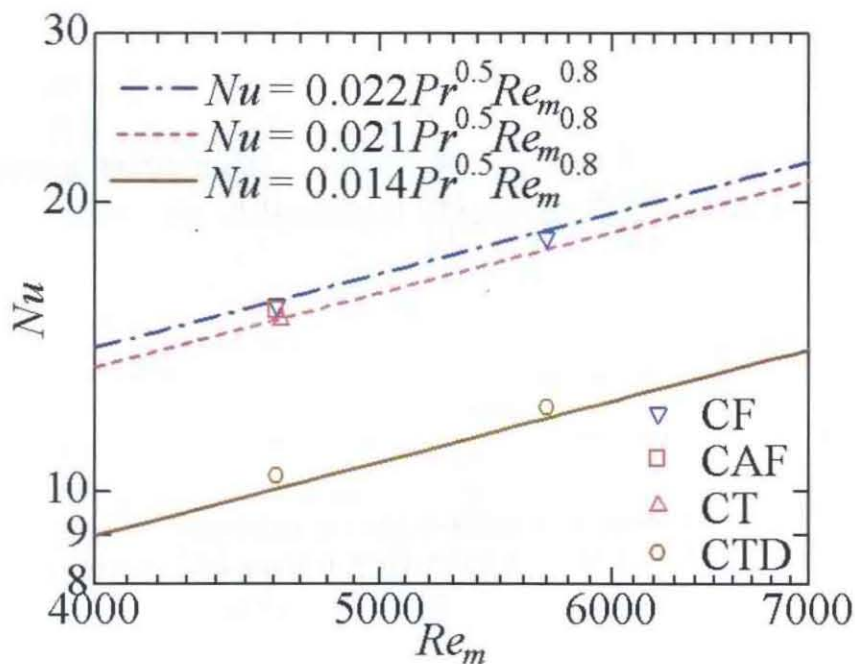


Fig. 3.3 Nusselt numbers for various thermal boundary conditions in smooth channel.

Figure 3.3 presents the Nusselt number for the smooth channel from four thermal conditions, where the Nusselt number is defined as follows:

$$Nu = \frac{2\bar{q}_w \delta}{\lambda(\bar{T}_w - T_m)} \quad (3.2)$$

In case of CT, the wall heat flux is averaged over the thermally asymptotic part in the main channel; the whole channel length excluding 10δ near the entrance. The results for CTD, CF and CAF are cited from the driver. The results for CT, CF and CAF

show almost no difference, whereas CTD reduces the Nusselt number by about 50 percent from other conditions. The figure includes lines from the past correlations:

$$Nu = 0.021 Pr^{0.5} Re_m^{0.8}, \quad \text{Kays et al.}^{(13)} \text{ for CT}; \quad (3.3)$$

$$Nu = 0.022 Pr^{0.5} Re_m^{0.8}, \quad \text{Kays et al.}^{(13)} \text{ for CF}; \quad (3.4)$$

and Eq. (2.8) for CTD. There is close agreement between the present simulation and the past correlations, validating the present simulation for cases of smooth channel.

3.3. Hydrodynamic Loss and Heat Transfer

The distributions of the local Nusselt number are shown in Fig. 3.4. In the figure, the global distribution on the ribbed surface and the distribution on rib surfaces are presented for CT (Constant Temperature Walls) and CTD (Constant Temperature Difference between Two Walls). The Nusselt numbers for two conditions take high values at the reattachment point on the ribbed wall ($x/\delta = 1.7$) and at the leading corner of the rib. There is no essential difference between Case 2 and Case 3, which change grids and the domain size, and independence from those is evidenced.

To measure the hydrodynamic loss, the present paper uses the friction factor defined as Eq. (2.4). This essentially means the dissipation of mechanical energy between x_u and x_d , in other words, the pumping power required to drive the fluid. It is noted that Eq. (2.4) reduces to the usual friction factor based on static pressure loss for the case of smooth walls. Figure 3.5 shows the friction factor of the ribbed channel for Case 2 with the reference positions of $x_u = -4\delta$ and $x_d = x$. The figure also shows the friction factor for the smooth wall (Case 4) together with the empirical correlations: Eqs. (2.6) and (2.7). In the figure the friction factor increases significantly in the ribbed channel, which reaches almost twice that of the smooth wall.

Figure 3.6 shows the spatial mean Nusselt number for the smooth and ribbed walls. The reference positions are again $x_u = -4\delta$ and $x_d = x$. In the figure, the Nusselt number is enhanced in the ribbed channel. However, increasing rate of the Nusselt number is only 30 percent, which is not so high as that of the wall friction.

In Fig. 3.7, the spatial mean Nusselt number is plotted against $f^{1/3} Re_m$ which corresponds to cubic root of non-dimensional pumping power. The figure shows the empirical relation between the Nusselt number and $f^{1/3} Re_m$ for the smooth wall:

$$Nu = 0.045 Pr^{0.5} \left(f^{1/3} Re_m \right)^{48/55}; \quad (3.5)$$

$$Nu = 0.0462 Pr^{0.5} \left(f^{1/3} Re_m \right)^{48/55}, \quad (3.6)$$

respectively deduced from Eqs. (2.6) and (3.3) and from Eqs. (2.7) and (3.3). The mean Nusselt number of the ribbed wall exceeds that of the smooth wall consuming the same pumping power when the integral limit is $x/\delta \geq 4$. In this form of presentation, the Nusselt number takes a maximum at $x/\delta = 6$, which is eight percent larger than the

smooth wall.

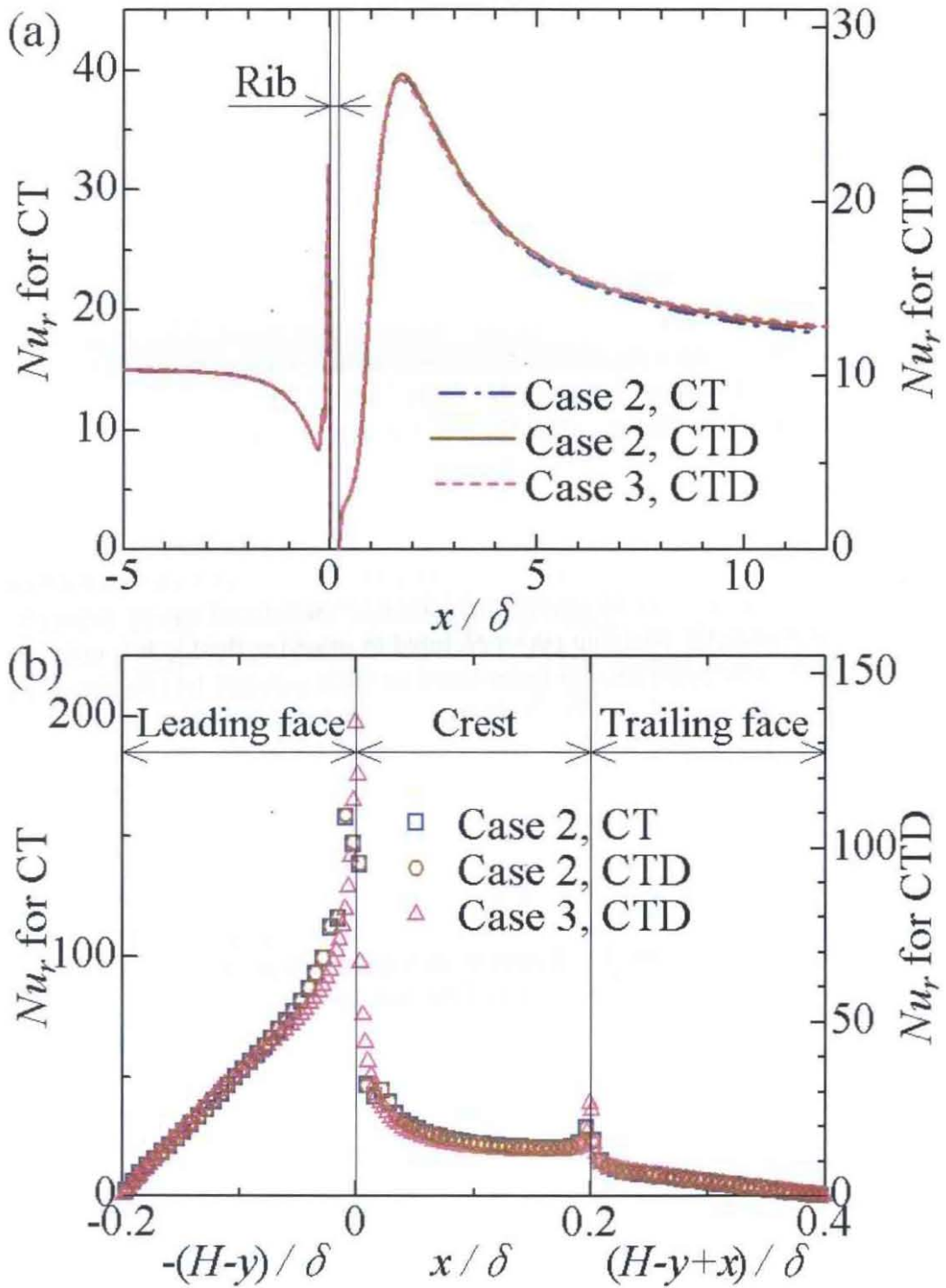


Fig. 3.4 Local Nusselt number. (a) Rough wall; (b) rib surface.

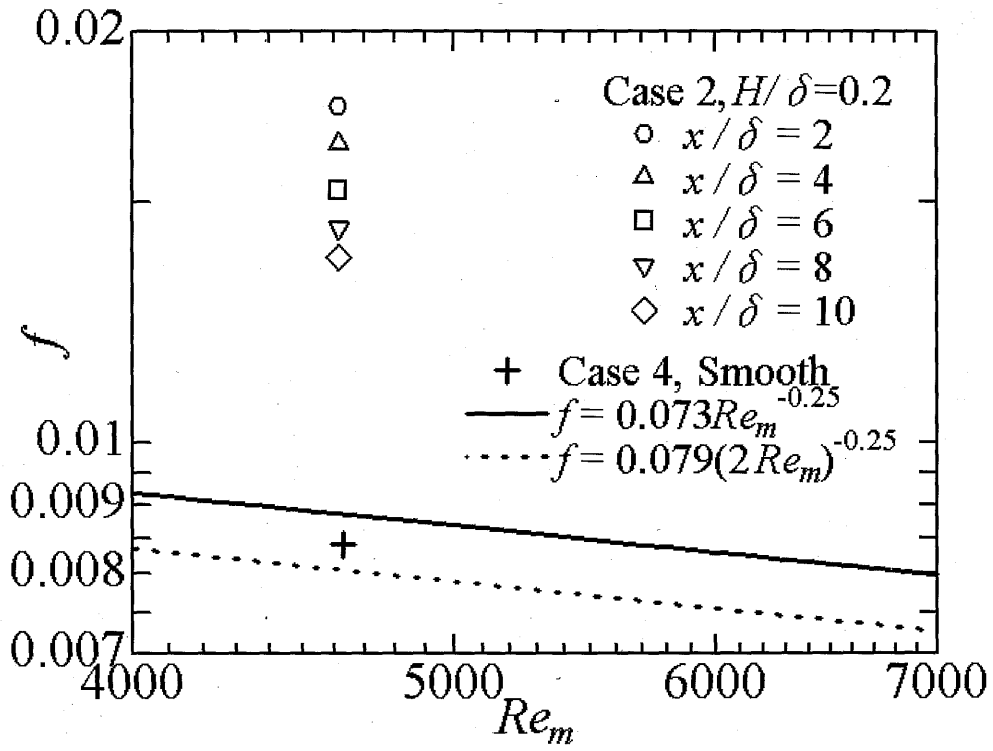


Fig. 3.5 Friction factor versus bulk Reynolds number.

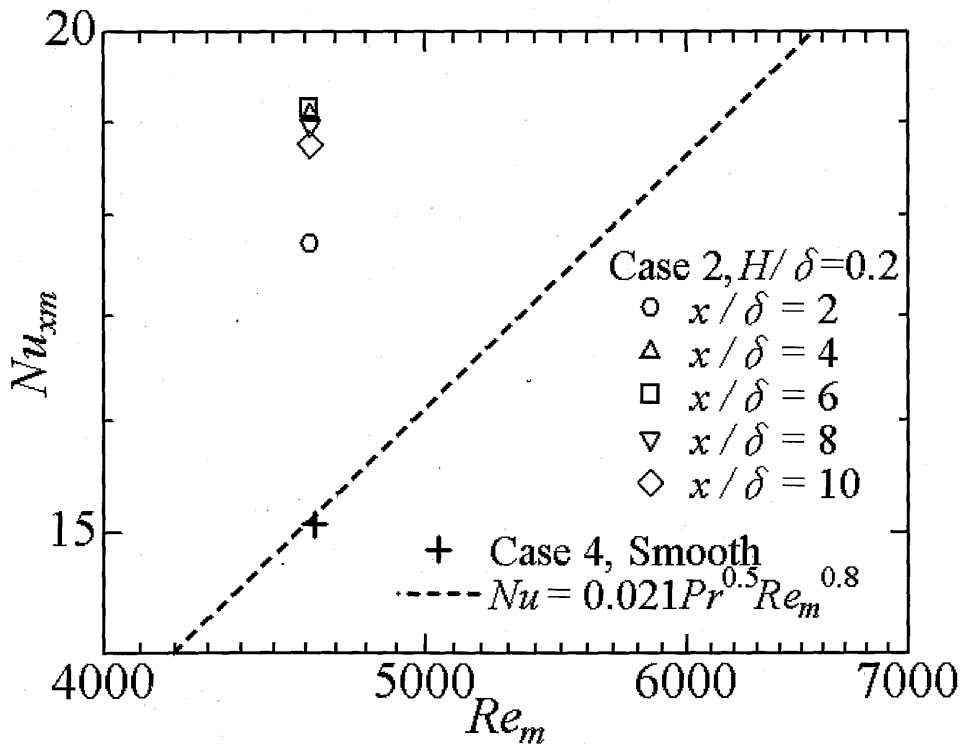


Fig. 3.6 Mean Nusselt number versus bulk Reynolds number.

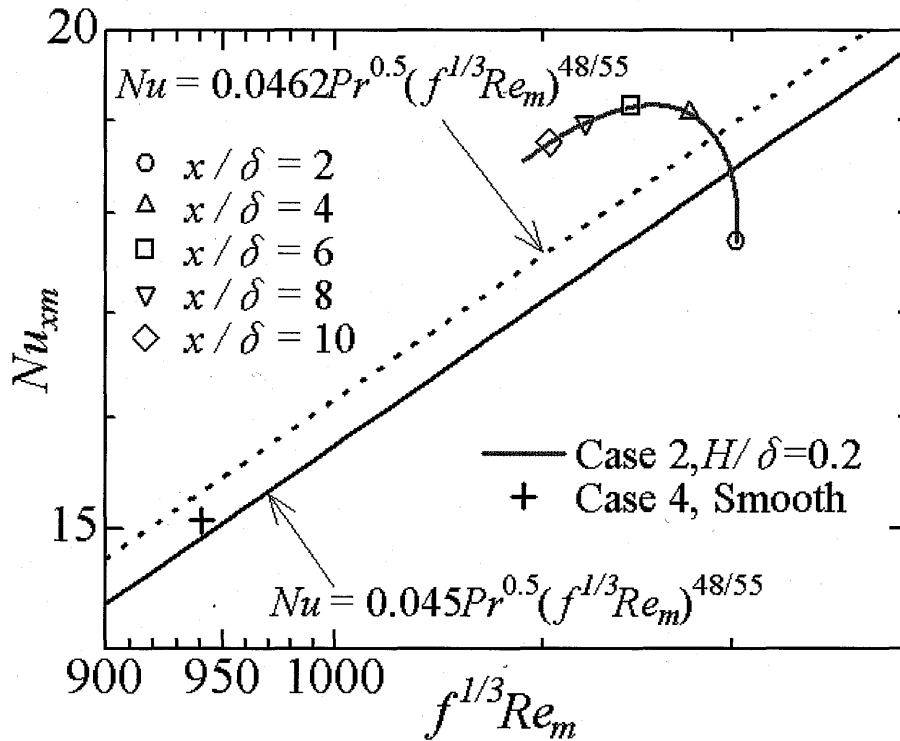


Fig. 3.7 Mean Nusselt number versus $f^{1/3} Re_m$.

3.4. Structure of Flow and Thermal Fields

Streamlines of mean flow are shown in Fig. 3.8, and contours of mean temperature in Fig. 3.9. These and following figures cite the numerical data from Case 2. Although the flow displacement by the rib relaxes swiftly behind the reattachment point, thermal excitation continues broadly as suggested by the dense temperature contours away from the rib

Figure 3.10 shows distribution of the wall variables: the friction coefficient and the Stanton number. High values of the Stanton number appear together with low friction coefficient near the reattachment point ($x/\delta = 1.7$). Such dissimilarity of heat and momentum transfer decays when going downstream, but remains to appear in the whole length computationally treated.

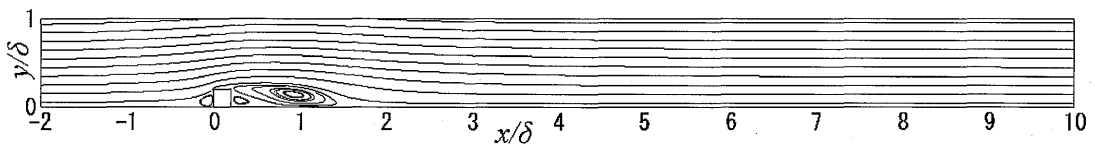


Fig. 3.8 Mean stream lines.

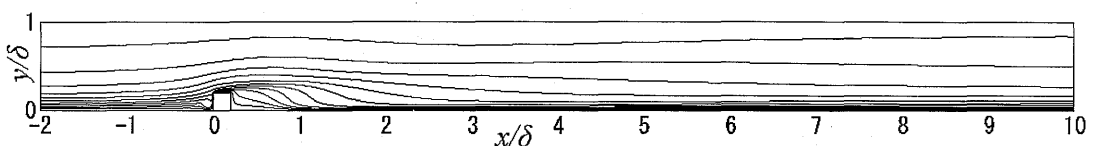


Fig. 3.9 Contour lines of mean temperature, $\bar{\theta} / \theta_m$. One contour level denotes 0.1.

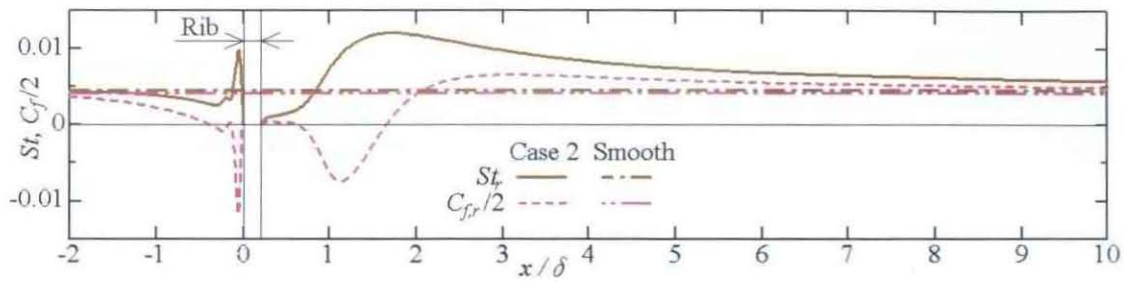


Fig. 3.10 Local skin friction coefficient and Stanton number on rough wall.

The iso-surface of negative pressure fluctuation is shown with contours of the friction coefficient fluctuation in Fig. 3.11(a) and of the Stanton number fluctuation in Fig. 3.11(b). The pressure iso-surfaces suggest that vortices are intermittently shed from the rib accompanying fluctuations of wall variables. Although the existing literatures depicted the two-dimensional structures behind a floated rod in the boundary layer⁽⁵⁾, the present DNS reveals that vortices are somewhat irregular and three-dimensional behind a protruded rib.

Figures 3.12 to 3.14 separately show quantities in Fig. 3.11. In Fig. 3.12, spanwise structures are twisted and skewed, and they are contaminated by longitudinal structures. However, the spanwise structures grow into organized vortices going away from the rib, and the Kelvin-Helmholtz type instability is suggested to occur. In Figs. 3.13 and 3.14, the wall values of friction and heat transfer shape longitudinal islands before and far behind the rib. Streaky structures of near-wall turbulence are thus thought to contaminate the spanwise roller structures (Fig. 3.12). Around spanwise roller structures marked at $x/\delta = 1.3, 2.7, 4.3, 5.8, 6.9$ (Fig. 3.12), the wall friction (Fig. 3.13) and heat transfer (Fig. 3.14) change differently, and the spanwise structures are implied to induce the transport dissimilarity.

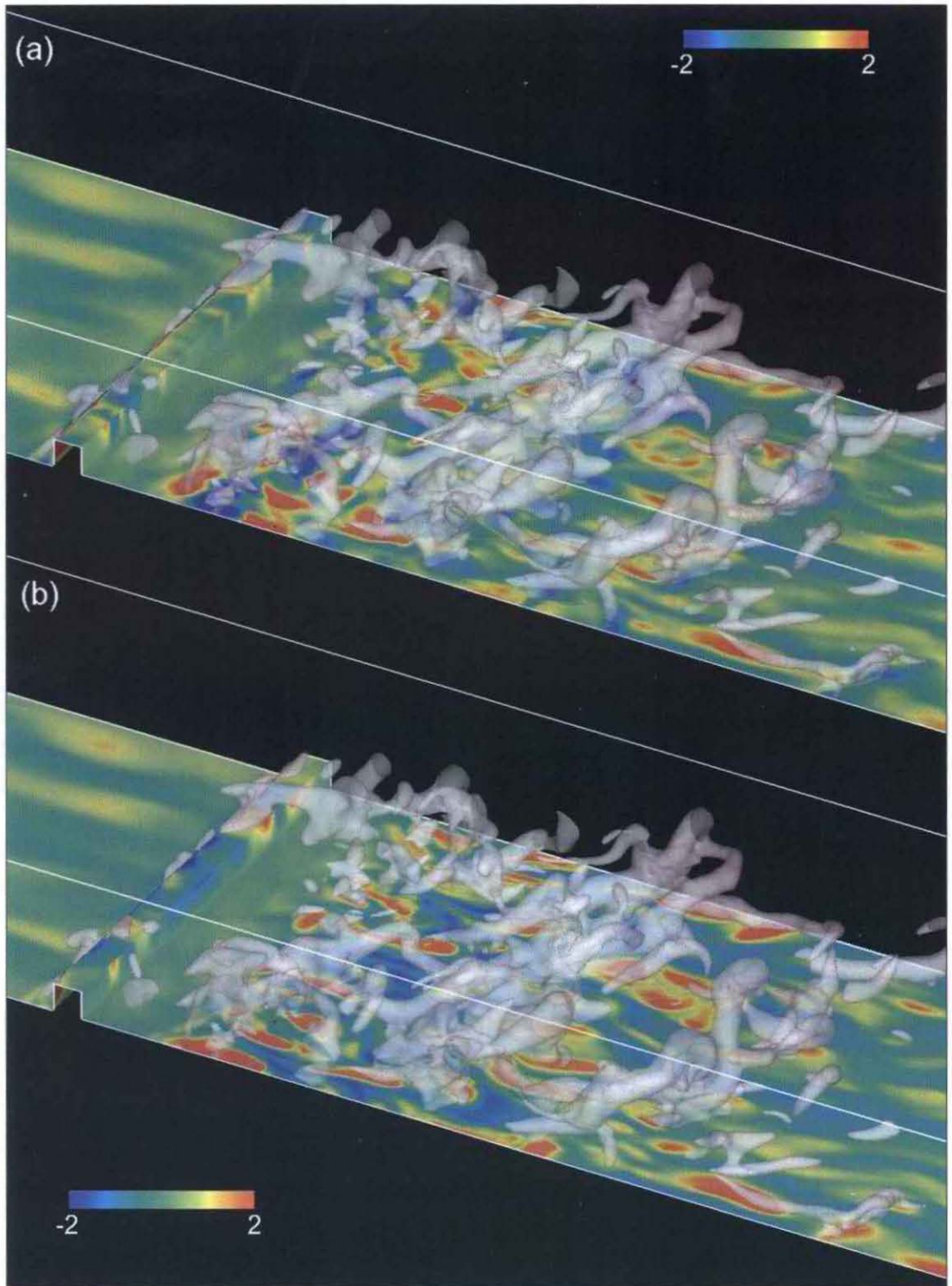


Fig. 3.11 Iso-surfaces of the negative pressure fluctuation, $p'/(\rho u_m^2) = -0.04$. (a) With contours of $C'_{f,r}/C_{f,SM}$, (b) with contours of St'_{r}/St_{SM} .

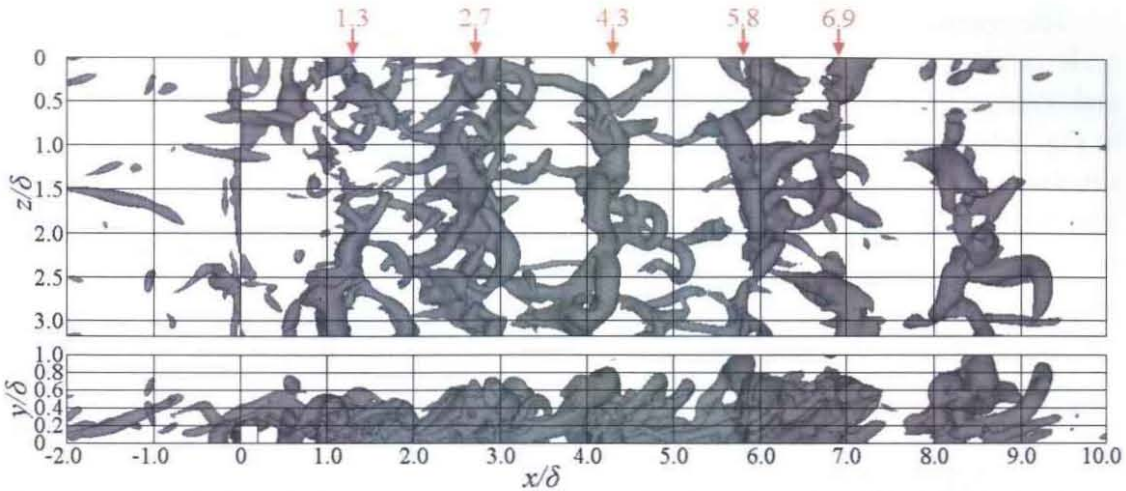


Fig. 3.12 Iso-surfaces of the negative pressure fluctuation, $p'/(\rho u_m^2) = -0.02$. Top: top view, bottom: side view.

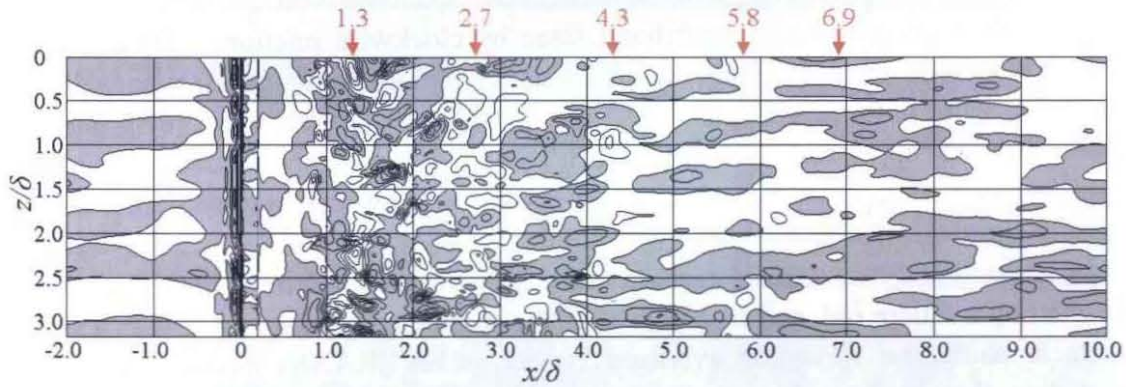


Fig. 3.13 Contour lines of $C'_{f,r}/C_{f,SM}$. Shaded areas represent positive. One contour level denotes 1.

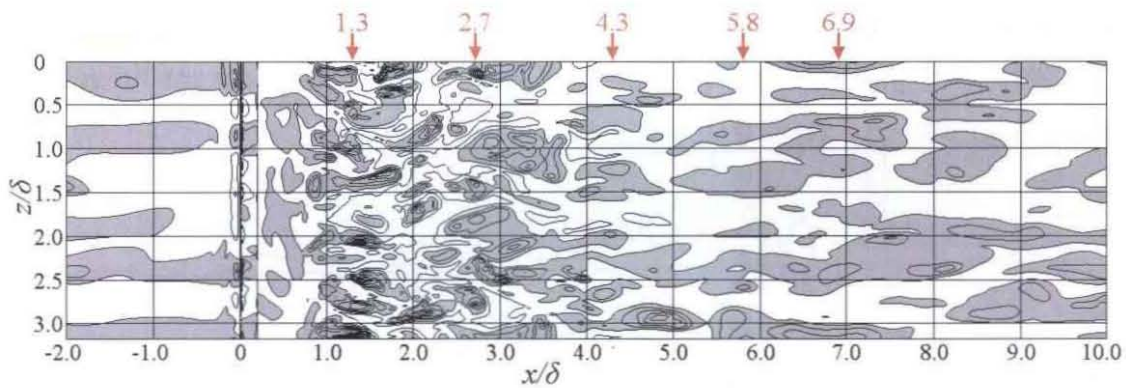


Fig. 3.14 Contour lines of St'_{r}/St_{SM} . Shaded areas represent positive. One contour level denotes 1.

The spanwise average of fluctuations is next examined to observe roles of large scale motion more clearly. Such statistical treatment is made for friction coefficient and Stanton number on the ribbed wall in Fig. 3.15, and for velocity fluctuation vectors in Fig. 3.16. In Fig. 3.15, decrease of wall friction and increase of heat transfer occur simultaneously, and the local dissimilarity is evident. In Figs. 3.15 and 3.16 local minima of wall friction are marked by arrows ($x/\delta = 1.3, 2.7, 4.3, 5.8, 6.9$), which correspond well to clockwise rotating vortices. In these figures, vortices with clockwise rotation accompany decrease of wall friction and increase of heat transfer, and such vortices are suggested to cause dissimilarity between momentum and heat transfer.

Figure 3.17 shows spanwise average of fluctuation of pressure, streamwise velocity, temperature and wall-normal velocity. This figure also shows $\langle u' \rangle \langle v' \rangle$ and $\langle v' \rangle \langle \theta' \rangle$, which respectively express the momentum flux by large-scale motion and the heat flux by that. Arrows in the figure indicate locations of local minima of wall friction. Comparison between Fig. 3.17 and Fig. 3.16 reveals flow and thermal fields around vortices summarized in Fig. 3.18. Namely, the spanwise vortices contain negative pressure fluctuation to resist centrifugal force by clockwise rotation. These vortices entrain hot fluid ($v' < 0, \theta' > 0$) at their downstream side to stagnate their near-wall layer ($u' < 0$). The vortices eject cold fluid ($v' > 0, \theta' < 0$) at their upstream side and accelerate their upper edge ($u' > 0$). Such two fluid motions both come to dissimilar transport ($u'v' > 0, v'\theta' < 0$), which suppress momentum transport and enhance heat transfer simultaneously.

K. Suzuki and H. Suzuki⁽¹⁴⁾ reported similar phenomenon in a laminar channel flow inserted by a square rod, and Inaoka et al.⁽⁵⁾ in a turbulent boundary layer with a similar obstacle using the Reynolds averaged Navier-Stokes (RANS) model. They both placed an obstacle away from the wall, where the Karman vortex streets are shed from the upper and lower sides of the obstacle. In their case, the lower streets of Karman vortices induced a counter rotating fluid near the wall to make the transport dissimilarity, and the Karman vortex contributed indirectly. Therefore, two-dimensional structures commonly cause the transport similarity both in the case of protrusion and the case of floated obstacle, but the detailed mechanisms are different.

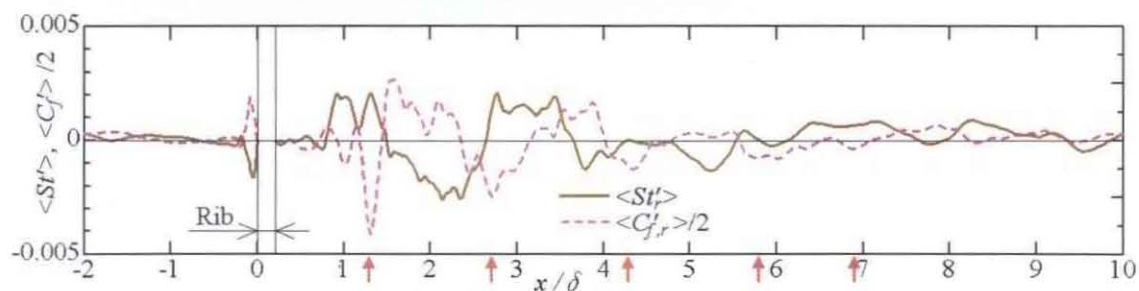


Fig. 3.15 Spanwise average values of $C_{f,r}'$ and St_r' .

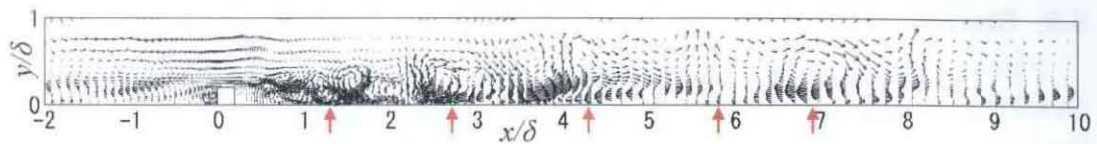


Fig. 3.16 Vectors of spanwise average velocity fluctuations.

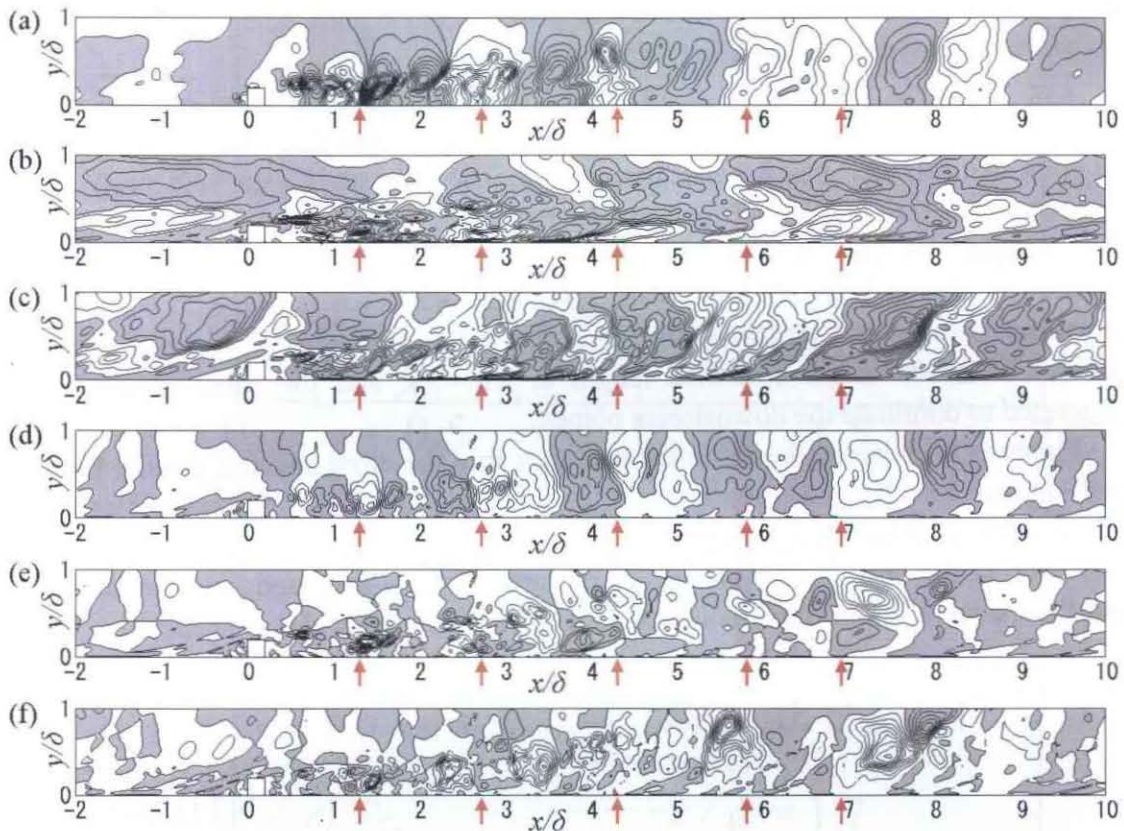


Fig. 3.17 Contour lines of spanwise average values. Shaded areas represent positive. (a) $\langle p' \rangle / (\rho u_m^2)$, one contour level denotes 0.005; (b) $\langle u \rangle / u_m$, one contour level denotes 0.02; (c) $\langle \theta \rangle / \theta_m$, one contour level denotes 0.02; (d) $\langle v \rangle / u_m$, one contour level denotes 0.02; (e) $\langle u' \rangle \langle v' \rangle / u_m^2$, one contour level denotes 0.001; (f) $\langle v' \rangle \langle \theta' \rangle / (u_m \theta_m)$, one contour level denotes 0.001.

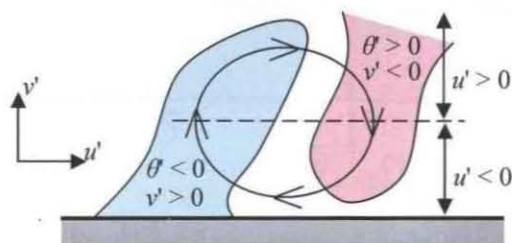


Fig. 3.18 Conceptual model of flow and thermal fields around spanwise vortex.

3.5. Statistical Analysis

Figure 3.19 shows cross-stream distributions of Reynolds shear stress, and Fig. 3.20 presents those of turbulent heat flux. The rib protrusion disturbs the flow to increase Reynolds stress at $x/\delta = 1.0, 1.7$, which turns to decline into smooth values behind the reattachment point ($x/\delta = 1.7$). Turbulent heat flux behaves similarly to the Reynolds shear stress, but its increase and decline delay to the shear stress. Turbulent heat flux is resulted to enhance more evidently at downstream planes, and its increasing rate surpasses the Reynolds shear stress at $x/\delta = 8$.

The Reynolds shear stress is expanded into the spanwise cross-spectral density between streamwise and wall-normal velocity components, E_{uvz} , in Fig. 3.21. In the smooth channel, E_{uvz} has a peak around $\lambda_z = 0.8\delta$ ($= 120\nu/U_{\tau 0}$ in wall unit), which corresponds to the interval between streaky structures⁽¹⁵⁾. The Reynolds shear stress is thus thought to majorly attribute to coherent motion in the smooth channel. The peak position is almost reserved even when turbulence enhances ($x/\delta = 1$ to 3), implying streaky structures still remain in the spanwise roller structures. However, the peak position shifts to larger spanwise length at $x/\delta = 8$, and the roller structures are suggested to dominate the downstream planes.

Figure 3.22 expands the turbulent heat flux into the cross spectral density between wall-normal velocity and temperature, $E_{v\theta z}$. The distribution of $E_{v\theta z}$ resembles E_{uvz} in the smooth channel, suggesting similarity between momentum and heat transport. However, at the downstream planes, $E_{v\theta z}$ is large in the wave band longer than E_{uvz} is, and the transport dissimilarity is indicated to appear in large-scale turbulence.

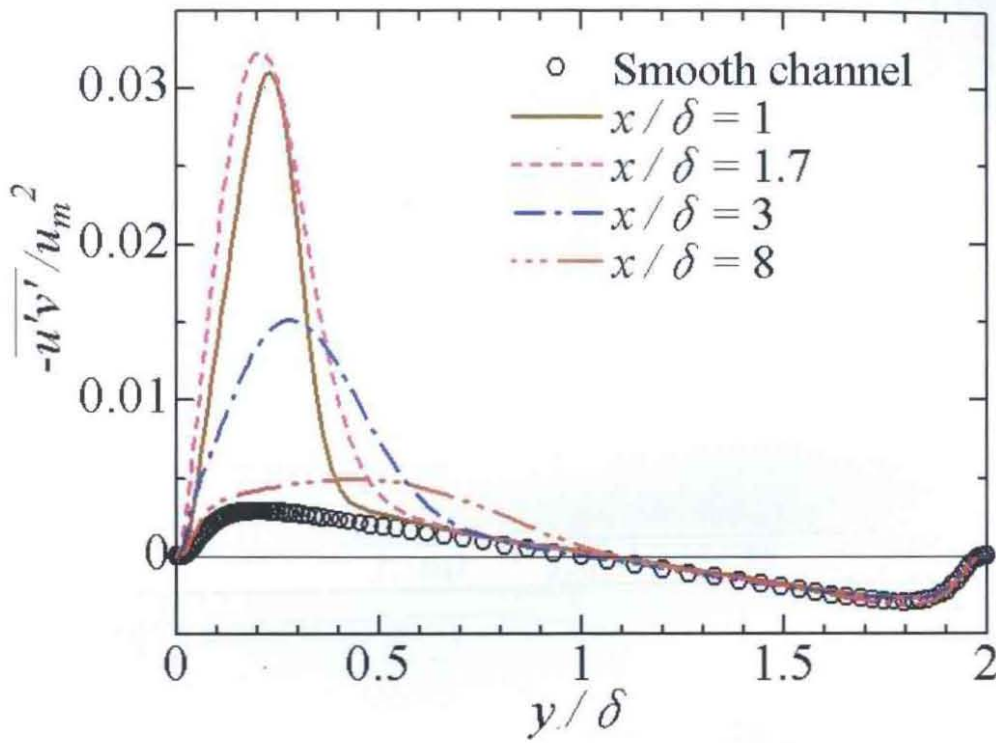


Fig. 3.19 Profiles of Reynolds shear stress.

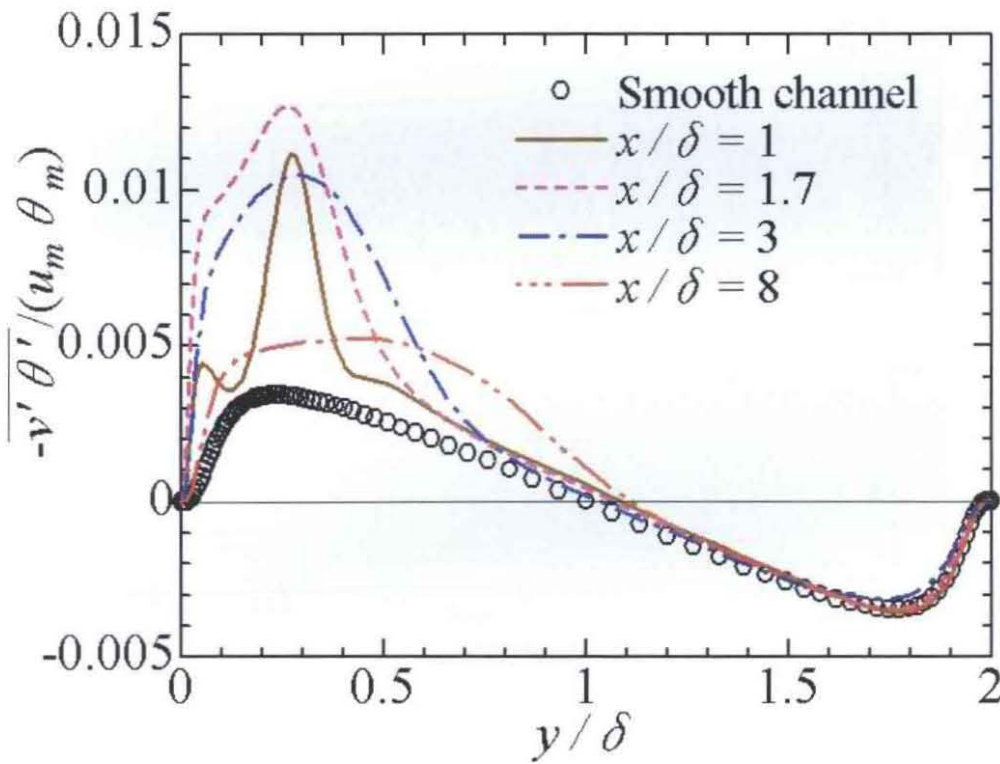


Fig. 3.20 Profiles of wall-normal turbulent heat flux.

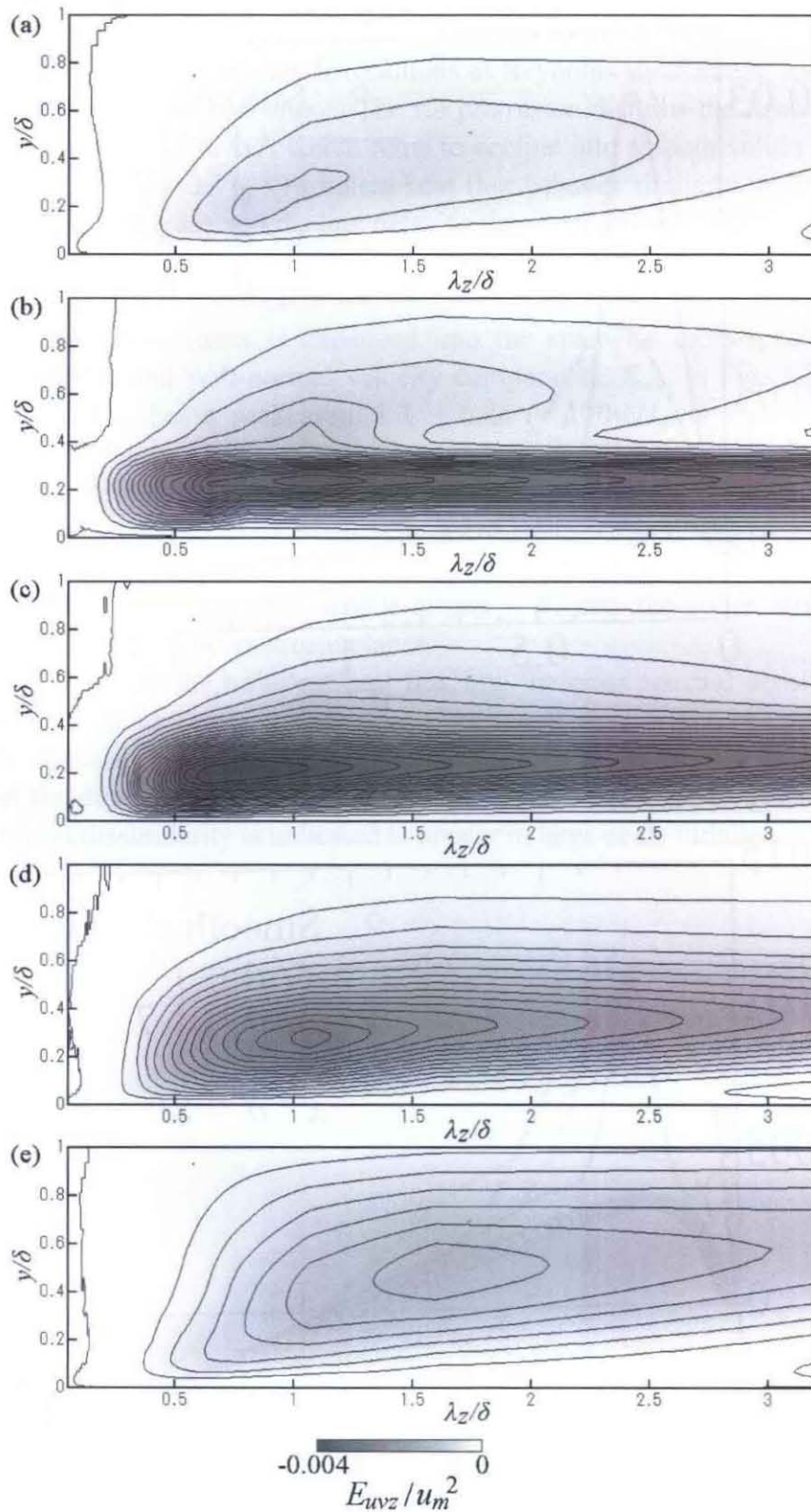


Fig. 3.21 Spanwise cross spectral density between streamwise and wall-normal velocities. One contour level denotes 0.0002. (a) Smooth channel; (b) at $x/\delta = 1$; (c) at $x/\delta = 1.7$; (d) at $x/\delta = 3$; (e) at $x/\delta = 8$.

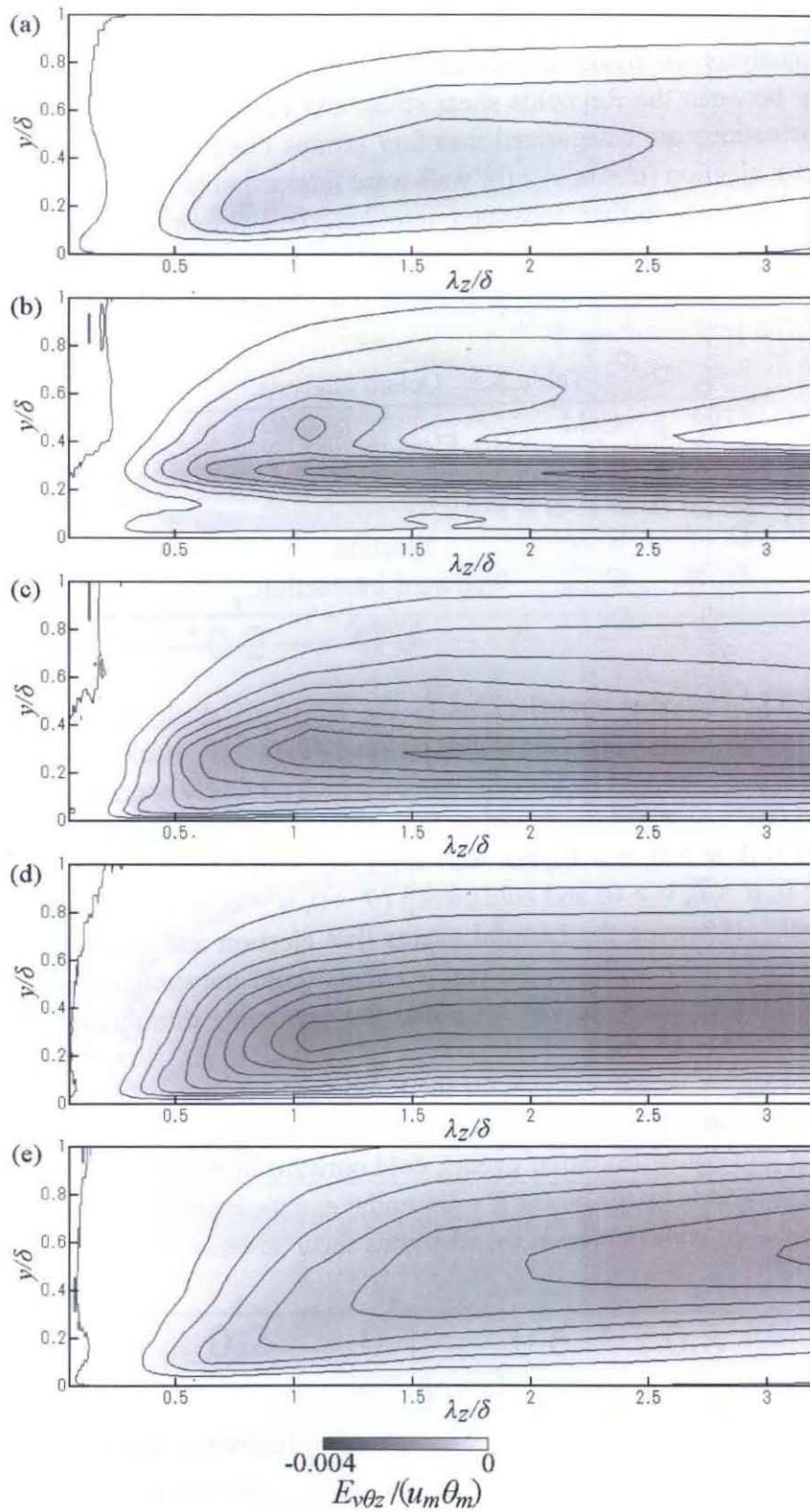


Fig. 3.22 Spanwise cross spectral density between wall-normal velocity and temperature. One contour level denotes 0.0002. (a) Smooth channel; (b) at $x/\delta = 1$; (c) at $x/\delta = 1.7$; (d) at $x/\delta = 3$; (e) at $x/\delta = 8$.

3.6. Octant Analysis

Octant analysis is made to reveal how the coherent motions contribute to dissimilarity between the Reynolds shear stress and turbulent heat flux quantitatively. Velocity fluctuations are categorized into four groups (Table 3.2): outward interaction ($u' > 0, v' > 0$); ejection ($u' < 0, v' > 0$); wall-ward interaction ($u' < 0, v' < 0$); sweep ($u' > 0, v' < 0$). Each is further separated into hot ($\theta' > 0$) or cold ($\theta' < 0$) events. Instantaneous values are sampled according to such grouping, and $\overline{u'v'}$ and $\overline{v'\theta'}$ are computed in each category, which represent the fractional contribution to the total flux.

Table 3.2 Octant analysis.

Hot $\theta' > 0$	Cold $\theta' < 0$	Fluid motion	u'	v'
S' ●	D ○	Outward-interaction	+	+
D' ▼	S ▽	Ejection	-	+
D ■	S' □	Wallward-interaction	-	-
S ▲	D' △	Sweep	+	-

In Fig. 3.23, fractional contributions to the Reynolds shear stress are compared between the smooth channel and the ribbed channel of $x/\delta = 8$. Cold ejection ($\theta' < 0, u' < 0, v' > 0$) and hot sweep ($\theta' > 0, u' > 0, v' < 0$), which similarly contribute the flow and heat transport ($u'v' < 0, v'\theta' < 0$), dominate both areas. Dissimilar events; cold outward interaction ($\theta' < 0, u' > 0, v' > 0$), hot wall-ward interaction ($\theta' > 0, u' < 0, v' < 0$), hot ejection ($\theta' > 0, u' < 0, v' > 0$) and cold sweep ($\theta' < 0, u' > 0, v' < 0$) are enlarged in the ribbed channel. However, the harmful events (hot ejection and cold sweep; $u'v' < 0, v'\theta' > 0$) mostly balance with the preferable events (cold outward interaction and hot wall-ward interaction; $u'v' > 0, v'\theta' < 0$), and the preferable dissimilarity does is not appealing in the ribbed channel.

Figure 3.24 shows octant analysis for the turbulent heat flux. Similar events; cold ejection and hot sweep are again dominant in the smooth channel and in the ribbed channel. The preferably dissimilar events; cold outward interaction and hot wall-ward interaction are balanced by the harmfully dissimilar events; hot ejection and cold sweep, which resemble their contribution to the Reynolds shear stress.

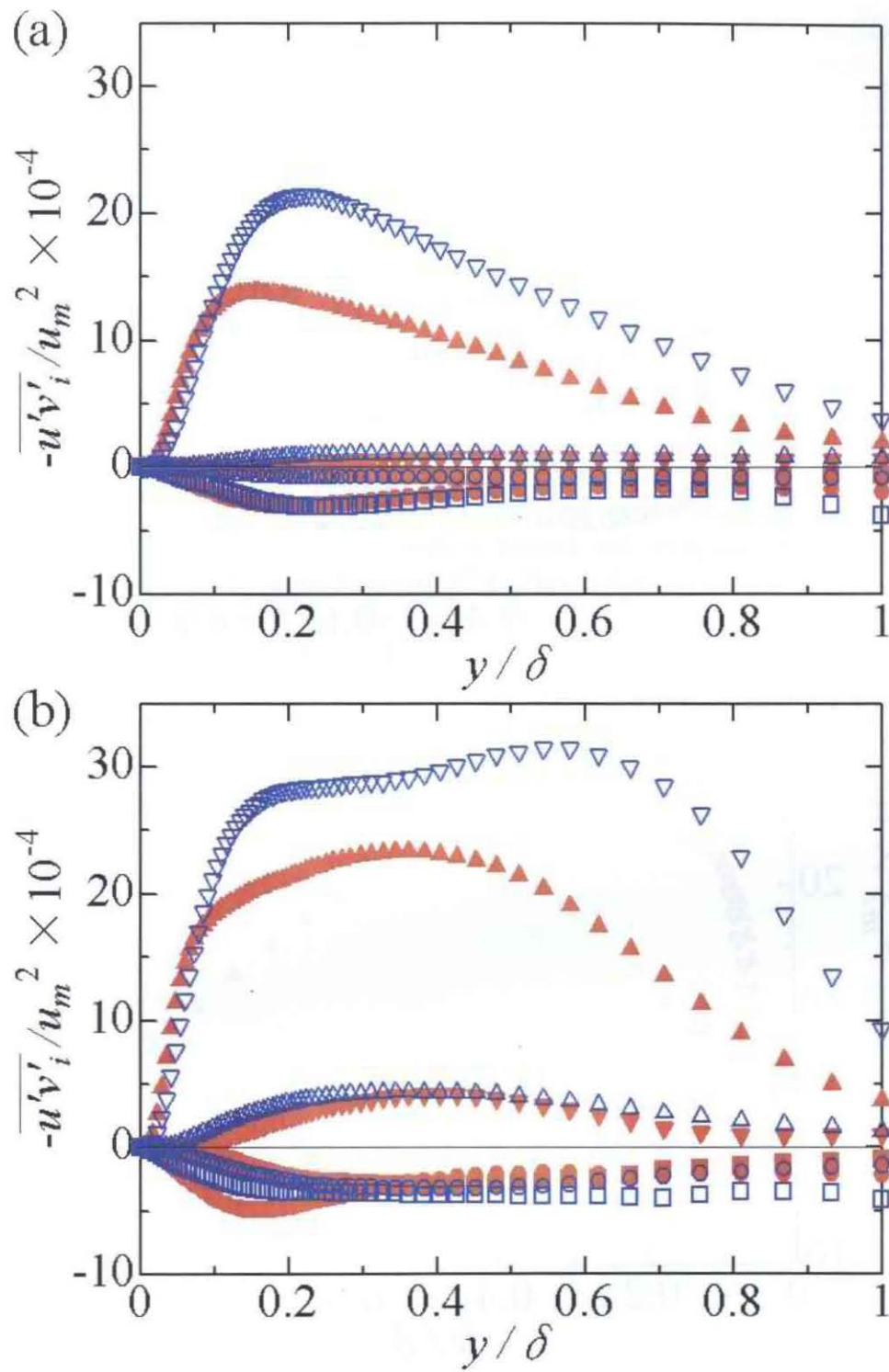


Fig. 3.23 Fractional contribution to Reynolds shear stress from each octant. (a) Smooth channel; (b) at $x/\delta = 8$.

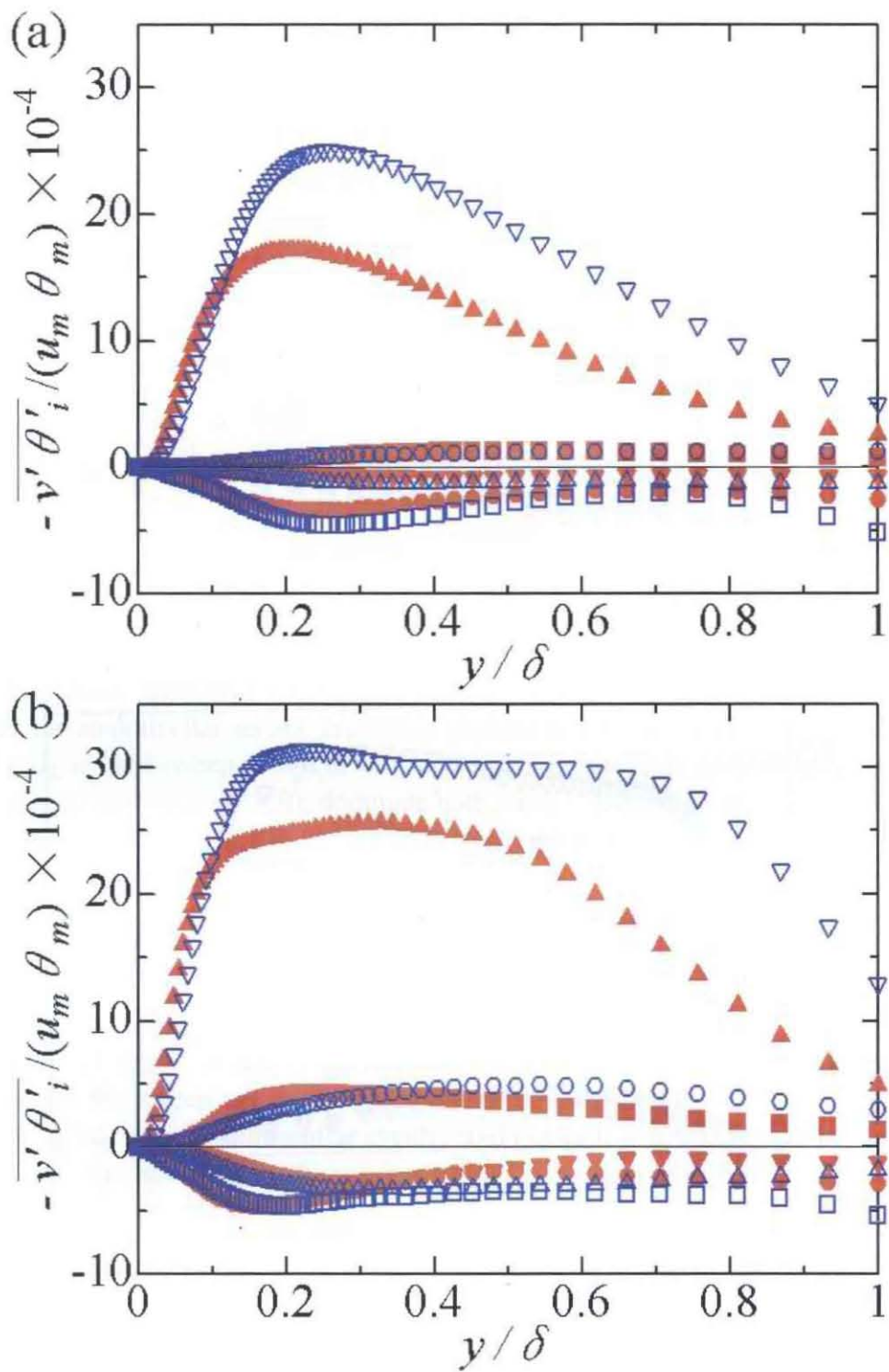


Fig. 3.24 Fractional contribution to wall-normal turbulent heat flux from each octant. (a) Smooth channel; (b) at $x/\delta = 8$.

Since the spanwise average of fluctuations captured large-scale coherent motions behind the rib as earlier mentioned, octant analysis for this average is thought to reveal contributions from the large-scale motion. Figures 3.25 and 3.26 show the analysis for $\overline{\langle u' \rangle \langle v' \rangle}$ and $\overline{\langle v' \rangle \langle \theta' \rangle}$, respectively, which represent the momentum and heat fluxes by the large scale motion. In the figures, the cold outward interaction ($\theta' < 0, u' > 0, v' > 0$) and hot wall-ward interaction ($\theta' > 0, u' < 0, v' < 0$) both act to suppress momentum transport and to enhance the heat transport, and they preferably contribute the transport dissimilarity more clearly than suggested by the analysis of total fluxes. The cold outward interaction and hot wall-ward interaction are consistent with coherent motion of large scale vortices: the ejection of cold fluid and the entrainment of hot fluid by the spanwise roller structures observed in Section 3.4. Therefore, the transport dissimilarity by the spanwise roller structures are quantitatively meaningful to make up to $\overline{\langle u' \rangle \langle v' \rangle}$ and $\overline{\langle v' \rangle \langle \theta' \rangle}$.

Although the present case exhibits the dissimilar events modestly away from the wall, the turbulent boundary layer with a floated rod indicated such events more prominently over the whole thickness of it⁽²⁾. This difference is thought to come from the geometric situation such that the floated obstacle enables to induce more powerful fluctuation near the wall than the protruded obstacle. However, the fractional contributions to the momentum and heat fluxes are analogous between the present case and the case with a floated obstacle, and inducing two-dimensional vortices to enhance the preferable interactions is recommended as a universal way to make the transport dissimilarity over the solid surface.

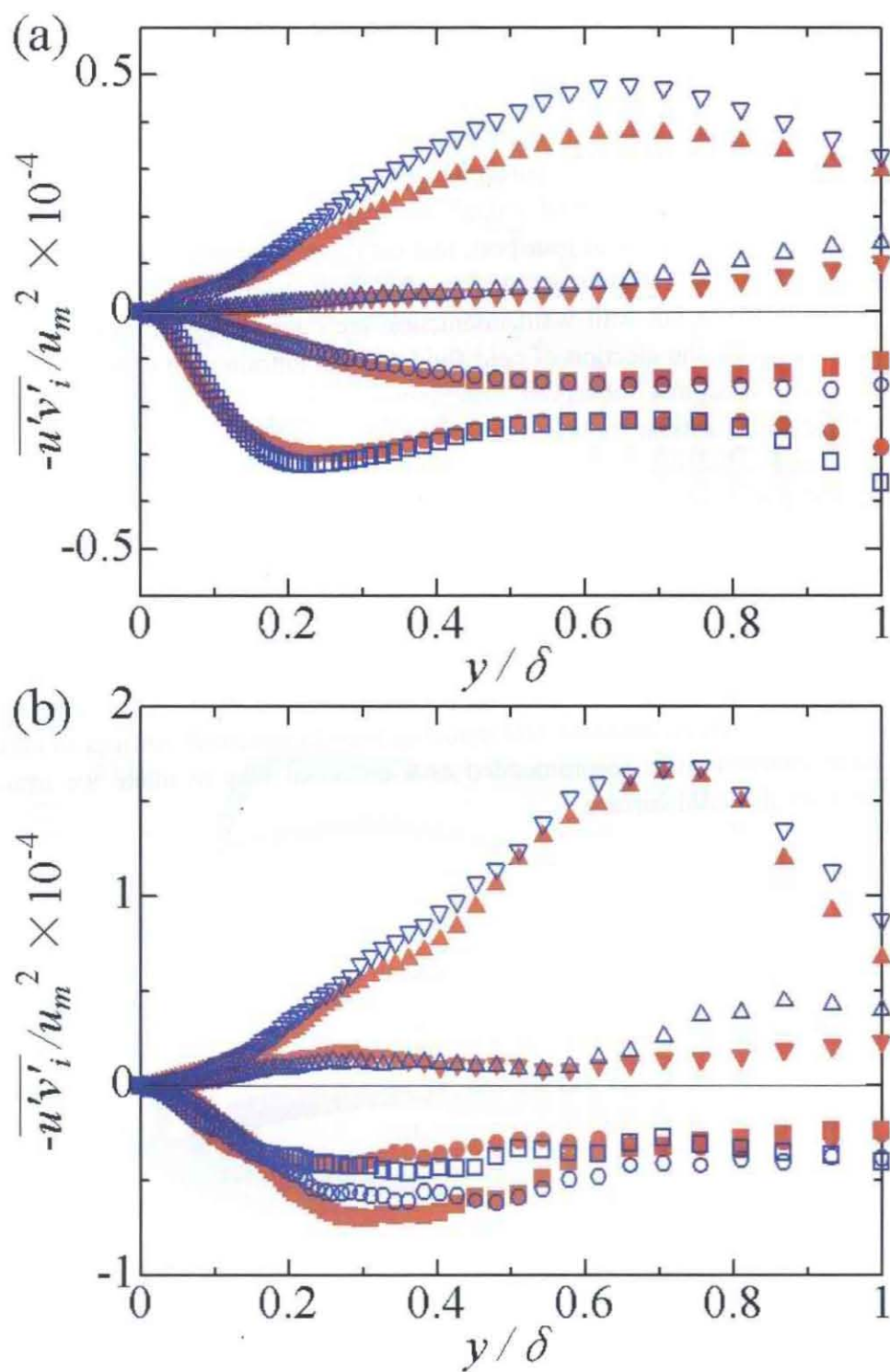


Fig. 3.25 Fractional contribution to Reynolds shear stress from each octant in the spanwise wave number, $k_z = 0$. (a) Smooth channel; (b) at $x/\delta = 8$.

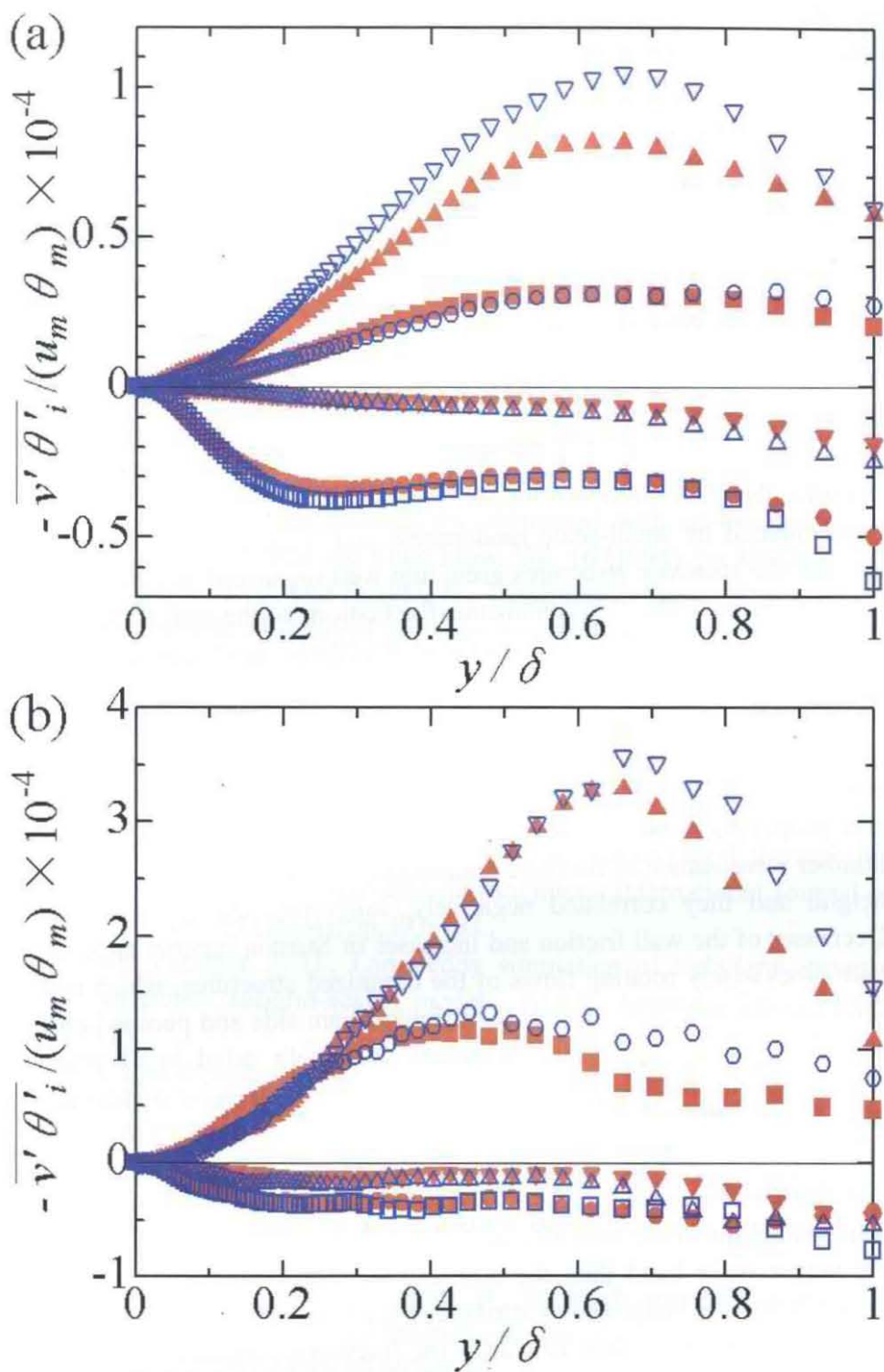


Fig. 3.26 Fractional contribution to wall-normal turbulent heat flux from each octant in the spanwise wave number, $k_z = 0$. (a) Smooth channel; (b) at $x/\delta = 8$.

3.7. Conclusions

This chapter described on large-scale coherent structures and the transport dissimilarity of the turbulent channel flow with a square rib protruded from the wall

surface. Basic equations were directly solved for the turbulent air flow at $Re_{\tau 0} = 150$. Two walls plus a rib were maintained at the same temperature, cooling the inflow with the fully developed profile between smooth walls. This study presented the numerical result of the rib height $H/\delta = 0.2$ including the instantaneous structures, and the cross spectrum density and octant analysis related to momentum and heat transport. Conclusions can be summarized as follows.

- Spatial mean Nusselt number was plotted against the pumping loss penalty changing the integral length. In this presentation, the spatial mean Nusselt number was maximized at the integral limit of 50 times the rib height, which exceeded the Nusselt number of the smooth channel consuming the same pumping power by eight percent. Therefore, a single rib protrusion could be efficient even when considering the hydrodynamic loss.
- The negative pressure iso-surfaces captured the spanwise roller structures almost periodically shed from the square protrusion. The spanwise structures were contaminated by small-scale randomness and longitudinal vortices close to the rib, but the spanwise structures grew into well organized motion when travelling into the downstream. Instantaneous fluctuations of the wall friction and Stanton number, accompanied by the spanwise structures, have staggered distributions, which suggested the local dissimilarity between momentum and heat transport.
- The spanwise averages of numerical quantities were examined to reveal roles of the large-scale organized motion. This statistical treatment was made for fluctuations of the wall friction and Stanton number, and for pressure, velocity and temperature fluctuations. By this treatment, the wall friction and Stanton number were shown to oscillate sinusoidally in the length up to 50 times the rib height, and they correlated negatively, suggesting the transport dissimilarity. Decreases of the wall friction and increases of Stanton number appeared together with clockwise rotating flows of the organized structures, which entrained hot fluid into the near wall layer at their downstream side and pumped out cold fluid at their upstream side. Such fluid motions both acted to decrease the wall friction and to increase the heat transfer, and the spanwise organized structures were thought to be a key element to induce the transport dissimilarity.
- The Reynolds shear stress and the wall-normal turbulent heat flux were expanded into the cross spectral density. The spectral distributions of the two quantities were analogous in the smooth channel, but the heat transport occurred strongly in the longer wave band than the momentum transport. Therefore, the transport dissimilarity was suggested to attribute to the large-scale motion.
- Octant analysis was made to clarify the fractional contribution to the Reynolds shear stress and the wall-normal turbulent heat flux. This analysis was made for the fluctuations of velocity and temperature, and also for their spanwise averages. In the analysis for the spanwise averages, the preferably dissimilar events; the cold outward interaction and the hot wallward interaction were as large as other major events; the hot sweep and the cold ejection in the near wall region of $y/\delta < 0.2$. These two preferable events were consistent with the large-scale fluid motions by the spanwise roller structures causing the transport dissimilarity, and

the large-scale motion was thought to be meaningful to contribute to the transport dissimilarity.

3.8. References

- (1) Lewis, M. J., Optimising the thermohydraulic performance of rough surfaces, *International Journal of Heat and Mass Transfer*, Vol. 18 (1975), pp.1243-1248.
- (2) Suzuki, H., Suzuki, K. and Sato, T., Dissimilarity between heat and momentum transfer in a turbulent boundary layer disturbed by a cylinder, *International Journal of Heat and Mass Transfer*, Vol. 31 (1988), pp.259-265.
- (3) Yao, M., Nakatani, M., Okuda, M. and Suzuki, K., Simultaneous measurements of flow and thermal fields in a turbulent channel flow with insertion of a square rod, *Transactions of the JSME Series B*, Vol. 60 (1994), pp.4192-4199.
- (4) Yao, M., Nakatani, M. and Suzuki, K., Flow visualization and heat transfer experiments in a turbulent channel flow obstructed with an inserted square rod, *International Journal of Heat and Fluid Flow*, Vol. 16 (1995), pp.389-397.
- (5) Inaoka, K., Yamamoto, J. and Suzuki, K., Dissimilarity between heat transfer and momentum transfer in a disturbed turbulent boundary layer with insertion of a rod - modeling and numerical simulation, *International Journal of Heat and Fluid Flow*, Vol. 20 (1999), pp.290-301.
- (6) Miyake, Y., Tsujimoto, K. and Nakaji, M., Direct numerical simulation of rough-wall heat transfer in a turbulent channel flow, *International Journal of Heat and Fluid Flow*, Vol. 22 (2001), pp.237-244.
- (7) Nagano, Y., Hattori, H. and Houra, T., DNS of velocity and thermal fields in turbulent channel flow with transverse-rib roughness, *International Journal of Heat and Fluid Flow*, Vol. 25 (2004), pp.393-403.
- (8) Yang, K. and Ferziger, J. H., Large-eddy simulation of turbulent obstacle flow using a dynamic subgrid-scale model, *AIAA Journal*, Vol. 31 (1993), pp.1406-1413.
- (9) Orellano, A. and Wengle, H., Numerical simulation (DNS and LES) of manipulated turbulent boundary layer flow over a surface-mounted fence, *European Journal of Mechanics, B/Fluids*, Vol. 19 (2000), pp.765-788.
- (10) Yakhot, A., Liu, H. and Nikitin, N., Turbulent flow around a wall-mounted cube: A direct numerical simulation, *International Journal of Heat and Fluid Flow*, Vol. 27 (2006), pp.994-1009.
- (11) Makino, S., Iwamoto, K. and Kawamura, H., Turbulent structures and statistics in turbulent channel flow with two-dimensional slits, *International Journal of Heat and Fluid Flow*, Vol. 29 (2008), pp.602-611.
- (12) Kasagi, N., Tomita, Y. and Kuroda, A., Direct numerical simulation of passive scalar field in a turbulent channel flow, *Transactions of the ASME, Journal of Heat Transfer*, Vol. 114 (1992), pp.598-606.
- (13) Kays, W. M., Crawford, M. E. and Weigand, B., *Convective Heat and Mass Transfer*, fourth ed. (2005), McGraw-Hill, New York.

- (14) Suzuki, K. and Suzuki, H., Instantaneous structure and statistical feature of unsteady flow in a channel obstructed by a square rod, *International Journal of Heat and Fluid Flow*, Vol. 15 (1994), pp.426-437.
- (15) Kim, J., Moin, P. and Moser, R., Turbulence statistics in fully developed channel flow at low Reynolds number, *Journal of Fluid Mechanics*, Vol. 177 (1986), pp.133-166.

Chapter 4 Channel Flow with Ribs

4.1. Introduction

There are compiled information on fully developed periodic flow and heat transfer in the ribbed channel⁽¹⁾⁻⁽⁸⁾. For example, Lewis⁽¹⁾ examined heat transfer enhancement taking the hydraulic loss into account. According to this reference, the heat transfer enhancement occurred most efficiently when the roughness Reynolds number, $U_r H/\nu$, was 20 and the space between ribs corresponds to the total length of separation bubbles before and behind each rib. Recently, DNSs (Direct Numerical Simulations) revealed transport mechanisms through analyzing the Reynolds stress budgets and instantaneous structures in the case of periodic ribs⁽⁵⁾⁻⁽⁸⁾.

However, there are limited numbers of publications for the developing cases^{(9), (10)}. Liou and Hwang⁽⁹⁾ made experiments on the required length for the flow establishment. Due to the scarceness of related papers, ambiguity has been left in optimization of the initial arrangement of ribs.

In this chapter, DNSs are performed for developing air flows in a channel with several ribs mounted on the wall. At the channel inlet, fully developed turbulent channel flow is provided by an additional simulator. Keeping the rib height at $H/\delta = 0.2$, several rib pitches are investigated. For analogous situations, fully developed cases are simulated by assuming the streamwise periodicity. Investigation is made for characteristics of flow and heat transfer in the initial region of the channel through comparison with developed cases. Mechanisms of heat transport are argued through presentation of streamlines, thermal contours and turbulence statistics including a turbulent heat flux. Instantaneous flow structures are examined to obtain visualized images of vortices triggering heat transfer enhancement.

4.2. Numerical Methods for Developing Region

We computed both developing and fully developed flows in ribbed channels. Numerical methods for the developing region are mentioned in this section.

Figure 4.1(a) shows the computational domain and the coordinate system. The square ribs are placed on one wall of the channel with constant pitch for each computed case. The numerical methods for the flow and thermal fields are also same as Chapter 2:

- The inflow is provided by driver part.
- The temperature difference, ΔT_w , is given to the bottom wall against the top wall with isothermal walls.
- The rib surfaces are maintained at the same temperature as the bottom wall.

Table 4.1 shows the numerical condition and the grid resolution. The rib height, H , is kept constant at $H/\delta = 0.2$. The rib pitch, P_i , is changed at four steps; $P_i/H = 2, 4, 7$ and 8. The rib number, N_{rib} , for each case is selected so that the ribbed length, $(P_i/H)N_{rib}$, exceeds 35. The friction Reynolds number at the inlet, $Re_{\tau 0}$, is assigned at 150. The corresponding bulk Reynolds number, Re_m , is approximately 4560. Air

flow is assumed, and the Prandtl number is given 0.71. The grid data in the streamwise direction are as Table 4.1. The grids in the wall-normal and spanwise directions are the same in all the cases: $N_y = 98$, $N_z = 64$, $\Delta y/\delta = 0.00625-0.0667$ and $\Delta z/\delta = 0.05$. The computational grids are allocated finely near the walls and in the ribbed channel, especially dense in upstream of the front surface of the rib. Single-rib simulations using this kind of resolution agreed well with an experiment and with a fine-grid simulation, and the numerical code and the grids were validated (see Chapter 2).

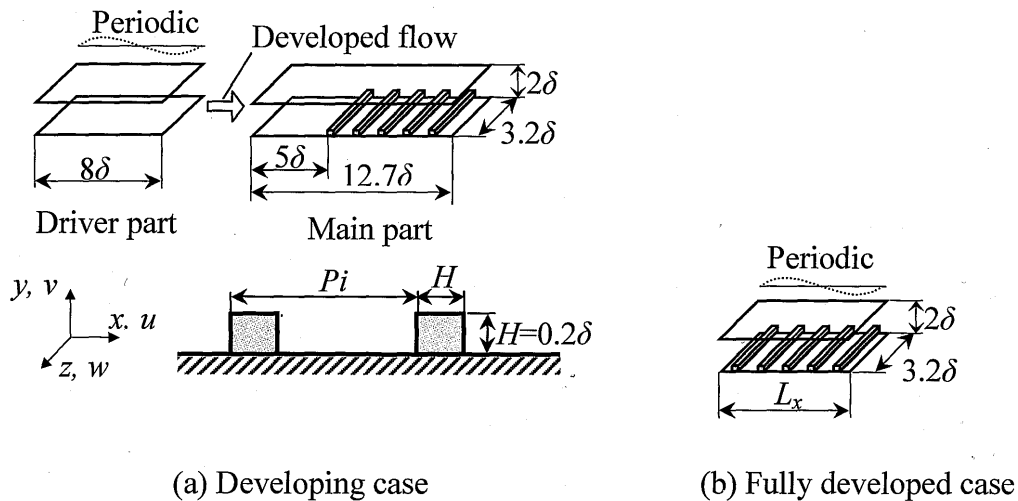


Fig. 4.1 Computational domain and coordinate system.

Table 4.1 Computational conditions for developing cases.

	Case 1	Case 2	Case 3	Case 4
Pi/H	2	4	7	8
N_{rib}	19	10	6	5
$Re_{\tau 0}$	150	150	150	150
Pr	0.71	0.71	0.71	0.71
N_{x0}	64	64	64	64
N_x	768	768	768	768
N_y	98	98	98	98
N_z	64	64	64	64
$\Delta x_0/\delta$	0.125	0.125	0.125	0.125
$\Delta x/\delta$	0.00625-0.0625	0.00625-0.0625	0.00625-0.0625	0.00625-0.0625
$\Delta y/\delta$	0.00625-0.0667	0.00625-0.0667	0.00625-0.0667	0.00625-0.0667
$\Delta z/\delta$	0.05	0.05	0.05	0.05

4.3. Numerical Methods for Fully Developed Region

Fully developed flows are simulated in the same way as the developing cases, except that streamwise periodicity is assumed without the driver part (Fig. 4.1(b)). The computational conditions are listed in Table 4.2. Four cases treat the same rib geometry as the developing cases, and three cases are added. The grid resolutions of

Case F-3f are finer than those of Case F-3. The mean friction Reynolds number, Re_τ , is selected for $Re_m \approx 4560$ in each case.

Table 4.2 Computational conditions for fully developed cases.

	Case F-1	Case F-2	Case F-3	Case F-4
Pi/H	2	4	7	8
N_{rib}	16	8	5	4
Re_τ	185	240	300	300
Pr	0.71	0.71	0.71	0.71
L_x	6.4	6.4	7.0	6.4
N_x	512	512	560	512
N_y	98	98	98	98
N_z	64	64	64	64
$\Delta x/\delta$	0.0125	0.0125	0.0125	0.0125
$\Delta y/\delta$	0.00625-0.0667	0.00625-0.0667	0.00625-0.0667	0.00625-0.0667
$\Delta z/\delta$	0.05	0.05	0.05	0.05
	Case F-5	Case F-6	Case F-7	Case F-3f
Pi/H	9	10	16	7
N_{rib}	4	4	2	5
Re_τ	300	300	275	300
Pr	0.71	0.71	0.71	0.71
L_x	7.2	8.0	6.4	7.0
N_x	576	640	512	1120
N_y	98	98	98	270
N_z	64	64	64	128
$\Delta x/\delta$	0.0125	0.0125	0.0125	0.00625
$\Delta y/\delta$	0.00625-0.0667	0.00625-0.0667	0.00625-0.0667	0.002-0.02
$\Delta z/\delta$	0.05	0.05	0.05	0.025

4.4. Comparison with Experimental Data

Since turbulent flow data for roughness have substance in the fully developed region, validity of the computation is checked for the region. Profiles of the rough-wall mean velocity normalized by the rough-wall friction velocity are shown in Figure 4.2. The present result, the experimental data by Hanjalić and Launder⁽²⁾ and the DNS result by Ikeda and Durbin⁽⁷⁾ have the same rib pitch, i.e., $Pi/H = 10$. The logarithmic function have been used by Hanjalić and Launder,

$$\frac{\langle \bar{u}_r \rangle}{\langle U_{\tau,r} \rangle} = \frac{1}{0.42} \ln\left(\frac{y}{H}\right) + 3.2, \quad (4.1)$$

is also shown in the figure. Although the Reynolds number of the present case is lower than a tenth of that for the experiment, the mean velocity profiles agree well above $y/H \approx 2$. In addition, the present distribution agrees well with the DNS result by

Ikeda and Durbin.

Profiles of the rough-wall heat transfer coefficient normalized by its average-value are shown in Figure 4.3. The experimental data by Williams and Watts⁽³⁾ and by Kattchee and Mackewicz⁽⁴⁾ have been obtained using a mass transfer analogy technique. The present data generally agree with the measurements, especially between D and E. The numerical and experimental values have noteworthy differences near B, and this is probably caused by that the experimental measurements at the corner was particularly difficult. Figure 4.3 also shows the result of Case F-3f which has fine grid resolutions, and this result agrees to that of Case F-3. Hence, validity of the present DNS is confirmed.

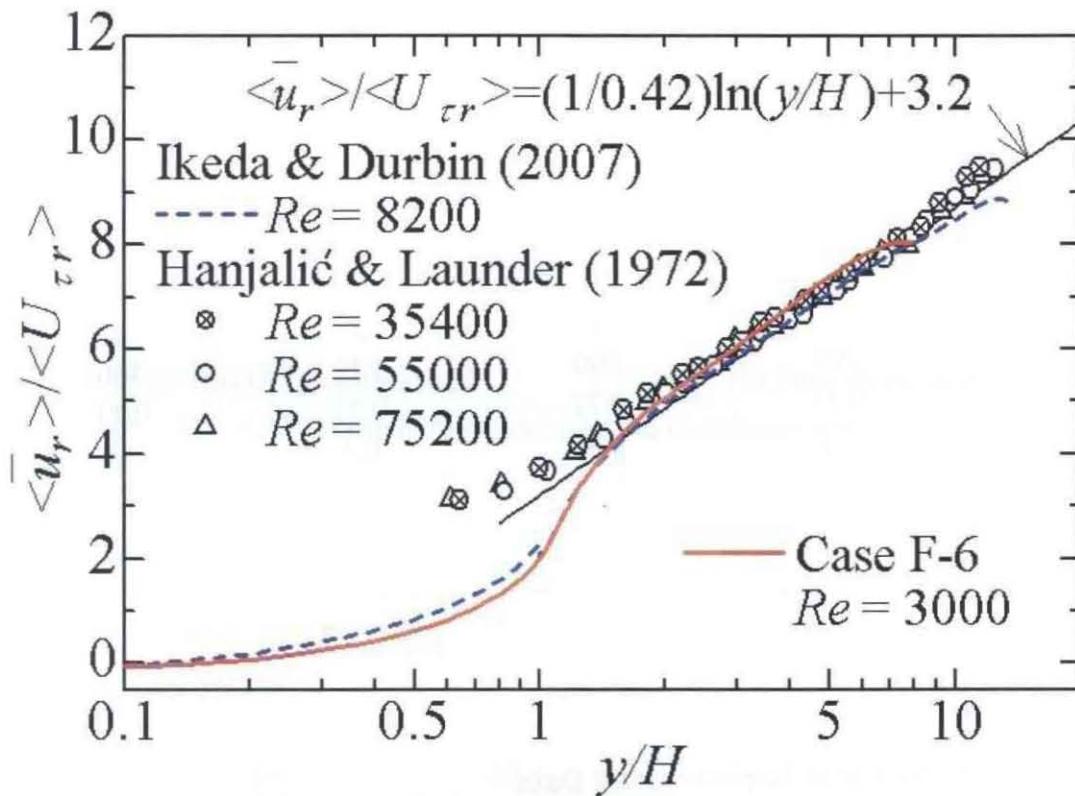


Fig. 4.2 Rough-wall mean velocity profiles for fully developed flow.

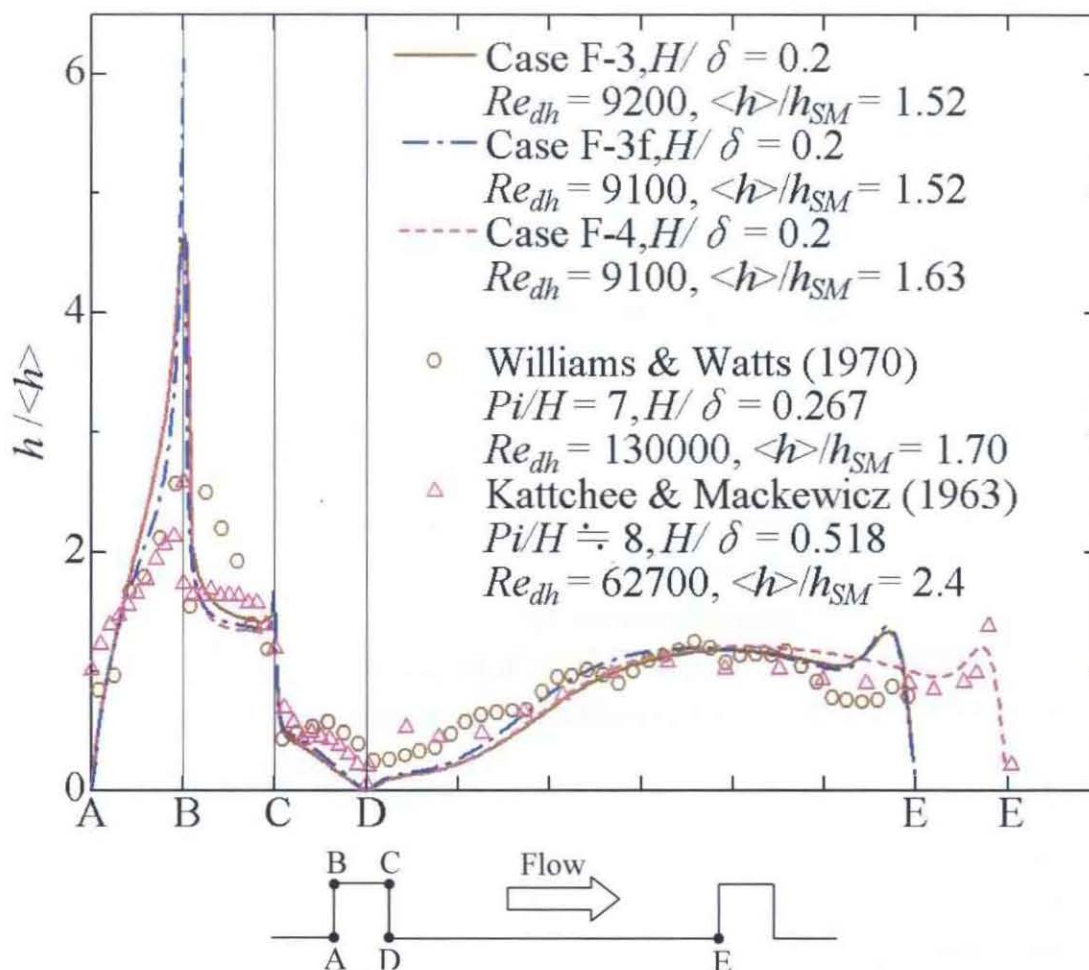


Fig. 4.3 Relative heat transfer coefficient distribution on rough-wall for fully developed flow.

4.5. Hydraulic Loss and Heat Transfer

In Fig. 4.4, presentation is made for the apparent friction factor defined as Eq. (2.4). As suggested by Eq. (2.4), f essentially means the mechanical energy loss. In Fig. 4.4, f is computed for each cavity, selecting reference positions x_u and x_d on the middle of upstream and downstream ribs of the cavity. The origin in the streamwise direction is located at the front surface of the first rib. Since results of Case F-3 and Case F-3f are almost same, the f in the developing flow for $Pi/H = 7$ is calculated from Case F-3. In the fully developed flows, the f for $Pi/H = 9$ is the highest and nearly equals to that for $Pi/H = 8$. The results in the fully developed flows are similar to the sum of the skin-frictional and form drags by Leonardi et al.⁽⁸⁾ In the developing flows, the value of f decreases as flow goes downstream in the case of $Pi/H = 2$, and it oscillates to show alternating rise and fall in $Pi/H = 7$ and 8. In the case of $Pi/H = 4$, f is almost constant, and the trend of f is medium among the other cases. However, the relation between f and Pi/H is generally similar to the fully developed flows.

To evaluate heat transfer, the spatial mean Nusselt number defined as Eq. (2.5) is shown in Fig. 4.5. The reference positions, x_u and x_d , are the same as f . The mean

Nusselt numbers are similar to the friction factors (Fig. 4.4) in fully developed region, whereas fully developing region has difference. About $x/\delta = 1.0$, the mean Nusselt numbers of $Pi/H = 2$ and 4 are approximately or above those of $Pi/H = 7$ and 8.

Efficiency of heat transfer enhancement is examined through the correlation of the mean Nusselt number for a smooth channel as a function of fRe_m^3 , i.e., an indicator of pumping power. Using Eq. (2.10), the efficiency parameter, $\langle \varepsilon \rangle$, can be written as

$$\langle \varepsilon \rangle = \frac{\langle Nu \rangle}{0.0308 Pr^{0.5} (f Re_m^3)^{6/55}} \quad (4.2)$$

which is the ratio of the heat transfer rate to the smooth channel consuming the same pumping power. Figure 4.6 shows the efficiency parameter. In the most part of the channel, the efficiency parameters of ribbed channels are higher than that of the smooth channel, and the heat transfer enhancement by ribs thus is practically meaningful even when the hydraulic loss is considered. In the fully developed cases, $Pi/H = 9$ has the highest performance, and $Pi/H = 8$ is second. The results in the fully developed flows are similar to the analysis by Lewis⁽¹⁾. In the developing cases, I would like to emphasize that $Pi/H = 4$ have higher efficiency than $Pi/H = 7$ and 8 in the most part of the channel. Therefore, the preferred arrangement of ribs is different between developing and developed regions.

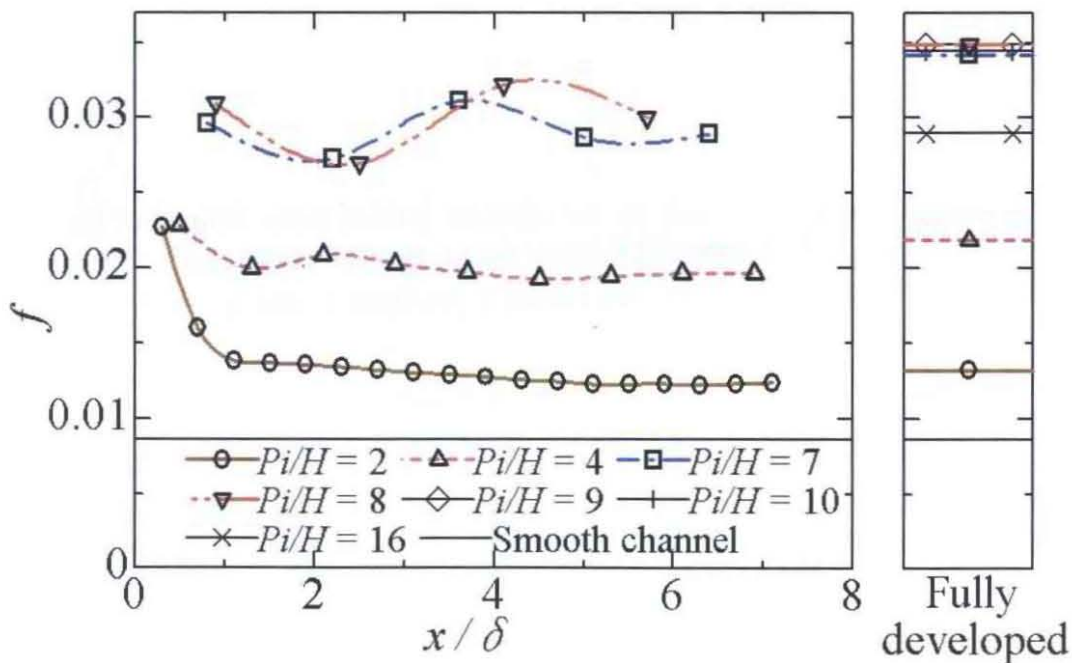


Fig. 4.4 Apparent friction factor from mid-crest to next mid-crest.

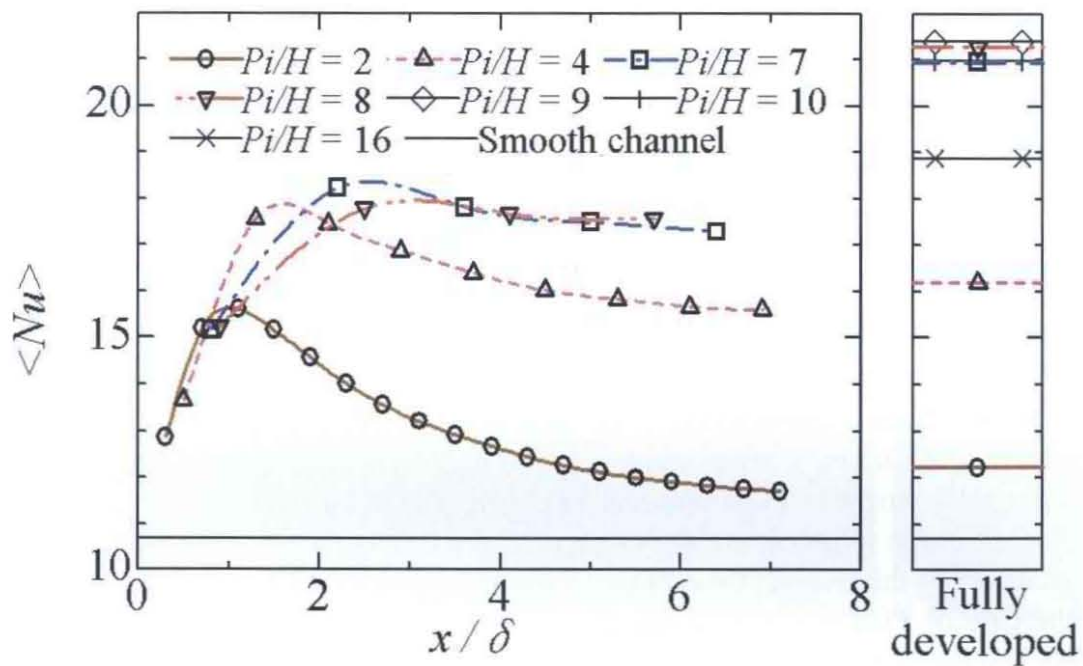


Fig. 4.5 Mean Nusselt number from mid-crest to next mid-crest.

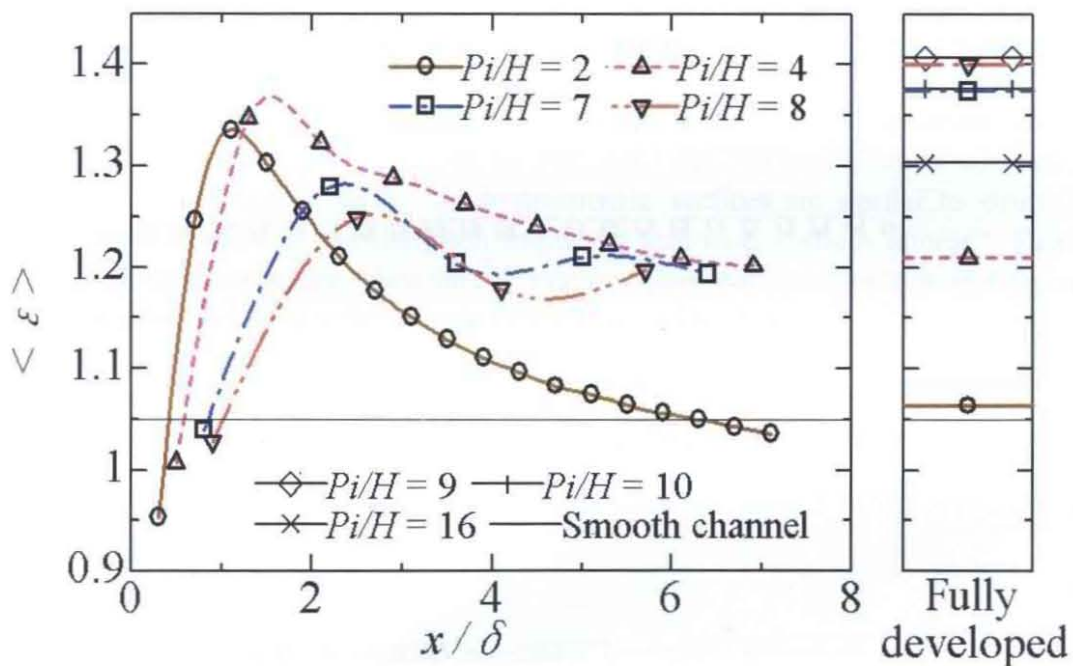


Fig. 4.6 Efficiency parameter from mid-crest to next mid-crest.

4.6. Turbulence Statistics of Flow

Figure 4.7 shows stream lines of mean flow for $Pi/H = 2, 4, 8$ from the spatially developing simulation and the simulation with streamwise periodicity. Compared with smaller values of rib pitch, $Pi/H = 2$ or 4 , the case of $Pi/H = 8$ exhibits complexity in the cavity flow between ribs. In the periodic case for $Pi/H = 8$, separation bubbles are separated to majorly two fractions before and behind the rib, and the stream line passing

nearby the rib top penetrates deeply inside the cavity. In this case, it is suggested that the fluid exchange is active between the cavity flow and the main stream. Such a fluid exchange should positively contribute to refreshing the thermal stagnation which is likely to occur inside the cavity, although such an exchange should negatively lead to a hydrodynamic load which increases pressure loss penalty. The better performance of $Pi/H = 8$ in the efficiency parameter is thought to occur with being aided by the positive aspect of it.

In the developing regions, stream lines are mostly similar to the periodic regions. However, the circulating flow in each of the first cavity grows more than other cavity, and the first rib is suggested to displace the mean flow heavily diverging it away from the rib top. Such a displacement is the most eminent in the case of $Pi/H = 8$, and the disadvantage of its heat transfer in initial region is thought to occur partly because of it.

Figure 4.8 shows contours of turbulent kinetic energy for $Pi/H = 2, 4, 8$. In the case of $Pi/H = 2$, the turbulent energy is large only near the first rib, and change of the boundary layer thickness is thought to dominate the pressure loss as earlier mentioned. In the case of $Pi/H = 8$, the turbulent energy gradually increases into the developed value, and the increased turbulence is thought to collect the fast fluid into the near wall layer enhancing the pressure loss. These distributions correspond to the friction factor (Fig. 4.4).

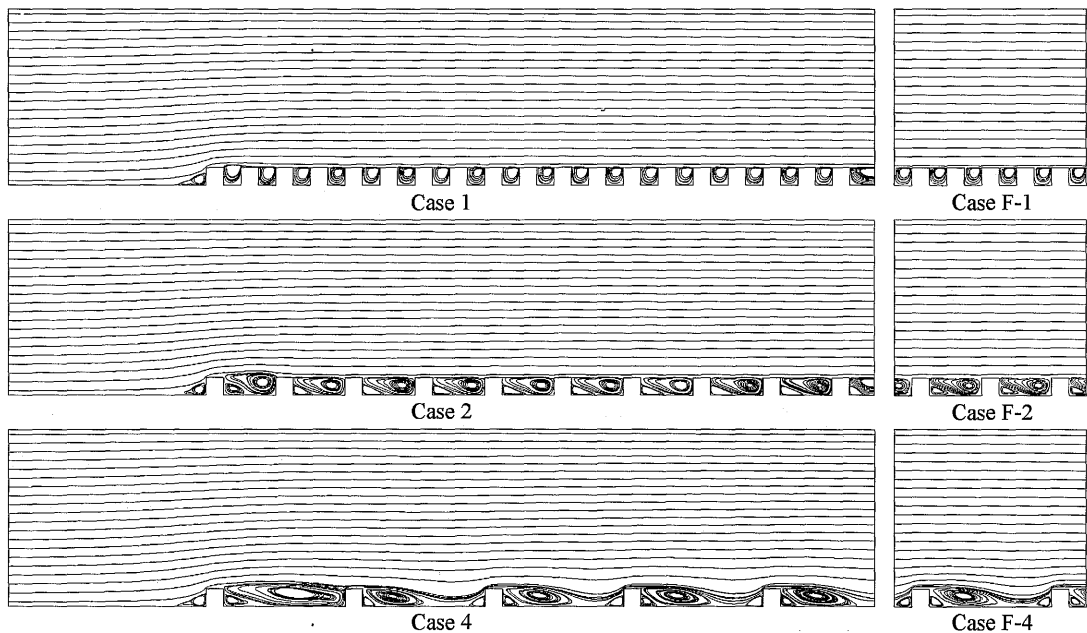


Fig. 4.7 Stream lines of mean velocity.

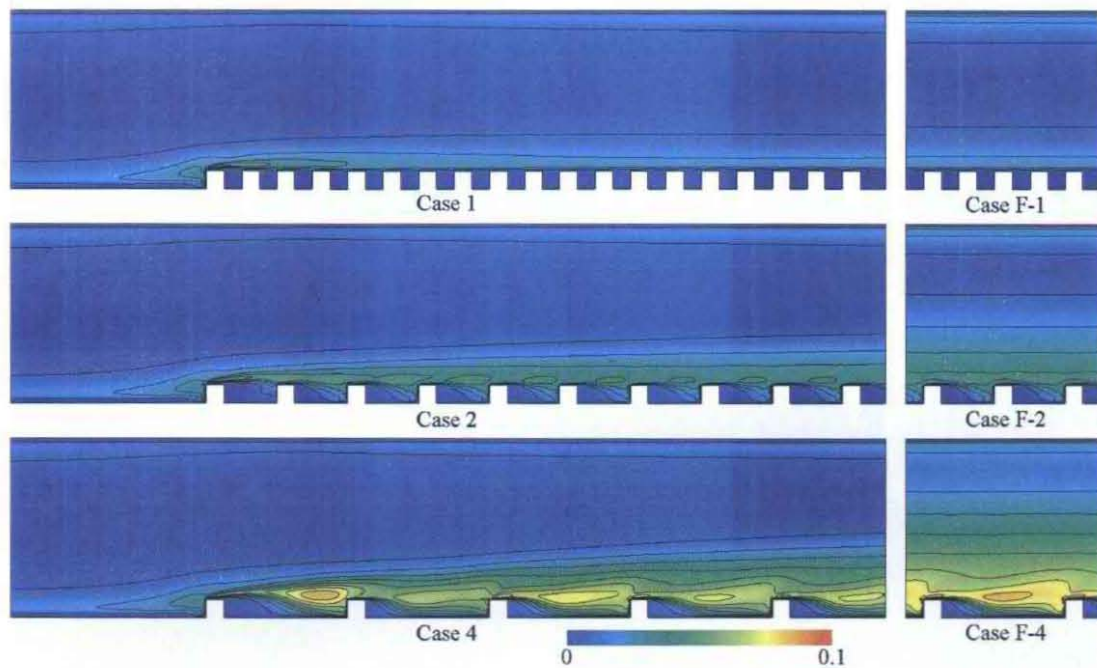
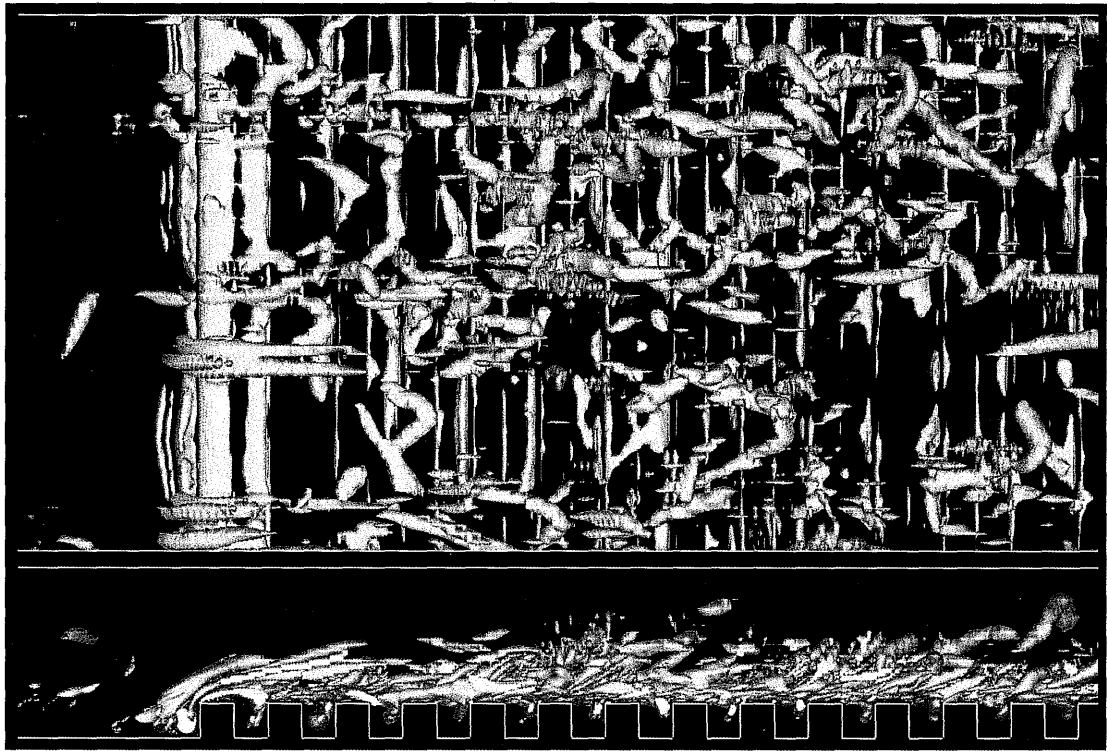


Fig. 4.8 Turbulent kinetic energy normalized by bulk mean velocity. One contour level denotes 0.01.

4.7. Vortex Structures

To observe the vortex structures, iso-surfaces of the second invariant of the velocity-gradient tensor are presented in Fig. 4.9. In $Pi/H = 2$, quasi-streamwise vortices can be recognized in it. Such streamwise vortices are similar to structures near the smooth wall⁽¹¹⁾. As the pitch increases, spanwise vortices appear. Hence, although the vortex structure when the rib pitch is narrow is close to that of a smooth wall, the peculiar turbulent structure can be seen in a wide pitch.

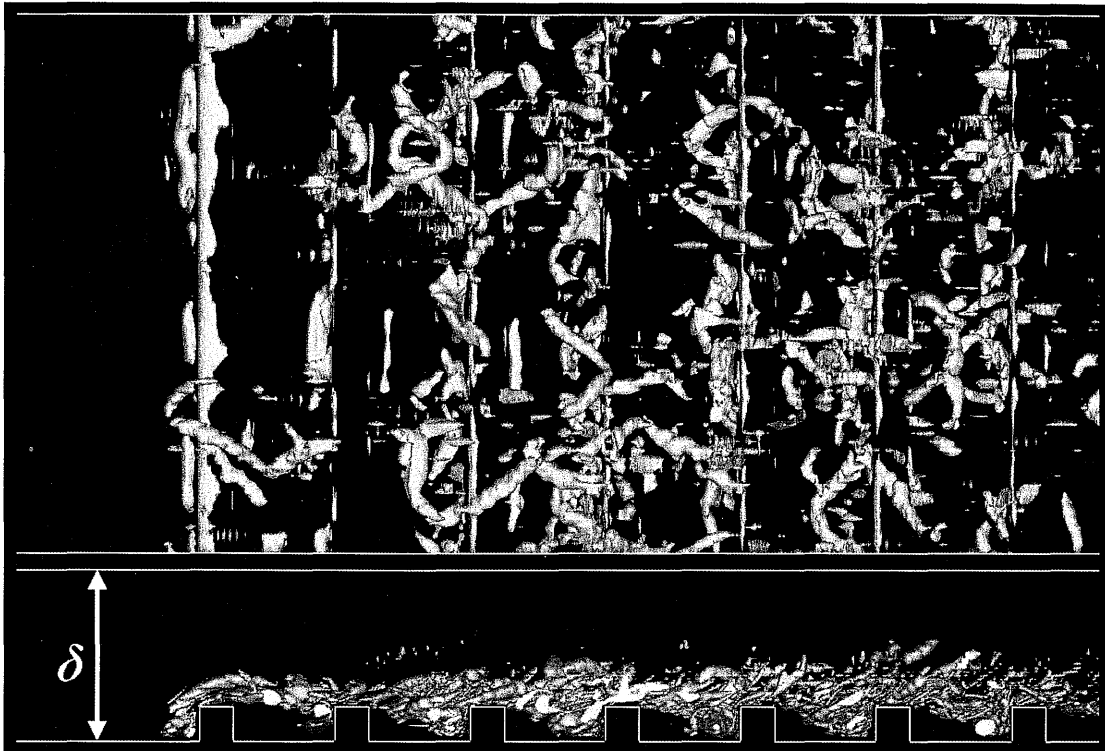


(a) Case 1, $Q\delta^2/u_m^2 = 5$

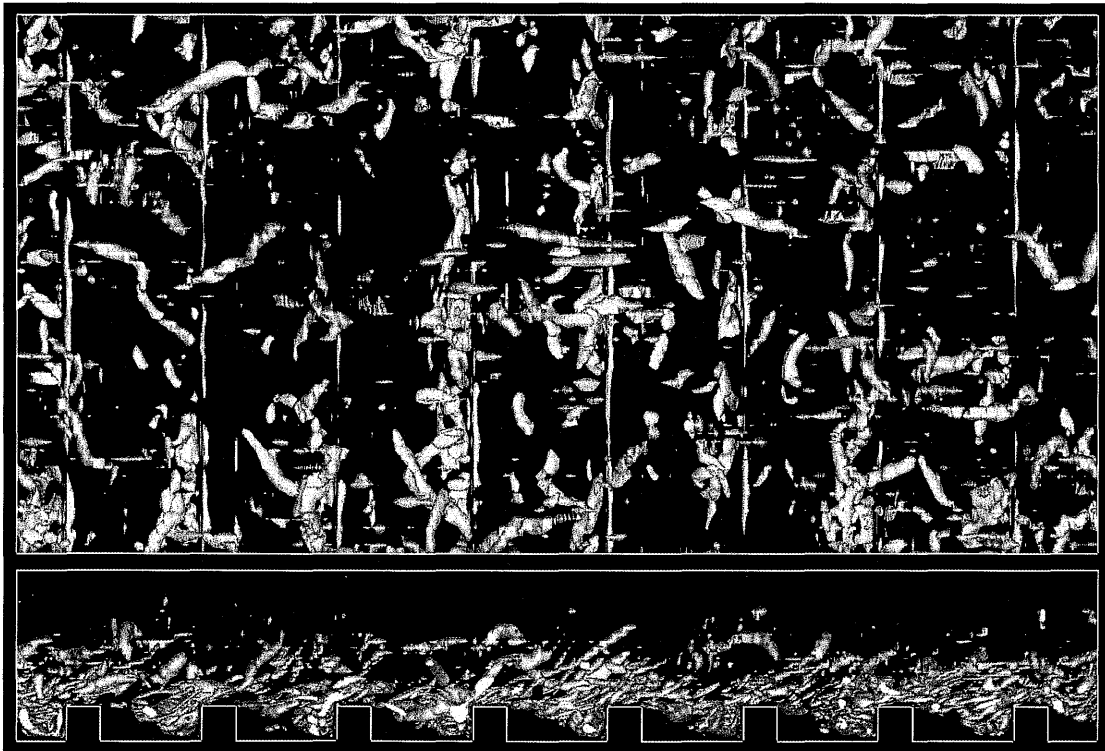


(b) Case F-1, $Q\delta^2/u_m^2 = 5$

Fig. 4.9 Vortex structures visualized by iso-surfaces of second invariant.

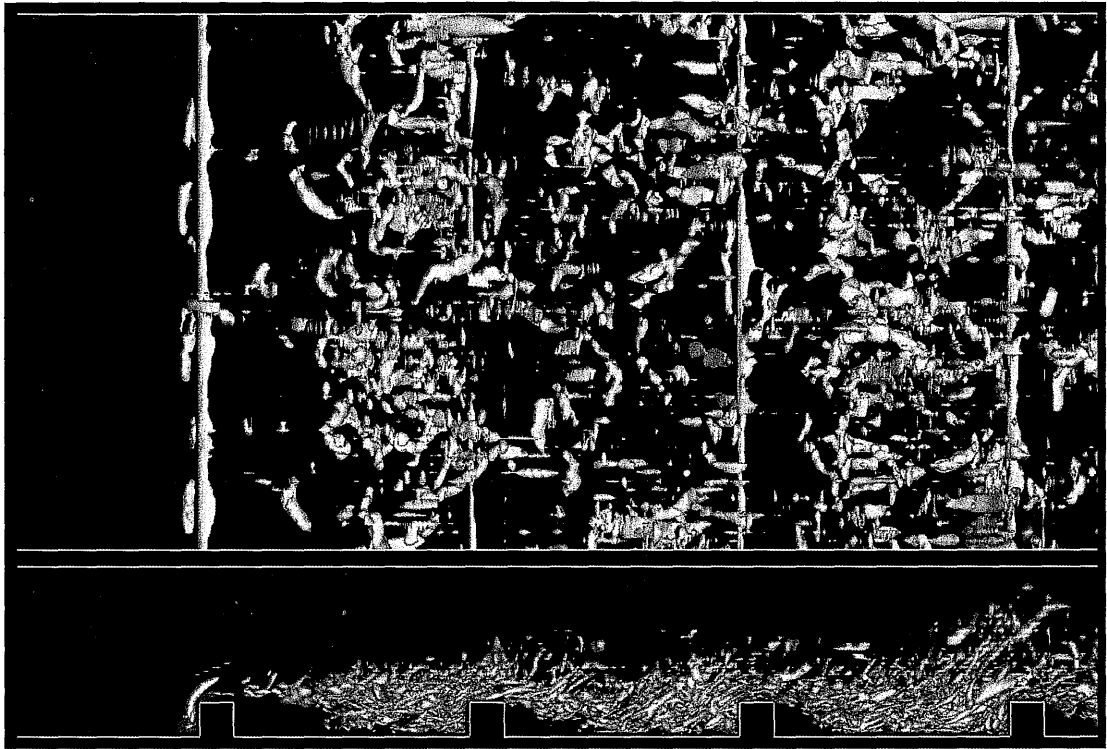


(c) Case 2, $Q\delta^2/u_m^2 = 20$

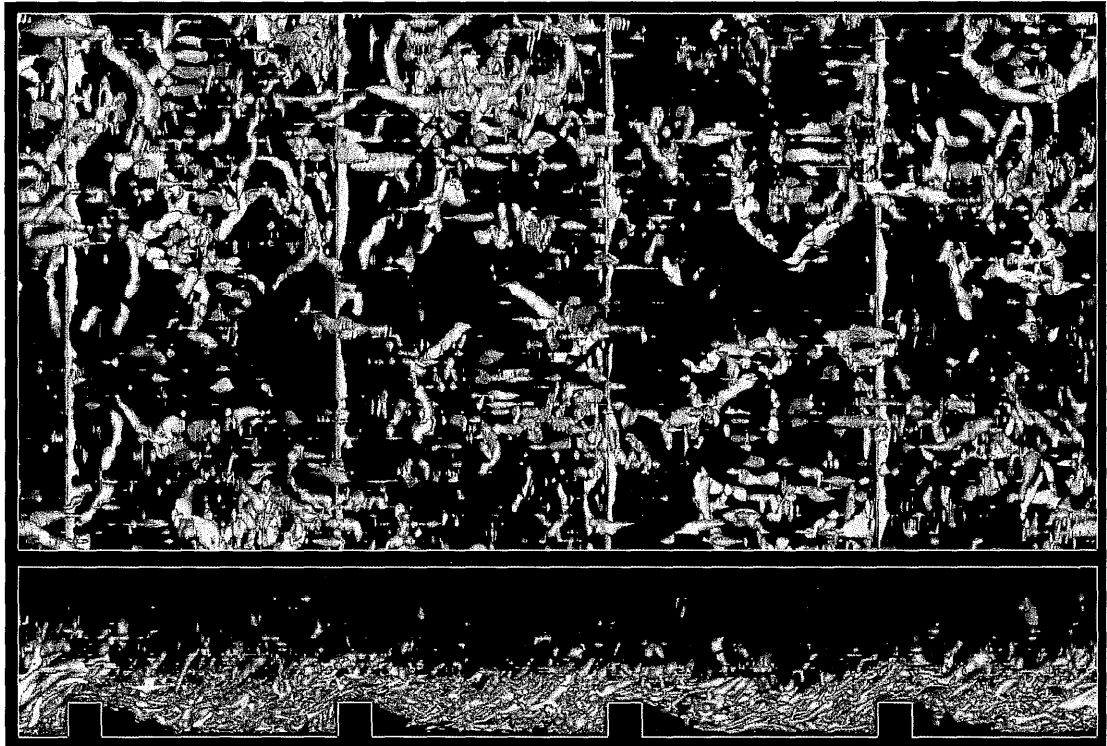


(d) Case F-2, $Q\delta^2/u_m^2 = 20$

Fig. 4.9 Vortex structures visualized by iso-surfaces of second invariant.



(e) Case 4, $Q\delta^2/u_m^2 = 40$



(f) Case F-4, $Q\delta^2/u_m^2 = 40$

Fig. 4.9 Vortex structures visualized by iso-surfaces of second invariant.

4.8. Turbulence Statistics of Temperature

Contours of mean temperature are shown in Fig. 4.10. In $Pi/H = 2$, the fluids inside cavities are low temperature, and the heat exchange between the cavity and the mainstream is inactive. In $Pi/H = 8$, the heat exchange is active because high temperature fluid goes into the cavities.

In the developing regions, the undeveloped thermal layer comes to the ribbed channels in all the pitches, and the rough surfaces are exposed to high temperature. Therefore, $Pi/H = 2$ and 4 have high heat transfer in spite of weak turbulence.

The wall-normal turbulent heat flux is shown in Fig. 4.11. The turbulent heat flux is negative above the first rib and is negative or low in the first cavity in all the cases, i.e. turbulence is not working to heat transport effectively. It is likely that the low fluxes cause the disappointing performance from the first rib to the second rib. Behind the first cavities, the turbulent heat fluxes are high by the thin thermal layers.

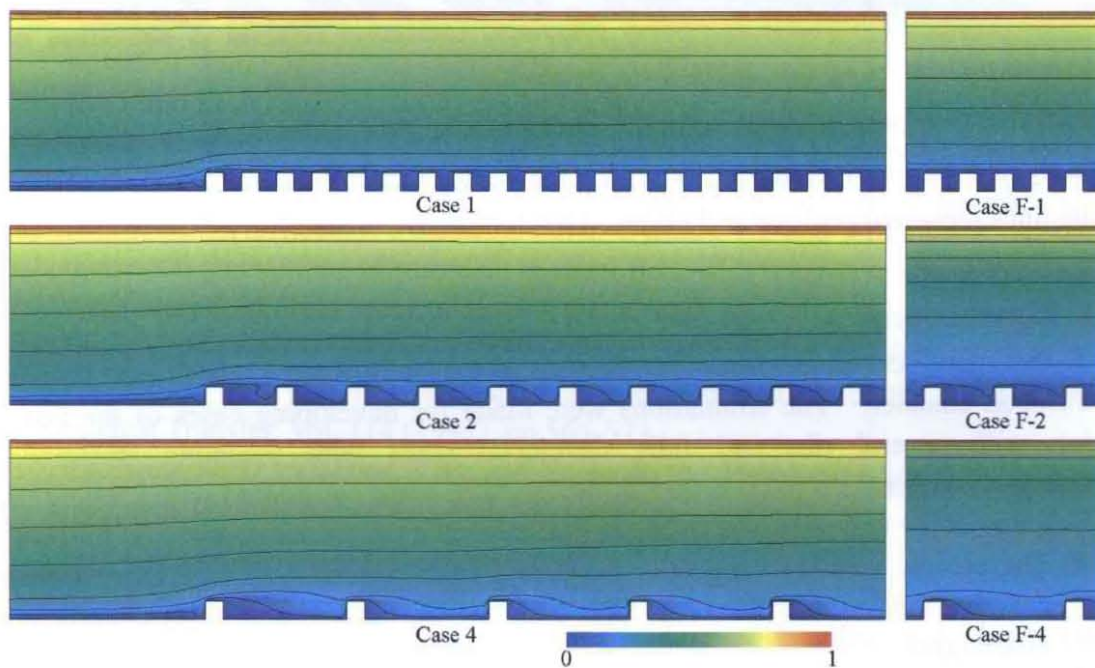


Fig. 4.10 Contours of mean temperature, $(\bar{T} - T_r)/(T_s - T_r)$. One contour level denotes 0.1.

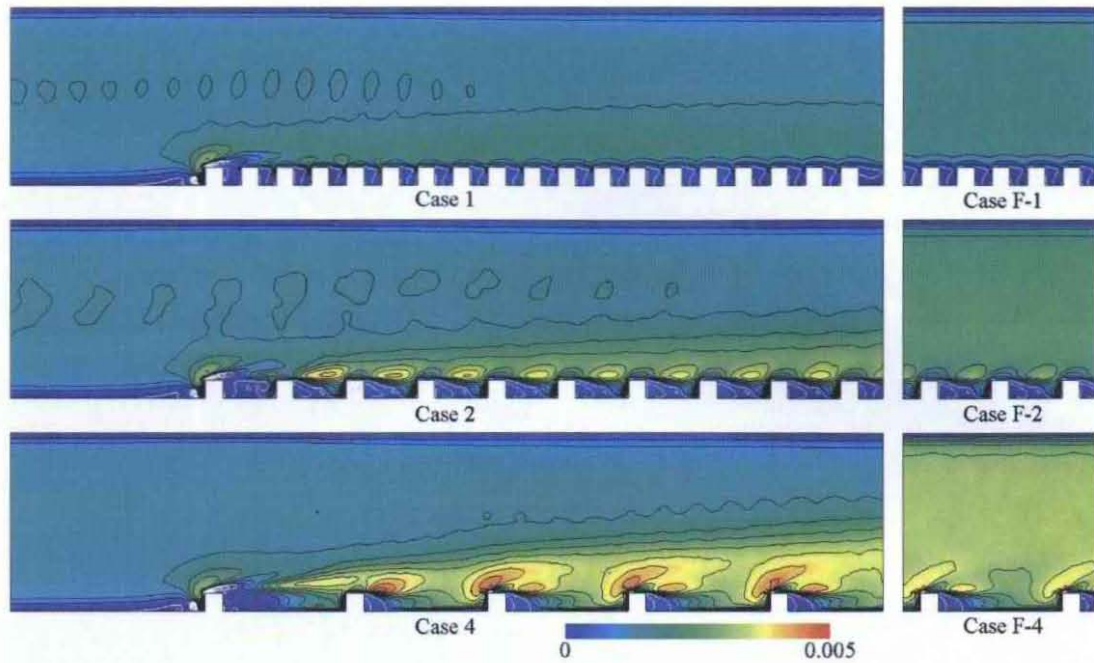


Fig. 4.11 Contours of wall-normal turbulent heat flux normalized by bulk mean velocity and wall temperature difference. One contour level denotes 0.0005. Black and white lines represent positive and negative (include zero), respectively.

4.9. Conclusions

Direct numerical simulations were performed for air flows and related heat transfer in a ribbed channel. The simulations were made for developing cases of the initial region with several ribs and fully developed cases with assuming streamwise periodicity. Several rib pitch-to-height ratios, Pi/H , were considered with keeping the rib height at $H/\delta = 0.2$. The conclusions thus extracted can be summarized as follows.

- The present results of the fully developed cases agreed well with experimental data on the mean velocity profile and on the local heat transfer coefficient distribution.
- $Pi/H = 8$ or 9 had the maximum friction factor in both developing and fully developed flows. Although mean Nusselt number was also the highest for $Pi/H = 9$ in fully developed, that of $Pi/H = 2$ or 4 was the highest in the initial region.
- Heat transfer characteristics were analyzed through the enhancement ratio of heat transfer in the ribbed cases to the smooth channel consuming the same pumping power. According to such analysis, the wide rib spacing ($Pi/H \approx 9$) showed the best performance for the fully developed region, but the narrower spacing ($Pi/H = 2$ or 4) was better than the wide spacing in the developing region.
- Turbulence was active between the first rib and the second rib, but the efficiency was low because the turbulence had a harmful influence on heat transfer.
- A thin thermal layer came to the initial region of the ribbed channels, and the rough surfaces were exposed to high temperature. Therefore, $Pi/H = 2$ and 4 had high heat transfer in spite of low pumping loss.

4.10. References

- (1) Lewis, M. J., Optimising the thermohydraulic performance of rough surfaces, *International Journal of Heat and Mass Transfer*, Vol. 18 (1975), pp.1243-1248.
- (2) Hanjalić, K., and Launder, B. E., Fully developed asymmetric flow in a plane channel, *Journal of Fluid Mechanics*, Vol. 51 (1972), pp.301-335.
- (3) Williams, F., and Watts, J., The development of rough surfaces with improved heat transfer performance and a study of the mechanisms involved, *Fourth International Heat Transfer Conference* (1970), FC 5.5.
- (4) Kattchee, N., and Mackewicz, W. V., Effects of boundary layer turbulence promoters on the local film coefficients of ML-1 fuel elements, *Nuclear Science and Engineering*, Vol. 16 (1963), pp.31-38.
- (5) Miyake, Y., Tsujimoto, K., and Nakaji, M., Direct numerical simulation of rough-wall heat transfer in a turbulent channel flow, *International Journal of Heat and Fluid Flow*, Vol. 22 (2001), pp.237-244.
- (6) Nagano, Y., Hattori, H., and Houra, T., DNS of velocity and thermal fields in turbulent channel flow with transverse-rib roughness, *International Journal of Heat and Fluid Flow*, Vol. 25 (2004), pp.393-403.
- (7) Ikeda, T., and Durbin, P. A., Direct simulations of a rough-wall channel flow, *Journal of Fluid Mechanics*, Vol. 571 (2007), pp.235-263.
- (8) Leonardi, S., Orlandi, P., Smalley, R. J., Djenidi, L., and Antonia, R. A., Direct numerical simulations of turbulent channel flow with transverse square bars on one wall, *Journal of Fluid Mechanics*, Vol. 491 (2003), pp.229-238.
- (9) Liou, T. M., and Hwang, J. J., Developing heat transfer and friction in a ribbed rectangular duct with flow separation at inlet, *Transactions of the ASME, Journal of Heat Transfer*, Vol. 114 (1992), pp.565-573.
- (10) Cardwell, N. D., Vlachos, P. P., and Thole, K. A., Developing and fully developed turbulent flow in ribbed channels, *Experiments in Fluids*, Vol. 50, No. 5 (2011), pp.1357-1371.
- (11) Jeong, J., Hussain, F., Schoppa, W. and Kim, J., Coherent structures near the wall in a turbulent channel flow, *Journal of Fluid Mechanics*, Vol. 332 (1997), pp.185-214.

Chapter 5 Curved Channel Flow with a Single Rib

5.1. Introduction

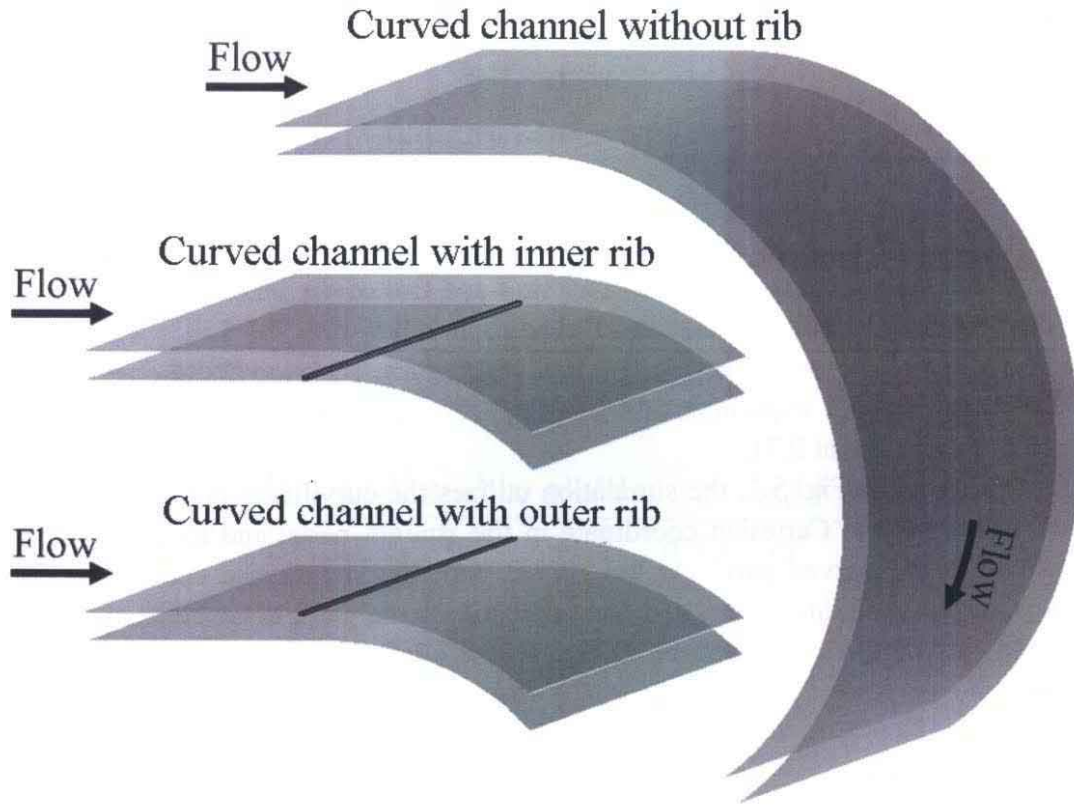
The two-dimensional flow in a curved channel has been of great interest for researchers and engineers, since flows in many cases have a streamline curvature affecting the scalar transport severely. For example, the internal combustion engine utilizes swirl and tumble flows to enhance the mixing, and the streamline curvature triggers flow instability to increase the turbulent transport.

As a basic model of the curved flow, two-dimensional flows between curved walls can provide a good arena for discussing the effects from curvature on the fluid mixing and heat transfer enhancement⁽¹⁾⁻⁽⁸⁾. So far, lots of academic works have been made for the transition from a laminar to turbulent flow⁽¹⁾⁻⁽⁵⁾, and the multi-scale structures in a two-dimensional curved channel⁽⁶⁾⁻⁽⁸⁾. Kobayashi et al.^{(6), (7)} measured turbulence statistics in a curved channel using the hot-wire anemometry. They reported streamwise variation of the mean velocity, Reynolds stress and triple correlation, and pointed out that turbulence quantities were controlled by the organized large-scale vortex. Moser and Moin⁽⁸⁾ directly solved the Navier-Stokes equations to predict the curved channel flow, and they captured complete data of the turbulent flow including the organized motion. Recently, Matsubara et al.^{(9), (10)} simulated spatially advancing flow and heat transfer in a curved channel, and reported that near-wall micro-scale structures increased the size and strength to grow into organized structures. However, its flow control with heat transfer is incomplete.

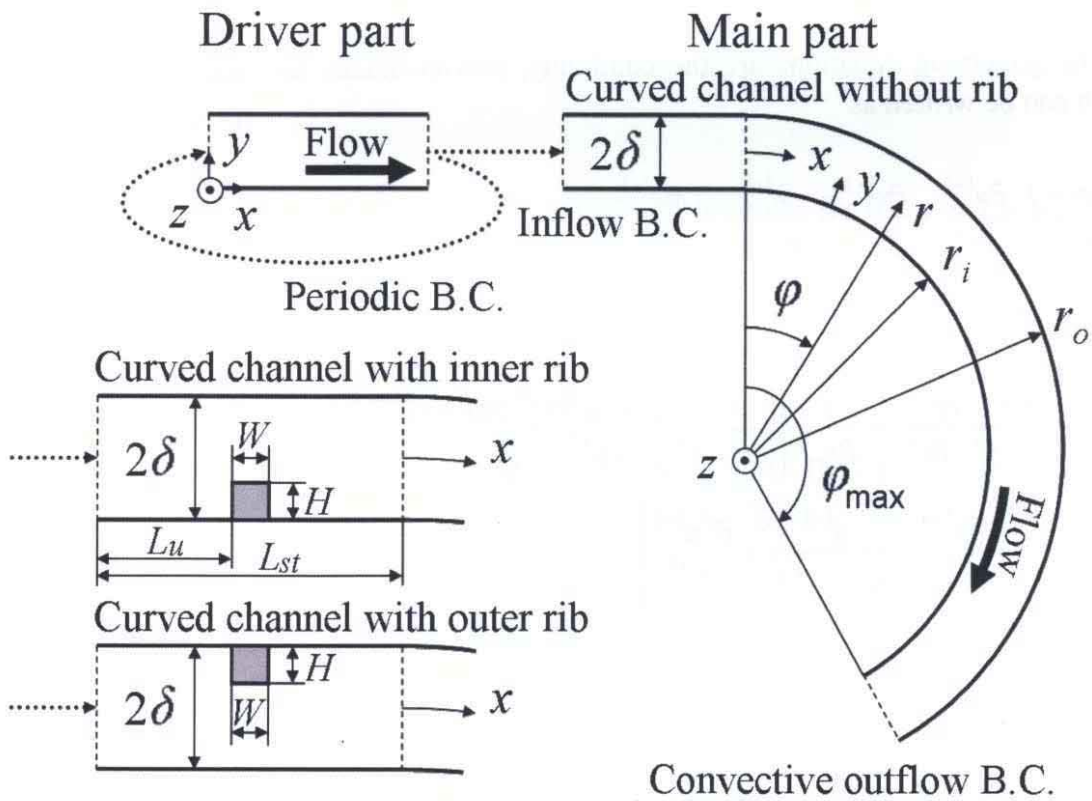
This study is an extension of the work by Matsubara et al. Purpose of the present study is to reveal effects of a rectangular rib placed in a straight connector introducing fully developed turbulence into the curved channel. Flow and heat transfer characteristics are discussed for the cases where a rib is placed on either the inner or outer wall and for the case of no rib on the walls.

5.2. Numerical Methods

The computational domain and the coordinate system are shown in Fig. 5.1. The computation was made by two separate domains: the driver and the curved channel. The fully developed flow is simulated by the driver, and is introduced into the curved channel having the straight portion at the upstream end. The driver flow is periodic in the streamwise and spanwise directions. The curved channel flow is periodic only in the spanwise direction, employing the convection outflow condition at the channel exit. The non-slip condition is used for the solid walls. In the driver and the curved channel, the inner and outer walls have a temperature difference and temperature is uniform on each wall. A rectangular rib is placed on the outer wall or the inner wall of the straight part connecting to the curved part. The rib is the same temperature as the ribbed wall.



(a) Outline of geometry



(b) Computational domain and coordinate system

Fig. 5.1 Two-dimensional curved channel.

The radius ratio of the curved channel

$$\alpha = \frac{r_i}{r_o} \quad (5.1)$$

is 0.92 which is the same as the experiment by Kobayashi et al.^{(6), (7)} In Eq. (5.1), r_o and r_i are the curvature radius of the outer wall and that of the inner wall, respectively. The straight flow is simulated at the Reynolds number, $Re_{\tau 0}$, of 150. The resulted mean flow Reynolds number is $Re_m = 4,560$, which corresponds to about one fourths of the Kobayashi et al.'s experiment ($Re_m = 20,000$). For air as the chosen fluid, the Prandtl number is set at 0.71.

As illustrated in Fig. 5.1, the simulation utilizes the curvilinear coordinate (x, y, z) which represents the Cartesian coordinate in the straight parts, and to the cylindrical coordinate in the curved part. In the curved part, the streamwise coordinate x is a distance along the middle plane, and the radial coordinate y is a distance from the inner wall. In this part, x and y can be related to the angle φ and the curvature radius r through

$$x = r_m \varphi = \frac{r_i + r_o}{2} \varphi \quad (5.2)$$

$$y = r - r_i \quad (5.3)$$

The governing equations are the continuity, Navier-Stokes and energy equations, which can be written as

$$\frac{\sigma + 1}{\sigma + y^*} \frac{\partial u^{(+)}}{\partial x^*} + \frac{\partial v^{(+)}}{\partial y^*} + \frac{v^{(+)}}{\sigma + y^*} + \frac{\partial w^{(+)}}{\partial z^*} = 0 \quad (5.4)$$

$$\frac{\partial u^{(+)}}{\partial t^*} + \frac{\sigma + 1}{\sigma + y^*} u^{(+)} \frac{\partial u^{(+)}}{\partial x^*} + v^{(+)} \frac{\partial u^{(+)}}{\partial y^*} + \frac{u^{(+)} v^{(+)}}{\sigma + y^*} + w^{(+)} \frac{\partial u^{(+)}}{\partial z^*}$$

$$= -\frac{\sigma + 1}{\sigma + y^*} \frac{\partial p^{(+)}}{\partial x^*} + \frac{1}{Re_{\tau 0}} \left\{ \left(\frac{\sigma + 1}{\sigma + y^*} \right)^2 \frac{\partial^2 u^{(+)}}{\partial x^{*2}} + \frac{2(\sigma + 1)}{(\sigma + y^*)^2} \frac{\partial v^{(+)}}{\partial x^*} + \frac{\partial^2 u^{(+)}}{\partial y^{*2}} \right. \quad (5.5)$$

$$\left. + \frac{1}{\sigma + y^*} \frac{\partial u^{(+)}}{\partial y^*} - \frac{u^{(+)}}{(\sigma + y^*)^2} + \frac{\partial^2 u^{(+)}}{\partial z^{*2}} \right\}$$

$$\begin{aligned} & \frac{\partial v^{(+)}}{\partial t^*} + \frac{\sigma+1}{\sigma+y^*} u^{(+)} \frac{\partial v^{(+)}}{\partial x^*} + v^{(+)} \frac{\partial v^{(+)}}{\partial y^*} - \frac{u^{(+)^2}}{\sigma+y^*} + w^{(+)} \frac{\partial v^{(+)}}{\partial z^*} \\ &= -\frac{\partial p^{(+)}}{\partial y^*} + \frac{1}{Re_{\tau 0}} \left\{ \left(\frac{\sigma+1}{\sigma+y^*} \right)^2 \frac{\partial^2 v^{(+)}}{\partial x^{*2}} - \frac{2(\sigma+1)}{(\sigma+y^*)^2} \frac{\partial u^{(+)}}{\partial x^*} + \frac{\partial^2 v^{(+)}}{\partial y^{*2}} \right. \end{aligned} \quad (5.6)$$

$$\begin{aligned} & \left. + \frac{1}{\sigma+y^*} \frac{\partial v^{(+)}}{\partial y^*} - \frac{v^{(+)}}{(\sigma+y^*)^2} + \frac{\partial^2 v^{(+)}}{\partial z^{*2}} \right\} \\ & \frac{\partial w^{(+)}}{\partial t^*} + \frac{\sigma+1}{\sigma+y^*} u^{(+)} \frac{\partial w^{(+)}}{\partial x^*} + v^{(+)} \frac{\partial w^{(+)}}{\partial y^*} + w^{(+)} \frac{\partial w^{(+)}}{\partial z^*} \\ &= -\frac{\partial p^{(+)}}{\partial z^*} + \frac{1}{Re_{\tau 0}} \left\{ \left(\frac{\sigma+1}{\sigma+y^*} \right)^2 \frac{\partial^2 w^{(+)}}{\partial x^{*2}} + \frac{\partial^2 w^{(+)}}{\partial y^{*2}} + \frac{1}{\sigma+y^*} \frac{\partial w^{(+)}}{\partial y^*} + \frac{\partial^2 w^{(+)}}{\partial z^{*2}} \right\} \end{aligned} \quad (5.7)$$

$$\begin{aligned} & \frac{\partial \theta^*}{\partial t^*} + \frac{\sigma+1}{\sigma+y^*} u^{(+)} \frac{\partial \theta^*}{\partial x^*} + v^{(+)} \frac{\partial \theta^*}{\partial y^*} + w^{(+)} \frac{\partial \theta^*}{\partial z^*} \\ &= \frac{1}{Re_{\tau 0} Pr} \left\{ \left(\frac{\sigma+1}{\sigma+y^*} \right)^2 \frac{\partial^2 \theta^*}{\partial x^{*2}} + \frac{\partial^2 \theta^*}{\partial y^{*2}} + \frac{1}{\sigma+y^*} \frac{\partial \theta^*}{\partial y^*} + \frac{\partial^2 \theta^*}{\partial z^{*2}} \right\} \end{aligned} \quad (5.8)$$

where the parameter σ can be related to the radius ratio α by

$$\sigma = \frac{r_i}{\delta} = \frac{2\alpha}{1-\alpha} \quad (5.9)$$

Equations (5.4)-(5.8) corresponds to the cylindrical formulas for $0 < \alpha < 1.0$ and to the Cartesian formulas for $\alpha \rightarrow 1.0$ ($\sigma \rightarrow +\infty$). These equations are solved by similar procedures as Chapter 2.

Computational conditions are listed in Table 5.1. Case 1 is the straight channel with the single rib. Cases 2, 3, and 4 are the curved channel without a rib, with the inner rib, and with the outer rib respectively.

Table 5.1 Computational conditions.

	Case 1 Rib	Case 2 No rib	Case 3 Inner rib	Case 4 Outer rib
α	1.0 (straight)	0.92	0.92	0.92
$\phi_{\max} [^\circ]$	-	150	150	150
H/δ	0.20	-	0.20	0.20
W/δ	0.25	-	0.25	0.25
$Re_{\tau 0}$	150	150	150	150
Pr	0.71	0.71	0.71	0.71
L_{x0}/δ	3.9	3.9	3.9	3.9
L_x/δ	66.7	66.7	66.7	66.7
L_w/δ	1.8	-	1.8	1.8
L_{st}/δ	-	3.9	3.9	3.9
L_z/δ	3.6	7.2	7.2	7.2
N_{x0}	32	32	32	32
N_x	544	544	544	544
N_y	61	61	61	61
N_z	64	128	128	128
$\Delta x_0^{(+)}$	18.39	18.39	18.39	18.39
$\Delta x^{(+)}$	18.39	18.39	18.39	18.39
$\Delta y^{(+)}$	1.0-14.12	1.0-14.12	1.0-14.12	1.0-14.12
$\Delta z^{(+)}$	8.43	8.43	8.43	8.43

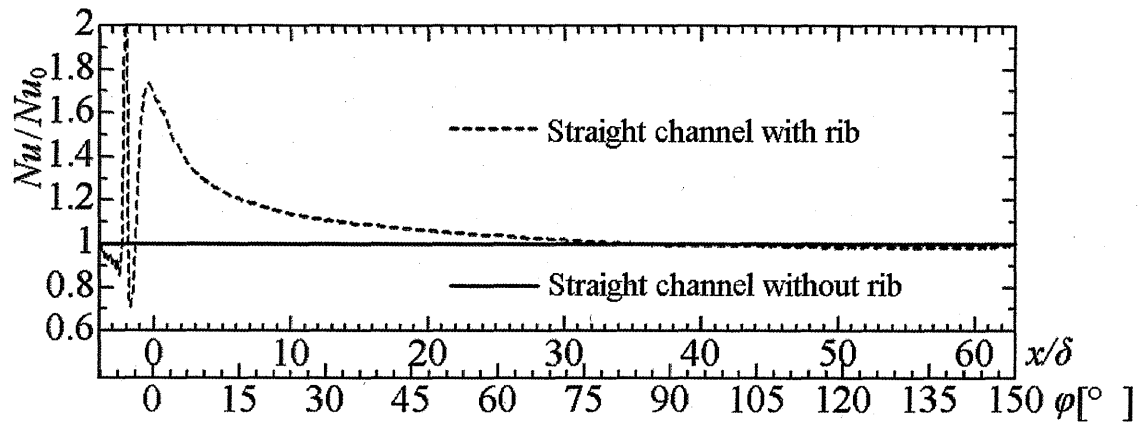
5.3. Heat Transfer Coefficient

Figure 5.2 shows distributions of the Nusselt number. It can be written as

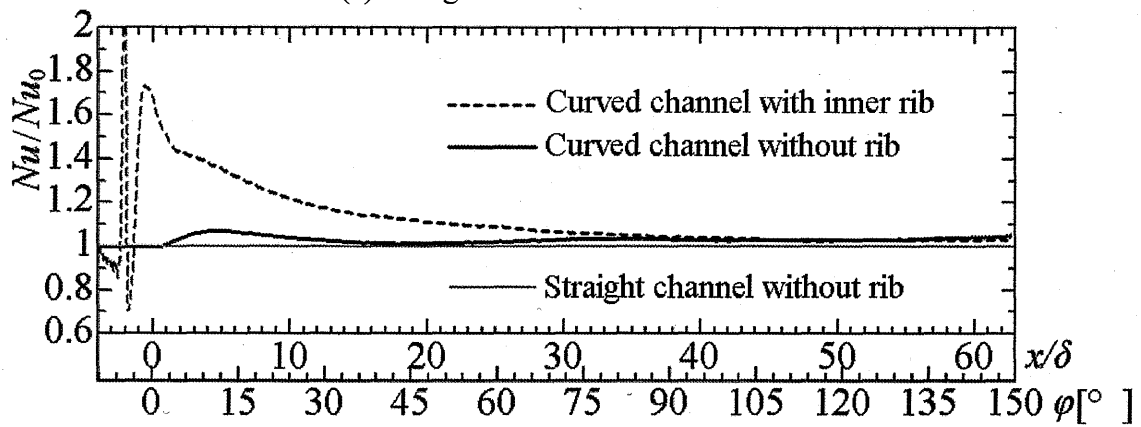
$$Nu = \frac{4\delta}{\lambda(T_i - T_o)} \frac{r_i \bar{q}_{w,i} - r_o \bar{q}_{w,o}}{r_i + r_o} \quad (5.10)$$

which is averaged between the inner and outer walls with weighing according to the surface broadness. The weighted averaging procedure accounts for the difference in the extent of walls in each side.

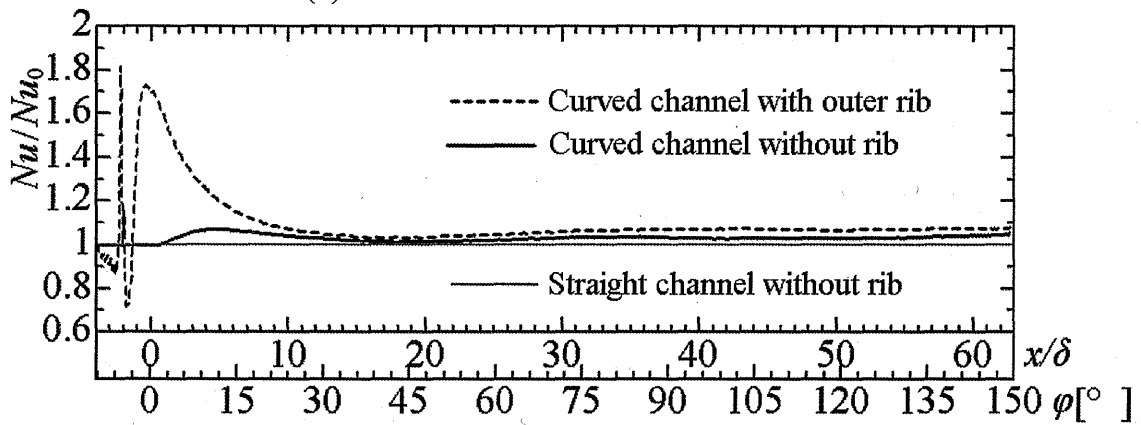
In the case of the straight channel with the rib (Fig. 5.2a), the Nusselt number reaches peaks at $x/\delta \approx -2.0$ (in front of the rib) and at $x/\delta \approx 0$ (the reattachment point). In this case, heat transfer is improved significantly for $0 \leq x/\delta \leq 20$. In the case of the curved channel with the inner rib (Fig. 5.2b), the Nusselt number is higher than that of the straight channel with the rib over $0 \leq x/\delta \leq 20$, and it returns mostly to the values of the curved channel without the rib for $x/\delta \geq 35$. In the case of the outer-rib (Fig. 5.2c), the heat transfer enhancement for $0 \leq x/\delta \leq 20$ is not as large as that of the straight channel with the rib. However the enhancement continues to appear even far from the rib: $x/\delta \geq 30$.



(a) Straight channel with/without rib



(b) Curved channel with/without inner rib



(c) Curved channel with/without outer rib

Fig. 5.2 Local Nusselt number averaged between two walls.

5.4. Mean Velocity Vectors

Figures 5.3-5.5 show time-mean velocity vectors in the curved-channel cases, where irregularity was removed by the time filter, $1200\nu/U_{t0}^2$, corresponding to about 10 times as long as the dissipation time scale at the straight channel center. In the figures, large-scale vortices are clearly depicted. The large-scale vortices contribute significantly to heat transfer⁽¹⁰⁾.

The transition from small-scale structures to large-scale structures is observed in all the curved-channel cases (Figs. 5.3-5.5). In the case of the inner-rib, the large-scale streamwise vortices are comparatively weak and small.

5.5. Power Spectral Density

Figures 5.6-5.8 show contours of the spanwise pre-multiplied power spectra of the wall-normal velocity, $k_z E_{v_{wz}}/U_m^2$. This component was selected because it clearly detects the large-scale motion as suggested in Figs 5.3-5.5. In the straight part (Figs. 5.6(a), 5.7(a), and 5.8(a)), a peak position at the spanwise wave length $\lambda_z/\delta \approx 0.8$ expresses the spacing between low-speed streaks. As the channel angle increases, the peak moves away from the outer wall with its wave length shift toward 2.5δ .

In the inner-rib case (Fig. 5.7), the power is increased in inner wall side at $\phi = 15^\circ$ and 45° but is comparatively weak on the whole from $\phi = 75^\circ$ to $\phi = 135^\circ$. The increase near the inner wall is generated by the rib, and the decrease suggests that the growth of the large-scale vortices is hindered. In the case of the outer-rib, the maximums and its wave length are larger than those without the rib, and it is likely that the growth of the large-scale vortices is improved. These results correspond to the heat transfer coefficients.

5.6. Thermo-Hydraulic Performance

Pumping power and heat transfer in the channels are evaluated as the previous chapters. Figure 5.9 shows the relation between pumping power and mean Nusselt number. The apparent friction factor, f , is calculated by Eq. (2.4). The mean Nusselt number is defined as

$$\langle Nu \rangle = \frac{I}{x - x_0} \int_{x_0}^x Nu dx \quad (5.11)$$

The correlation of a straight channel without a rib is led by Eq. (2.9) or Eq. (2.10).

From the figure, all the cases have higher performance than a straight channel without a rib. In the three cases with the rib, the inner-rib case has the best performance. However, the outer-rib case moves up strongly in the second half of the channel.

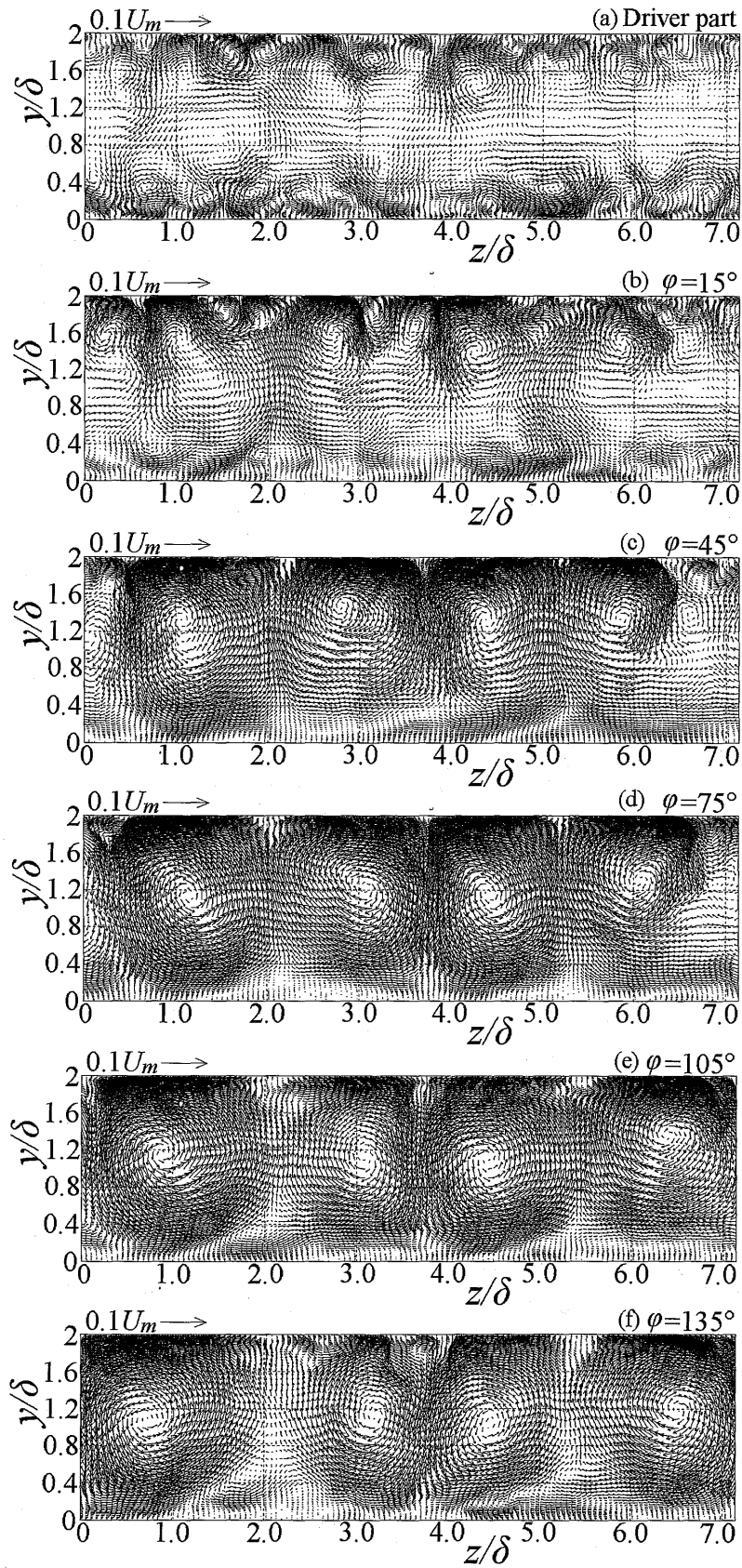


Fig. 5.3 Mean velocity vectors in y - z planes of curved channel without rib.

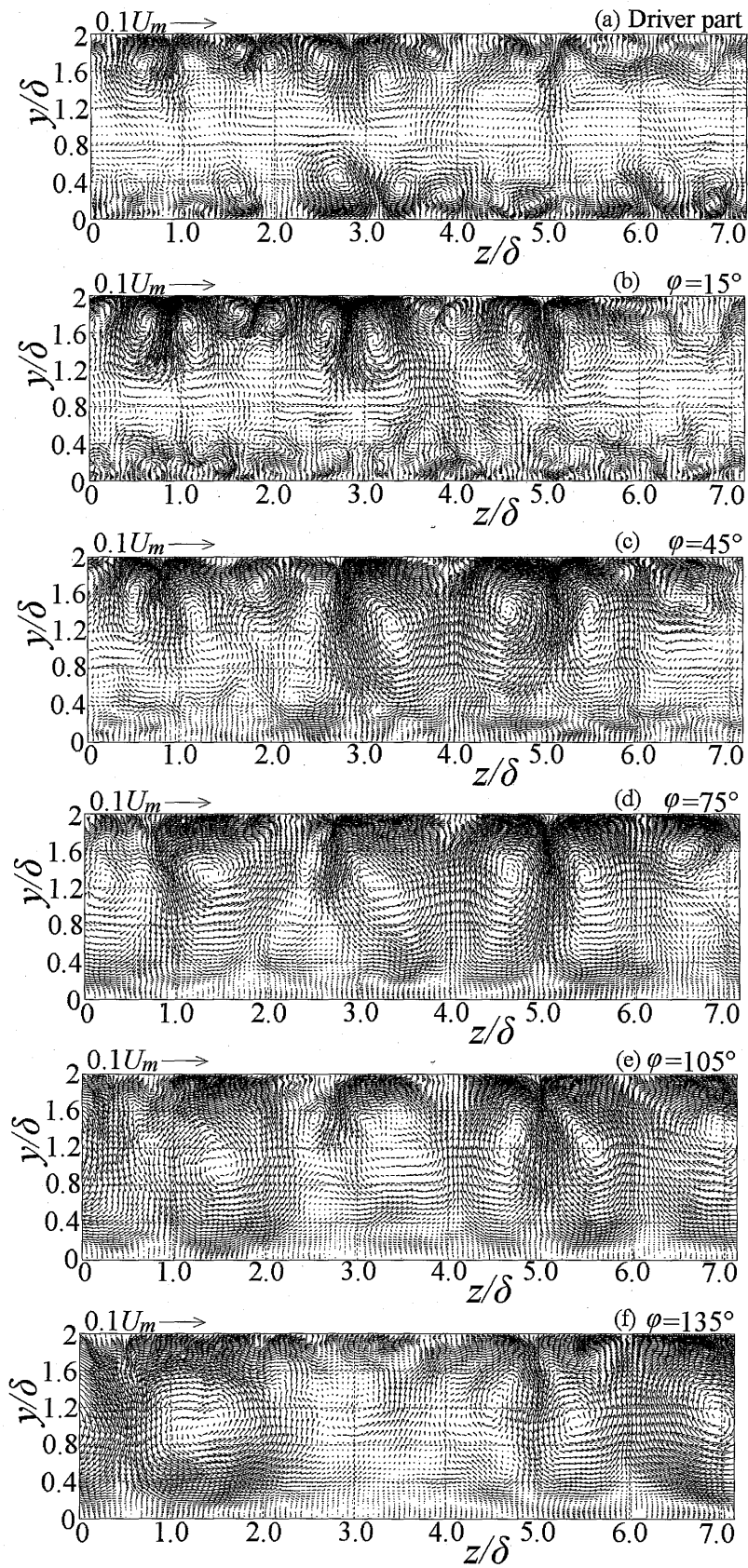


Fig. 5.4 Mean velocity vectors in y - z planes of curved channel with inner rib.

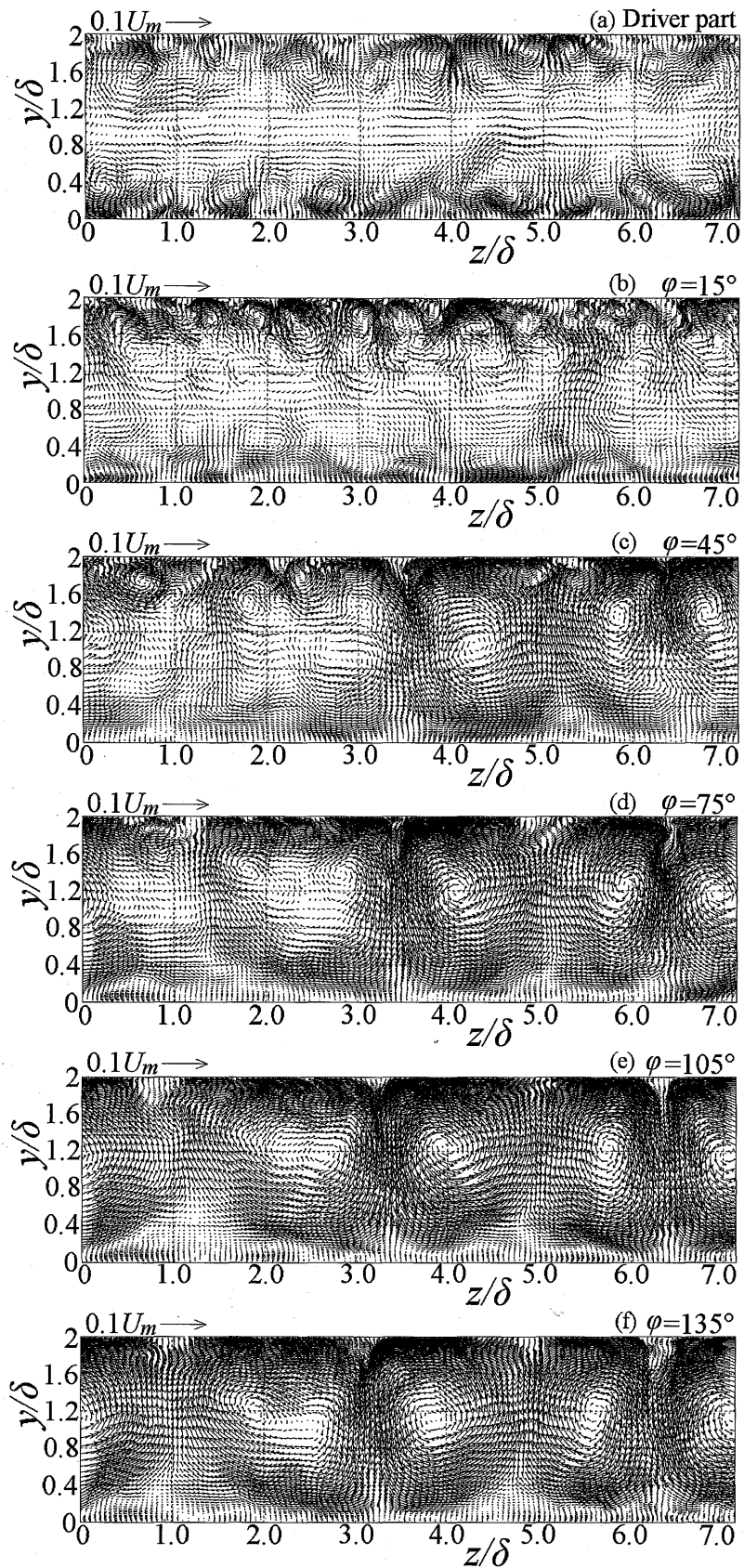


Fig. 5.5 Mean velocity vectors in y - z planes of curved channel with outer rib.

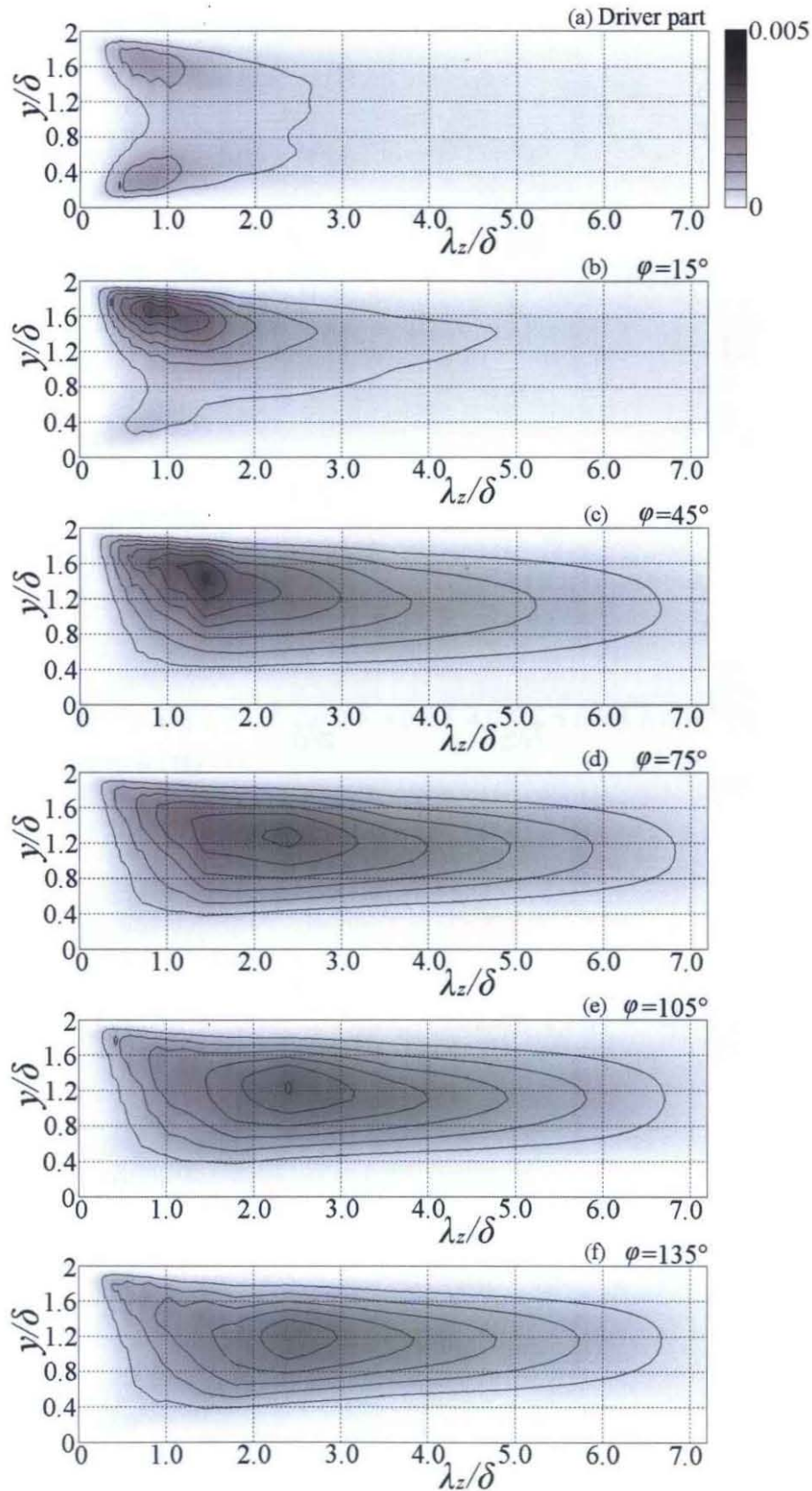


Fig. 5.6 Contours for spanwise pre-multiplied power spectra of wall-normal velocity, $k_z E_{vvz}/U_m^2$, in curved channel without rib.

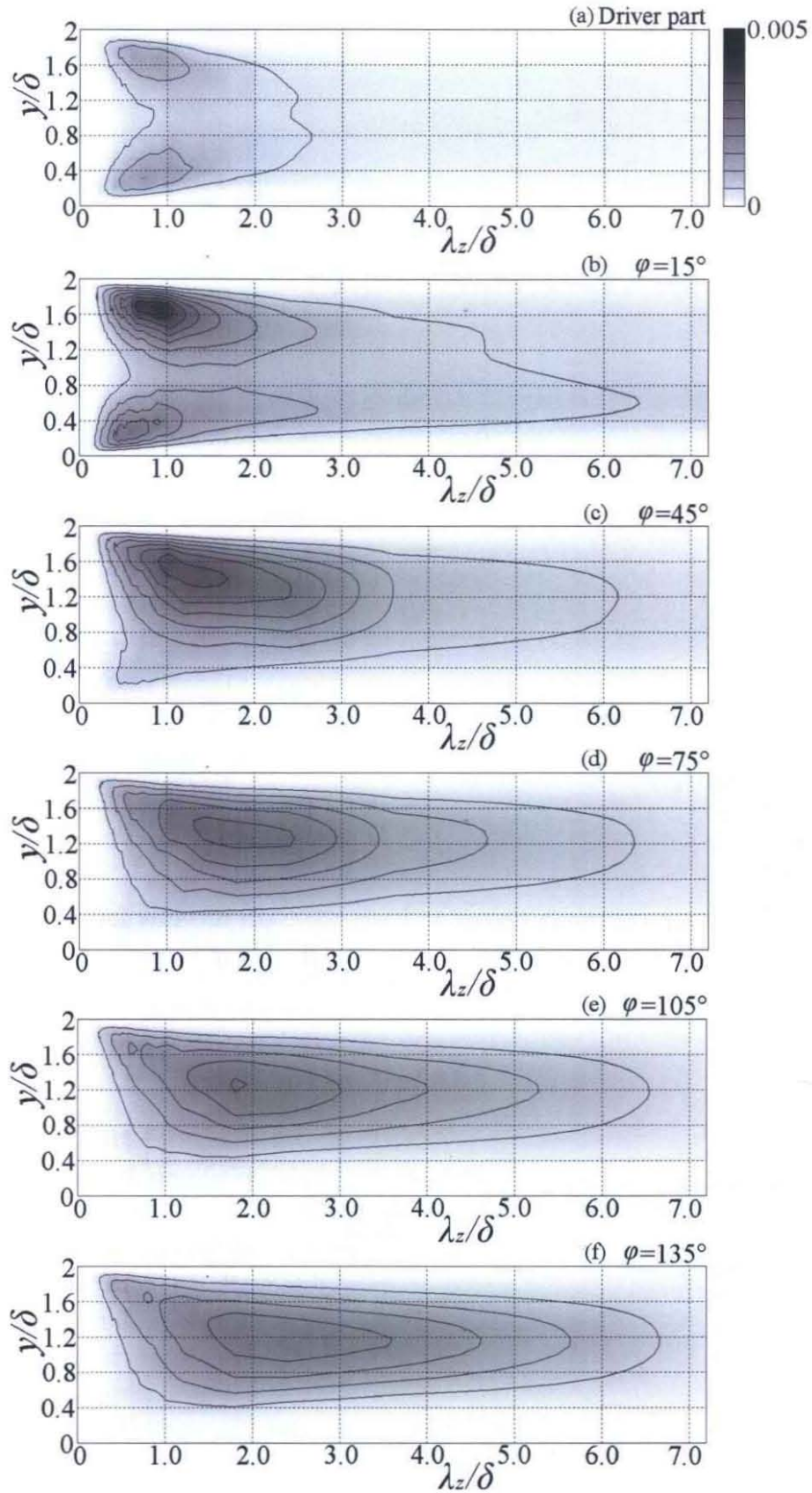


Fig. 5.7 Contours for spanwise pre-multiplied power spectra of wall-normal velocity, $k_z E_{vvz} / U_m^2$, in curved channel with inner rib.

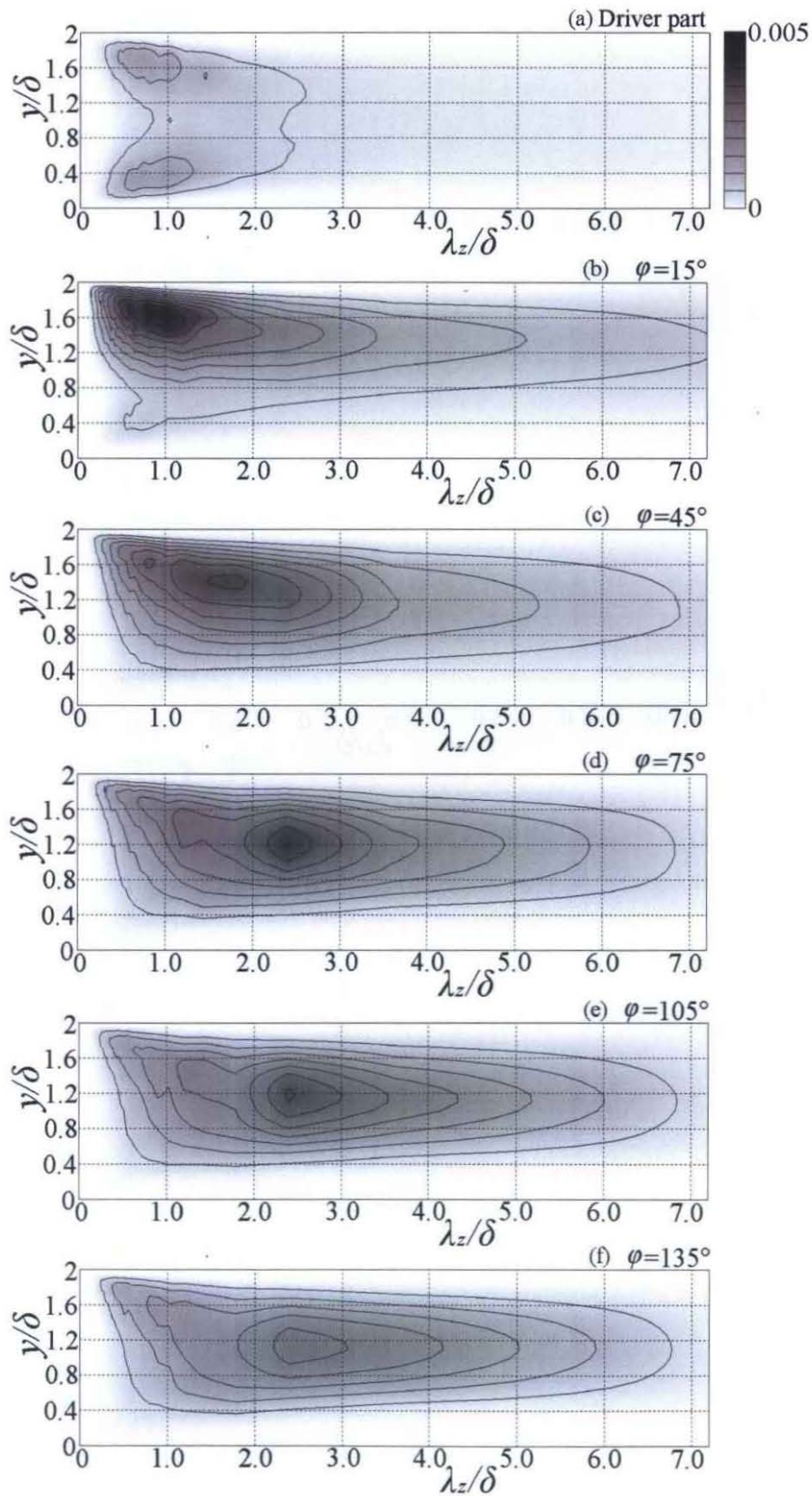
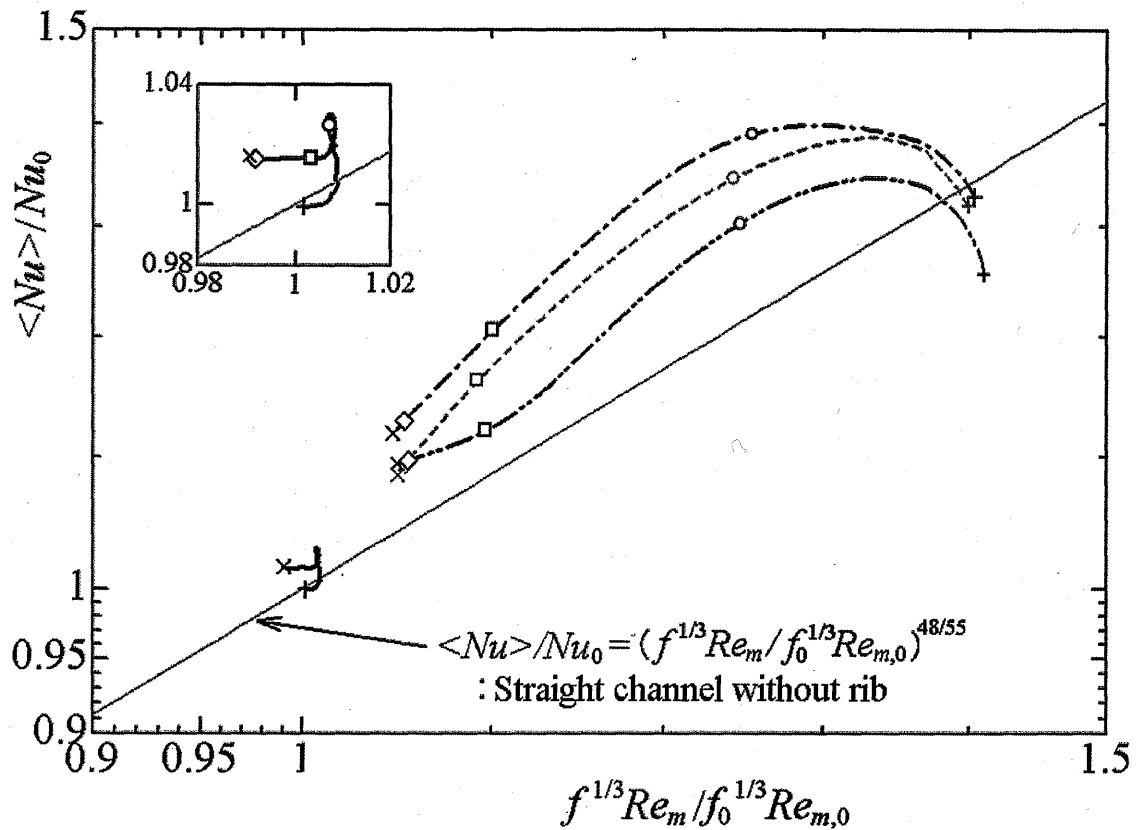


Fig. 5.8 Contours for spanwise pre-multiplied power spectra of wall-normal velocity, $k_z E_{vvz} / U_m^2$, in curved channel with outer rib.



Straight channel with rib

$x/\delta = 62.6 \quad 56.5 \quad 31.4 \quad 6.3 \quad 0$
 $\times \text{---} \diamond \text{---} \square \text{---} \circ \text{---} +$

Curved channel with inner rib

$x/\delta = 62.6 \quad 56.5 \quad 31.4 \quad 6.3 \quad 0$
 $\varphi = 150^\circ \quad 135^\circ \quad 75^\circ \quad 15^\circ \quad 0^\circ$
 $\times \text{---} \diamond \text{---} \square \text{---} \circ \text{---} +$

Curved channel without rib

$x/\delta = 62.6 \quad 56.5 \quad 31.4 \quad 6.3 \quad 0$
 $\varphi = 150^\circ \quad 135^\circ \quad 75^\circ \quad 15^\circ \quad 0^\circ$
 $\times \text{---} \diamond \text{---} \square \text{---} \circ \text{---} +$

Curved channel with outer rib

$x/\delta = 62.6 \quad 56.5 \quad 31.4 \quad 6.3 \quad 0$
 $\varphi = 150^\circ \quad 135^\circ \quad 75^\circ \quad 15^\circ \quad 0^\circ$
 $\times \text{---} \diamond \text{---} \square \text{---} \circ \text{---} +$

Fig. 5.9 Mean Nusselt number versus pumping power.

5.7. Conclusions

Direct numerical simulation was performed for flow and heat transfer in a curved channel with a single rib. The rib was mounted on either the inner or outer wall in front of the curve. The radius ratio was 0.92, and the outlet of the curved channel was at 150° . The frictional Reynolds number was assigned at 150, and the Prandtl number was given 0.71. Conclusions thus extracted are as follows.

- Heat transfer in the channel was enhanced by the rib effects. Compared to the straight channel with the rib, heat transfer was enhanced notably in the first half of the inner-rib case and in the second half of the outer-rib case.
- The heat transfer enhancement behind the inner rib was generated by the turbulence of the rib. The enhancement in the outer-rib case resulted from the growth of the large-scale vortices. These were suggested by time-mean velocity vectors and spectral analysis.

- The inner-rib case had better thermo-hydraulic performance than the outer-rib case until the outlet of the curved channel. However, the latter case narrowed the gap in the second half of the channel.

5.8. References

- (1) Ligrani, P. M. and Niver, R. D., Flow visualization of Dean vortices in a curved channel with 40 to 1 aspect ratio, *Physics of Fluids*, Vol. 31 (1988), pp.3605-3617.
- (2) Bland, S. B. and Finlay, W. H., Transitions toward turbulence in a curved channel, *Physics of Fluids A*, Vol. 3, No. 1 (1991), pp.106-114.
- (3) Ligrani, P. M., Finlay, W. H., Fields, W. A., Fuqua, S. J. and Subramanian, C. S., Features of wavy vortices in a curved channel from experimental and numerical studies, *Physics of Fluids A*, Vol. 4, No. 4 (1992), pp.695-709.
- (4) Guo, Y. and Finlay, W. H., Splitting, merging and wavelength selection of vortices in curved and/or rotating channel flow due to Eckhaus instability, *Journal of Fluid Mechanics*, Vol. 228 (1991), pp.661-691.
- (5) Ligrani, P. M., Skogerboe, P., Schallert, A. R. and Skogerboe, P., Effects of Dean vortex pairs on surface heat transfer in curved channel flow, *International Journal of Heat and Mass Transfer*, Vol. 39, No. 1 (1996), pp.27-37.
- (6) Kobayashi, M., Maekawa, H., Takano, T. and Hayakawa, S., An experimental study on a turbulent flow in a two-dimensional curved channel (time-mean velocity and multiple velocity correlations in the entrance section), *Transactions of the JSME Series B*, Vol. 57 (1991), pp.4064-4071.
- (7) Kobayashi, M., Maekawa, H., Shimizu, Y. and Uchiyama, K., An experimental study on a turbulent flow in a two-dimensional curved channel (space-time correlation and spectra of velocity fluctuations), *Transactions of the JSME Series B*, Vol. 58 (1992), pp.119-126.
- (8) Moser, R. D. and Moin, P., The effects of curvature in wall-bounded turbulent flows, *Journal of Fluid Mechanics*, Vol. 175 (1987), pp.479-510.
- (9) Matsubara, K., Matsui, A., Miura, T., Kawai, K., Kobayashi, M. and Suto, H., Multi-scale coherent structures of spatially advancing turbulent flows in curved channel, *Proceedings of 6th International Symposium on Turbulence and Shear Flow Phenomena*, (2009), pp.29-34.
- (10) Matsubara, K., Matsui, A., Miura, T., Sakurai, A., Suto, H. and Kawai, K., A spatially advancing turbulent flow and heat transfer in a curved channel, *Heat Transfer—Asian Research*, Vol. 39, No. 1 (2010), pp.14-26.

Chapter 6 Conclusions

In this thesis, direct numerical simulation was performed for air flows and related heat transfer in a channel with a single rib or several ribs. A curved channel with a single rib was also treated. The transverse rectangular ribs were mounted on one wall. The inflow was a fully developed turbulent plane-channel flow at the frictional Reynolds number of mainly 150. The major conclusions are as follows.

- The computational results agreed well with the following experimental data: a mean pressure distribution on the wall with a single rib, logarithmic velocity profiles in rough-wall boundary layers, and relative heat transfer coefficient distributions on rough-wall.
- Several kinds of computation were made with changing computational domain and grid arrangement. The minimum grid points were about 2.4×10^6 , and the maximum were about 9.7×10^7 . Computational results from these simulations showed almost no difference. Therefore, these simulations had enough domain and resolutions.
- In single rib cases, the rib height was changed at $H/\delta = 0.05, 0.10, 0.20, 0.40$. $H/\delta = 0.20$ and 0.40 were almost the same efficiency and had the highest thermo-hydraulic performance. There was little difference in the performance between $H/\delta = 0.05$ and the smooth channel.
- In the single rib at $H/\delta = 0.20$, turbulence statistics and Reynolds stress budgets were presented. These data would be useful for testing and developing turbulence models. In addition, mechanisms of heat transfer enhancement were examined through discussion of these data.
- Behind the single rib, the dissimilarity between momentum and heat transfer was generated. I revealed that large spanwise vortices shed from the rib both acted to decrease the wall friction and to increase the heat transfer.
- In repeated-rib cases, the wide rib-pitch ($Pi/H \approx 9$) showed the best thermo-hydraulic performance for the fully developed region, but the narrower rib-pitch ($Pi/H = 2$ or 4) was better than the wide pitch in the developing region.
- A thin thermal layer came to the initial region of the ribbed channels, and the rough surfaces were exposed to high temperature. Therefore, $Pi/H = 2$ and 4 had high heat transfer in spite of low pumping loss.
- In a curved channel with a single rib, the curved channel with the inner rib had better thermo-hydraulic performance than that with the outer rib because the inner rib enhanced declining heat transfer on the inner wall. However, the outer-rib case narrowed the gap by large-scale vortices in the second half of the curved channel.

The knowledge which would contribute to the improvement in the thermo-hydraulic performance on roughness was presented. I will be glad if the knowledge is utilized for an actual product, for validating a computation, and for future research.

Appendix: Parallel Computation

Parallel computation was applied to the simulations, because the present study had huge computational load: Open Multi-Processing (OpenMP) and Message Passing Interface (MPI) were used for Case 3 of Chapter 3, and only OpenMP was applied for the other simulations.

The computational domains were divided in the streamwise direction for MPI (Fig. A1), except in the solution of the Poisson's equation. The computational domains were decomposed in the spanwise direction during the FFT and inverse FFT for the streamwise direction, the TDMA and the SOR method with the recomposition of the sub-domains. In addition, Open MP was used for further parallelization within each sub-domain.

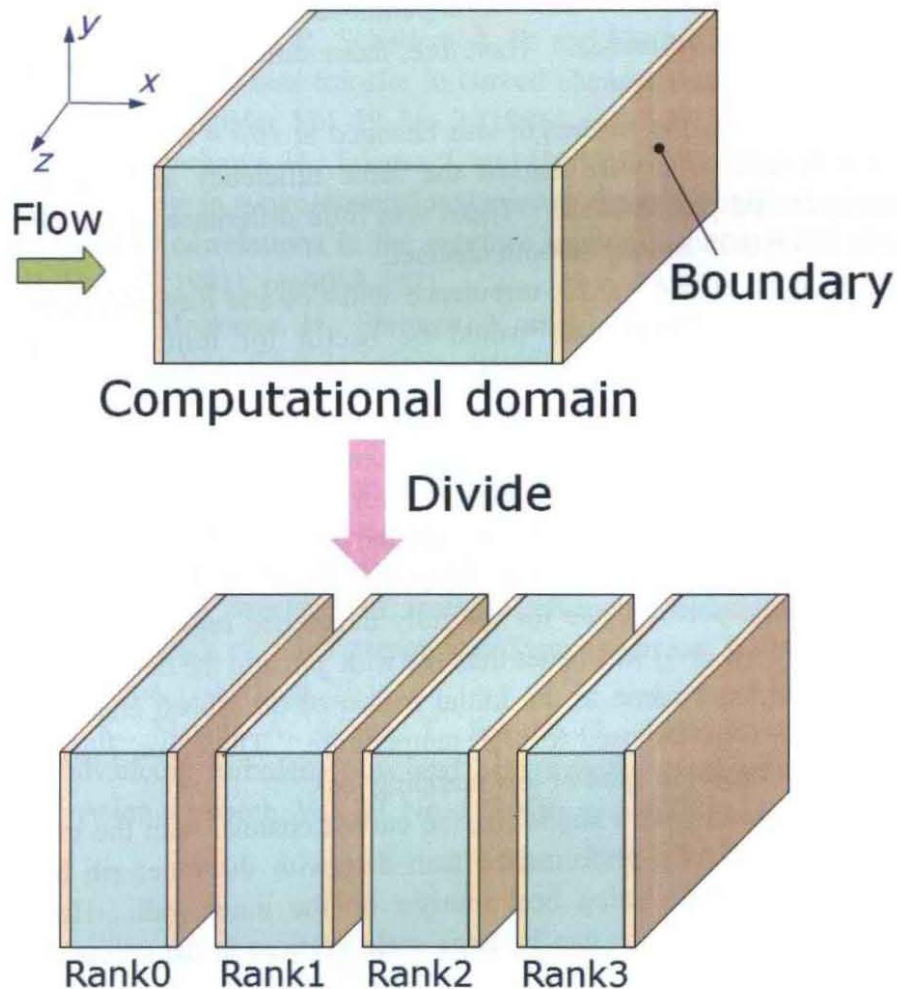


Fig. A.1 Divided computational domain for MPI into four.

Acknowledgements

First of all, I would like to thank Dr. Koji Matsubara, who is my supervisor since my bachelor thesis; for his elaborated guidance, invaluable discussion, broad support and considerable encouragement. I have been fortunate to have such a great supervisor.

I would like to express my sincere gratitude to Prof. Takatsune Narumi, who is this thesis supervisor. He has encouraged and advised me many times. I would also like to thank the other member of my thesis committee: Prof. Nobuyuki Fujisawa, whose helpful suggestions improved this thesis.

I also thank Dr. Atsushi Sakurai. He always commented on my presentation in laboratory seminars. He also improved my papers.

I want to express my gratitude to all members of the laboratories: Thermal Engineering Lab and Radiative Transfer Lab in Niigata University. Mr. Akihiko Matsui, Mr. Koji Kawai, Mr. Kenya Yamazaki, and Mr. Makoto Takeda investigated curved channel flows. Mr. Takashi Uchida and Mr. Suguru Tachikawa computed the curved channel flow with a single rib. Mr. Yoshiyuki Nagai supported the study of channel flow with ribs. Mr. Yuta Kobayashi has been co-researcher on the channel flow with a single rib. Mr. Shunsuke Kazama has studied the numerical method of constant temperature walls with me. Mr. Satoshi Ohta has supported setup of computers. They contributed obviously to this thesis; however, other members also supported me.

I would like to express my thanks for the financial supports: Japan Student Services Organization Scholarship in the first and second years, Japan Society for the Promotion of Science Research Fellowship for Young Scientists in the third year. I would also like to thank the Supercomputing Division, Information Technology Center, at the University of Tokyo. A part of the present computations was performed by their parallel computer.

Finally, I thank my family. They supported me from childhood to now.